UNIVERSITY OF MODENA AND REGGIO EMILIA

PH.D. DISSERTATION

Soft-Switching DC-DC Power Converters and Electric Drives for Green Transportation

Author:
Raffaele FORNARI

Supervisor:
Prof. Emilio LORENZANI

School Dean:
Prof. Franco ZAMBONELLI

A thesis submitted for the degree of Doctor of Philosophy in

Industrial Innovation Engineering

XXXII cycle

Department of Sciences and Methods for Engineering

5 March 2020

UNIVERSITÀ DEGLI STUDI DI MODENA E REGGIO EMILIA

TESI DI DOTTORATO

Convertitori DC-DC Soft-Switching e Azionamenti Elettrici per l'Elettrificazione dei Trasporti

Candidato:
Raffaele FORNARI

Relatore:
Prof. Emilio LORENZANI

Coordinatore del Corso di Dottorato:
Prof. Franco ZAMBONELLI

Dottorato di Ricerca in

Ingegneria dell'Innovazione Industriale

Ciclo *XXXII*

Dipartimento di Scienze e Metodi dell'Ingegneria

5 Marzo 2020

Acknowledgements

This thesis work completes my Ph.D. work and I would like to express gratitude to Prof. Emilio Lorenzani. He was my Bachelor's degree, Master's degree and, finally, Ph.D. supervisor and thanks to his guidance I gained professional and engineering skills.

I want also to thank for this work Prof. Fabio Immovilli, Claudio Bianchini, Andrea Stefano Crinto ("The Boss"), all other colleagues, my Ph.D. student colleagues Giovanni Migliazza and Ambra Torreggiani and who helped and cooperated with me. I say thank because it has been a pleasure working with them.

I would like to recognize the invaluable assistance provided during my studies by my parents, my brothers, my sister, my friends and my fiancée Lucy, who have shared the joys and challenges of this period and have supported me.

Contents

Introduction

Energy efficiency and emissions reduction were better attended to due to climate changes and global warming. Greater interest has been generated towards research pertaining to renewable energy sources. Nowadays, transportation is one of the biggest contributors to air pollution and to the widespread fossil fuel usage. In the past few years, the industry and academic research have attempted to develop electric vehicles. Power electronics plays a crucial role in this field that is continuously growing up. Thermal modelling and efficiency maximization of switching converters, magnetics design, Electro Magnetic Compatibility (EMC), system reliability and cost reduction are certain aspects demanded by the transport electrification process. The battery pack supplies energy to the electric motor used for the vehicle propulsion, and to the systems related to vehicle safety or to the driver's comfort, such as lighting, air conditioning and infotainment. These loads may require a wide range of input-output voltages and for this reason, is necessary the adoption of converters specifically designed to fulfil these requirements. A battery charger is an example of such converters. It can be placed on-board or outside of the vehicle, and its typology is either monodirectional or bidirectional. Bidirectionality is mandatory when the converter must manage both phases of propulsion and regeneration to recover energy. Accordingly, the battery charger can be integrated into a single-stage solution able to manage the charge of the battery pack and to supply the on-board loads. In this context, motor control is another area of interest wherein researchers are investigating new algorithms to improve and optimize electric machine performances during vehicle propulsion.

This thesis deals with all these prospects by proposing solutions corroborated by simulation models and experimental validations. The aim is to show the design of power converters functional to electric powertrain and to describe control algorithms able to optimise the performance of the electric motor intended for vehicle propulsion. In addition, are described the function modes adopted to satisfy high efficiency requirements and to optimize the performance, and are assessed the results obtained from experimental validations.

This thesis details two DC-DC power converters: an LLC architecture proposed as power stage of a unidirectional battery charger and a Dual Active Bridge (DAB) proposed either as a battery charger suitable for *Vehicle-to-Grid* (V2G) capability or as bidirectional converter part of a *Smart Home*. The design of the resonant tank of the former typology has been carried out in order to satisfy the constraints on the wide output voltage regulation range. For this purpose, the hard-switching commutations have been analysed when the PWM modulation is adopted at light load and an alternative approach has been proposed to mitigate the effects. In the following, has been performed the design of a DAB with a wide input-output voltage range. The results have been shown for advanced modulation techniques implemented for the maximization of the conversion's efficiency on the whole operating range. The motor control theory has been analysed in the last chapter of the thesis and has been

presented an enhanced flux-weakening algorithm developed for a powertrain application. The fast transitions from propulsion to regeneration (and vice versa) of the electric machine in flux-weakening operations are properly managed using this control strategy. During these phases, the saturation and windup of the control loop regulators may happen and the torque and power delivered by the motor have been improved through a strategy enhanced with a feed forward contribution.

In summary, the content of the chapters being part of this thesis work:

Chapter 1 This chapter deals with a brief introduction to green transportation. The architectures of Hybrid Electric Vehicle and Full Electric Vehicle are presented, relating to that the advantages and issues. The role of the power electronics is introduced as the requirements assessed for a DC-DC power converter, in terms of power density and wide input/output voltage capability. The intended use of the power converter is described for each architecture. It can be installed on the vehicle taking part in the propulsion or can be used as an off-board battery charger.

Chapter 2 In this chapter the design of a 2kW LLC converter is presented. The resonant tank parameters are chosen to match with wide voltage/power range capability and the benefits are presented introducing PWM modulation at light load condition. The asymmetric effects resulting from the enhanced PWM modulation on the current and voltage waveforms are analysed as well. An innovative *Adaptive PWM* control technique is proposed for minimization of the losses due to the hard-switching events on the first commutation. The PWM signals state is used by the Peak Detector Circuit to identify the free oscillation of the midpoint voltage. The gate signals are masked until the *soft-switching* condition for the high side MOSFET is identified and then the modulation is re-enabled. A Duty Cycle Corrector compensates the duty cycle of the low side device to avoid the transformer saturation. The constructed prototype is proposed as a power conversion stage of a unidirectional battery charger and the experimental results are carried out. The efficiencies are obtained and compared in PFM and PWM operations.

Chapter 3 The Dual Active Bridge typology is suitable for DC-DC power converters requiring bidirectionality and galvanic isolation. These characteristics are mandatory to transfer the energy from the battery to the load when the converter installed on the vehicle has to manage the regenerative braking phase. The *wide-voltage* operating range comes from the need to interface the high voltage DC-links with the battery, typically of low voltage rate. The V2G capability is another case where the bidirectionality is indented for the battery charger. Further, the galvanic isolation and wide-voltage capability are wanted when the battery of the vehicle is used as storage mean of a renewable energy plant. This chapter deals with the design of a $3,2$kW Dual Active Bridge converter, indented as a bidirectional *single-stage* wide voltage/power range converter. The traditional Phase-Shift modulation allows the *soft-switching* operations in the working range limited to the nominal design conditions. The Trapezoidal and Triangular modulation techniques are implemented to extend the *soft-switching*, maximizing the efficiency over the whole wide-voltage operating range. The presented implementation provides that the dwell times are computed in *feed forward* and an additional block is inserted to compensate the inaccurate knowledge of all DAB parameters. An analysis of the switching and

conduction losses is carried out for the two advanced modulations, disclosing that different criteria can be adopted to choose the devices according to the predominant modulation sequence. The experimental validation is presented at the end of the chapter.

Chapter 4 The Interior Permanent Magnet Synchronous Motor control is the topic of this chapter. Different control strategies are presented to address the critical issue of fast torque transition, presenting *enhanced flux-weakening* strategies based on outer voltage loop or i_d current error. During the fast transition of torque set point, the current angle error due to iron losses changes its sign, the saturation and windup of the control loop regulators may happen. These phenomenons make difficult during the regenerative braking phase to manage the energy-flow transition from the motor to the battery to avoid battery unsafe operation or overcharge. Moreover, the vehicle behaviour could be heavily affected by the braking torque generated by the motor, especially for motorcycles also a short time braking torque could cause driver injuries. These main critical issues of common flux-weakening strategies are investigated through experimental tests. The results of new and improved control methods, based on a *feed forward* contribution, are shown comparing the operating region profiles of the improved methods obtained by test bench experimental.

The author of this thesis work had been enrolled from November 2016 to November 2019 in XXXII doctoral program in Mechatronics and Energy curricula of the Industrial Innovation Engineering Doctorate School. The period of the course was spent at the Department of Science and Methods of Engineering of the University of Modena and Reggio Emilia. He has cooperated with Power Electronics and Electric Drives research group with the guidance of Prof. Emilio Lorenzani. The full list of publications produced by the author during the Ph.D. period is reported at the page 8. The author recommends inspecting the publications' list to deepen the topics on high efficient soft-switching converters and electric machines drives. The abroad experience the author had in July-August 2019 at the PEMC laboratory of the University of Nottingham UK, has allowed sharing with other researchers the skills acquired and the research activities carried out during the Ph.D. course.

Introduzione

I cambiamenti climatici e la ricerca di fonti rinnovabili come sorgente d'energia hanno suscitato una sensibilità sempre maggiore per ciò che riguarda l'efficienza energetica e la riduzione delle emissioni. I mezzi di trasporto, ad oggi, sono tra le principali cause d'inquinamento dell'aria e rappresentano uno dei motivi di maggior sfruttamento dei combustibili fossili. Infatti negli ultimi anni, grande è stato l'interesse nel settore industriale e nel mondo della ricerca per lo sviluppo di veicoli elettrici. Un campo questo, in crescente espansione anche grazie allo sviluppo dell'elettronica di potenza, chiamata in causa per ciò che riguarda: la modellazione termica e la massimizzazione dell'efficienza dei convertitori switching, il dimensionamento dei magnetici, la compatibilità elettromagnetica (EMC), l'incremento dell'affidabilità dei sistemi e la riduzione dei costi. Dal pacco batterie del veicolo vengono alimentati il motore elettrico utilizzato per la trazione e i sistemi legati alla sicurezza o al comfort di guida, come i dispositivi di illuminazione, la climatizzazione e l'infotainment. Inoltre, queste tipologie di utenze possono richiedere un regime operativo ad ampio range di funzionamento delle tensioni di ingresso-uscita. Per questo motivo si rende necessaria l'adozione di convertitori utili all'alimentazione di tali utenze, specificatamente progettati per adempiere a tali requisiti operativi. Il caricabatterie ne è un esempio, esso può essere di tipologia monodirezionale o bidirezionale e trovarsi a bordo del mezzo o all'esterno. La bidirezionalità del suo stadio di conversione è richiesta per gestire sia la fase di propulsione che quella di recupero dell'energia in fase rigenerativa. In questo modo il caricabatterie può essere integrato in un'unica soluzione in grado sia di caricare le batterie, sia di alimentare le altre utenze a bordo del veicolo. Il controllo motore rappresenta un altro ambito ancora che afferisce all'elettrificazione dei trasporti. Lo sviluppo di algoritmi che massimizzino le performance del motore elettrico e, più genericamente della trazione elettrica, sono di particolare interesse per lo sviluppo di un veicolo elettrico.

Tutti questi aspetti sono oggetto del lavoro di tesi che viene esposto, nella cui trattazione vengono proposte soluzioni da considerarsi sempre avvalorate e sostenute da simulazioni e prove sperimentali. Si intende illustrare la progettazione di convertitori funzionali alla trazione elettrica e descrivere algoritmi per il controllo motore in grado di ottimizzare le prestazioni del motore elettrico destinato alla trazione del veicolo. Inoltre, vengono descritte le modalità di funzionamento adottate per soddisfare requisiti di alta efficienza e ottimizzazione delle prestazioni, e vengono valutati i risultati ottenuti dalle prove sperimentali.

Nello specifico di questo lavoro di ricerca si presentano due convertitori DC-DC: un'architettura LLC proposta come stadio di potenza di un caricabatterie monodirezionale, e un Dual Active Bridge (DAB) proposto come caricabatterie compatibile con il sistema *Vehicle-to-grid* (V2G) o come convertitore bidirezionale di una *Smart Home*. Riguardo la prima tipologia viene illustrato il dimensionamento del resonant tank per soddisfare specifiche di funzionamento ad ampio range di regolazione della tensione di uscita. A tale scopo sono state analizzate le commutazioni hard-switching che si verificano durante la modulazione PWM, adottata a carico leggero,

e una tipologia di controllo che ne mitighi gli effetti. Il convertitore DAB che viene presentato nel proseguo della trattazione, è stato dimensionato per un ampio range di tensioni di ingresso-uscita. I risultati che si trovano illustrati sono stati ottenuti con l'implementazione di strategie avanzate di modulazione, finalizzate a massimizzare il rendimento dello stadio di conversione rispetto a tutto il range operativo di funzionamento. Infine, nell'ultimo capitolo di questa tesi, analizzando la teoria del controllo motore si presenta un algoritmo avanzato di flux-weakening sviluppato per un'applicazione per trazione. Esso è in grado di mitigare le problematiche relative alle fasi di transizione rapida dagli stati di funzionamento da motore e da generatore della macchina elettrica. In tali transitori si verificano fenomeni di saturazione e windup degli anelli di regolazione. Grazie a una strategia di deflussaggio basata su un contributo feed forward sono stati ottenuti benefici sulla coppia motrice e la potenza erogata dal motore.

Di seguito, in sintesi, viene riportato il contenuto dei capitoli del lavoro di tesi:

Capitolo 1 Il primo capitolo tratta una breve introduzione sull'elettrificazione dei trasporti. Vengono portati in evidenza i vantaggi e le criticità legate alle architetture dei veicoli ibridi o totalmente elettrici. Viene investigato il ruolo svolto dall'elettronica di potenza, denotando le caratteristiche richieste. Fra queste sono di particolare rilievo la densità di potenza e la compatibilità di utilizzo per un ampio range di tensioni di ingresso/uscita. Per ogni architettura viene indicata la destinazione d'uso del convertitore DC-DC, che può essere installato a bordo del veicolo o essere utilizzato come caricabatterie.

Capitolo 2 In questo capitolo viene dimensionato un convertitore LLC da 2kW. I valori del resonant tank vengono scelti per l'adattabilità a un funzionamento ad ampio range di tensioni di ingresso/uscita e vengono descritti i benefici ottenuti dalla modulazione PWM, adottata in condizioni di carico leggero. Vengono anche analizzate le problematiche dovute alle asimmetrie introdotte dalla modulazione PWM avanzata. Si propone un controllo PWM di tipo *adattivo* per la minimizzazione delle perdite dovute alle commutazioni hard-switching sulla prima commutazione. Lo stato dei segnali PWM è utilizzato dal Peak Detector Circuit per identificare l'oscillazione libera della tensione di midpoint. I segnali di gate sono mascherati fino a quando non viene identificata la condizione di soft-switching per il MOSFET di high side, in corrispondenza della quale viene riabilitata la modulazione. Il duty cycle del dispositivo di low side viene compensato dal Duty Cycle Corrector per prevenire la saturazione del trasformatore. Sono riportati i risultati sperimentali ottenuti con il prototipo realizzato, destinato come stadio di conversione di un caricabatterie unidirezionale. Vengono analizzati e messi a confronto i dati di efficienza ottenuti in funzionamento PFM e PWM.

Capitolo 3 L'architettura Dual Active Bridge è una tipologia di convertitore DC-DC destinata ad applicazioni che richiedono bidirezionalità e isolamento galvanico. Queste caratteristiche sono mandatorie quando il convertitore deve riversare energia verso le batterie in fase di frenata rigenerativa del veicolo. Il funzionamento ad *ampio range di tensioni* è necessario per interfacciare il DC-link ad alta tensione con la batteria, tipicamente a bassa tensione. La compatibilità per il V2G è un differente caso dove è richiesto il funzionamento bidirezionale del caricabatterie. L'utilizzo della batteria del veicolo come strumento di accumulo di un impianto di energia rinnovabile è un'ulteriore

applicazione che richiede l'isolamento galvanico e l'ampio range di tensioni di ingresso/uscita. In questo capitolo viene sviluppato un convertitore Dual Active Bridge da $3,2$kW, destinato ad applicazioni a *singolo stadio* di conversione per un funzionamento ad ampio range della potenza e delle tensioni di ingresso/uscita. Il tradizionale schema di modulazione Phase-Shift permette di ottenere un regime di funzionamento soft-switching limitato alle condizioni nominali di funzionamento. Sono state implementate le modulazioni Trapezoidale e Triangolare per estendere il funzionamento *soft-switching* e ottenere la massimizzazione dell'efficienza sull'intero range operativo ad ampia variazione delle tensioni/potenza di ingresso/uscita. L'implementazione che viene presentata prevede che il calcolo dei dwell times sia ottenuto in *feed forward* e la inaccurata conoscenza dei parametri del DAB sia compensata da un blocco addizionale. Viene svolta un'analisi delle perdite di switching e di conduzione per i due schemi di modulazione avanzata e viene fornito un criterio per la scelta dei dispositivi in base allo schema di modulazione principalmente adottato. In conclusione al capitolo sono riportati i risultati della validazione sperimentale.

Capitolo 4 La trattazione di questo capitolo riguarda il controllo del Motore Sincrono a Magneti Permanenti Interni. Vengono riportate differenti strategie di controllo per risolvere le criticità risultanti dai transitori rapidi di coppia, mediante strategie di *deflussaggio avanzato* e basate sull'anello di outer voltage o sull'errore di corrente i_d. Durante un transitorio rapido del set point di coppia, l'errore dell'angolo di corrente cambia segno a causa delle perdite nel ferro e possono avere luogo la saturazione e il windup degli anelli di regolazione. Questi fenomeni rendono difficoltoso il riversamento di energia dal motore alla batteria durante la fase di frenata rigenerativa, diventando causa di danneggiamento o sovraccarica della batteria. Inoltre, il comportamento del veicolo può essere inficiato dalla coppia frenante risultante ponendo il guidatore in condizione di pericolo. Questi aspetti critici per le comuni strategie di deflussaggio sono stati investigati attraverso prove sperimentali. Tramite il confronto dei profili e delle curve di lavoro ottenute a banco prova, sono mostrati i risultati derivanti da una metodologia di controllo avanzata basata su un contributo *feed forward*.

L'autore di questo lavoro di tesi è stato iscritto dal novembre 2016 al novembre 2019 al XXXII ciclo della Scuola di Dottorato in Ingegneria dell'Innovazione Industriale presso il Dipartimento di Scienze e Metodi dell'Ingegneria dell'Università di Modena e Reggio Emilia. Ha collaborato con il gruppo di ricerca in Macchine Convertitori e Azionamenti Elettrici sotto la guida del Prof. Emilio Lorenzani. La lista completa delle pubblicazioni conseguite durante il periodo di dottorato è riportata a pagina 8. L'autore consiglia di prenderne visione per meglio approfondire le tematiche riguardanti i convertitori DC-DC soft-switching e il controllo delle macchine elettriche. L'esperienza all'estero avuta dall'autore nel luglio-agosto 2019 presso il laboratorio PEMC dell'università di Nottingham UK, ha permesso di condividere con altri ricercatori l'esperienza acquisita e i risultati conseguiti dalle attività di ricerca svolte durante il periodo di dottorato.

Author's publications

[1] Cristiano Maria Verrelli, Emilio Lorenzani, Raffaele Fornari, Michele Mengoni, and Luca Zarri. "Steady-state speed sensor fault detection in induction motors with uncertain parameters: A matter of algebraic equations". In: *Control Engineering Practice* 80 (2018), pp. 125–137. ISSN: 0967-0661. DOI: `https://doi.org/10.1016/j.conengprac.2018.08.016`. URL: `http://www.sciencedirect.com/science/article/pii/S0967066118304593`.

[2] C.M. Verrelli, P. Tomei, E. Lorenzani, R. Fornari, and F. Immovilli. "Further results on nonlinear tracking control and parameter estimation for induction motors". In: *Control Engineering Practice* 66 (2017), pp. 116–125. ISSN: 0967-0661. DOI: `https://doi.org/10.1016/j.conengprac.2017.05.008`. URL: `http://www.sciencedirect.com/science/article/pii/S0967066117301247`.

[3] D. Benatti, G. Migliazza, R. Fornari, E. Lorenzani, and G. Buticchi. "Analytical Equivalent Circuit Model for Series-Compensated Wireless Power Transfer Systems". In: *IECON 2019 - 45th Annual Conference of the IEEE Industrial Electronics Society*. Vol. 1. Oct. 2019, pp. 4177–4182. DOI: `10.1109/IECON.2019.8926902`.

[4] R. Fornari, G. Migliazza, E. Lorenzani, and F. Immovilli. "Critical Aspects of Hybrid PFM-PWM Operation in LLC Converters For Electric Vehicles". In: *2018 IEEE International Conference on Electrical Systems for Aircraft, Railway, Ship Propulsion and Road Vehicles International Transportation Electrification Conference (ESARS-ITEC)*. Nov. 2018, pp. 1–6. DOI: `10.1109/ESARS-ITEC.2018.8607763`.

[5] R. Fornari, F. Immovilli, and E. Lorenzani. "Wide Voltage Range Dual Active Bridge PV Retrofit Storage System". In: *IECON 2019 - 45th Annual Conference of the IEEE Industrial Electronics Society*. Vol. 1. Oct. 2019, pp. 2524–2531. DOI: `10.1109/IECON.2019.8926933`.

[6] R. Fornari, G. Franceschini, D. David, A. Torreggiani, C. Bianchini, and M. Frigieri. "Enhanced Internal Permanent-Magnet Machines Flux Weakening Control Strategies for Traction Applications". In: *IECON 2019 - 45th Annual Conference of the IEEE Industrial Electronics Society*. Vol. 1. Oct. 2019, pp. 2682–2687. DOI: `10.1109/IECON.2019.8926936`.

Chapter 1

Green transportation and electric vehicles

1.1 Transport electrification

In the last years, the research's activities have investigated a lot on environmental care, pollutions problems and global warming. The climate changes are the most important motivation for energy efficiency and emission reduction. Transportation is one of the most causes of air quality deterioration. Over the past decade, the prices of fossil fuels have increased as the worries about their availability in the next years. As a consequence, many car builders are introducing electric and hybrid vehicles in the market. A vehicle equipped with an Internal Combustion Engine (ICE) relies on the combustion of hydrocarbon fuels as source of energy. Heat and combustion gases are produced by the combustion, which is a reaction between the fuel and the air. Ideally, the combustion would yield only carbon dioxide and water. In practical the combustion is never ideal and besides these products produces nitrogen oxides (NO_x), carbon monoxide (CO), sulfur oxides (SO_x) and unburned residuals of fuel. Moreover, the petroleum companies add chemical compounds to the fuels to improve the performance of the engines. Modern ICE vehicles are reliable, comfortable, have excellent performance and are used for all kinds of applications: from personal car to heavy load caterpillar. Despite one century of activity research and development of this technology, only 30% of the amount of energy produced is converted for the motion of the vehicle. Approximately 70% of the energy is wasted as heat. As shown in Fig. 1.1 in terms of efficiency the electric motors (EMs) are far superior, with a value of around 85%.
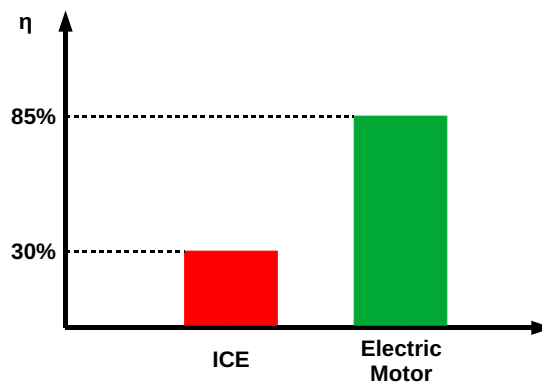

FIGURE 1.1: Efficiency of an ICE and of an EM.

Further, they have not gas emissions, are noise-free and the efficiency can be optimized by means of advanced control strategy of the electric drive, such as regenerative braking or optimization of power electronics driver topologies. These aspects have put the attention of the industry and academia on the transport electrification. Anyway, a critical aspect concerns the impact of massive use of electric vehicles on the grid. The electric grid capacity must be able to sustain a big number of new consumers and the carbon dioxide production can be effectively reduced if the energy production is made by carbon-free resources (solar, wind, hydro, nuclear).

Differentiating the vehicle by the energy source, they can be classified as shown in Fig. 1.2. Three typology of vehicles are listed [1], [2], [3], [4]:

- Internal Combustion Engine Vehicle

- Hybrid Electric Vehicle

- Electric Vehicle

The hybrid represents a midway solution between the ICE vehicles and electric vehicles. The automotive companies look for an intermediate transition from the old technology to the new one, of course. The hybrid solution looks like as "short term" solution while the autonomy and infrastructure problems related to the "pure" electric vehicles are still not solved.
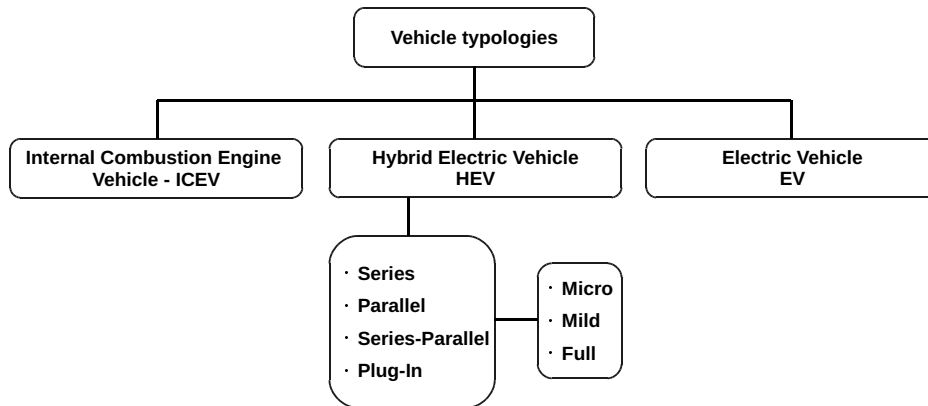

FIGURE 1.2: Typologies of vehicles.

1.2   Hybrid Electric Vehicles - HEVs

A vehicle having more than one energy source is classified as "hybrid". The propulsion energy sources are available at the same time during the driving and can be selected upon the driving or terrain conditions. As stated in the introduction of this chapter, at this time a hybrid vehicle represents a compromise for environmental care and the limits affecting pure electric vehicle. Besides the ICE, the vehicle is equipped with an EM and other power electronics related to the drive. The benefits of the internal combustion engine are merged with ones of the EM. The EM can supply the traction in order to partially or completely sustains it and allowing the ICE to work at the maximum point of efficiency. The critical issues of a pure electric vehicle (such as a limited operating range and charging point availability) are solved, but the design complexity of the vehicle is greater.

Different layout platforms and configurations can be adopted for a HEV. Figure 1.3 shows the power flow from the energy sources to the wheels. The energy source 1 is unidirectional (ICE) while the energy source 2 is bidirectional and can deliver power from the load. The main modes of functioning are:

- The energy source 1 alone delivers its power to the load

- The energy source 2 alone delivers its power to the load

- The energy source 2 sinks power from the load (regenerative braking)

- The energy source 1 sources power to energy source 2 and to the load

- Both energy sources deliver their power to the load simultaneously

- The energy source 1 delivers its power to the energy source 2

- The energy source 2 sinks power from the load and from the energy source 1
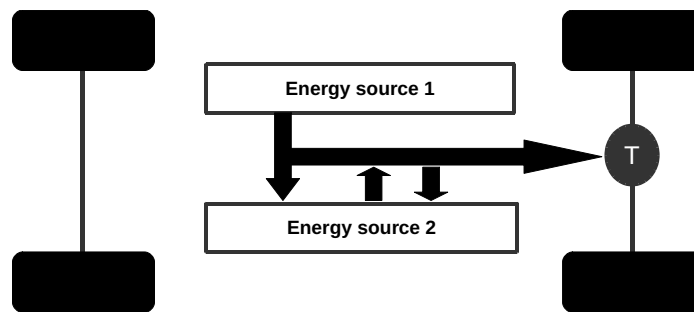

FIGURE 1.3: Power Flow in a HEV (T - Trasmission).

Figure 1.4 shows the load power of a vehicle during a driving cycle. The load power can be seen as the sum of the average power and the dynamic power. Instead of the dynamic power, mean value of the average power is different from zero. In the design of a HEV the average power is supplied by the internal combustion engines, while the dynamic power by the electric part. At the end of the driving cycle the amount of energy delivered to the load from the electric part is zero. In a HEV the electric part acts as a "power damper" and ideally it does not lose energy capacity.
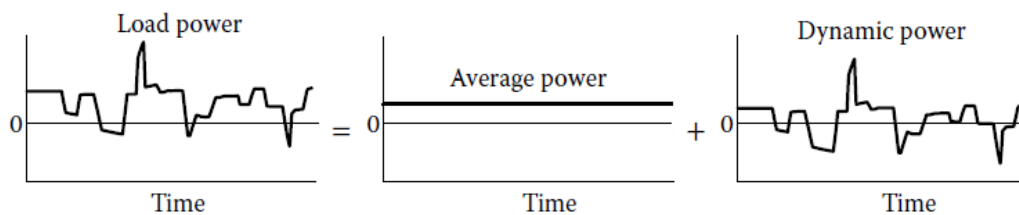

FIGURE 1.4: Vehicle driving cycle as sum of awerage power and dynamic power [1].

Different kinds of storing can be adopted: batteries, ultracapacitors, flywheel or their combinations. Various configurations have been applied by the automotive company. The choice is made upon the usage destination of the vehicle: city cars, sport utility vehicles, trucks, buses, operating machines. In this way, there are different ways to classifies a HEV, as shown in Fig. 1.2. Three groups can be considered with respect on how electric power portion is compared with the overall power:

- Micro hybrids: the level of electric power installed is no more than 5kW. The EM can do the Start & Stop and can take the place of the internal combustion engines during the low speed condition or simply it helps the driving as a boost power source. Some micro hybrids are capable of regenerative braking. Due to the small effort for the electric equipment integration and cheaper re-engineering cost, many car manufacturers have applied this solution as a start point for the "hybridization".

- Mild hybrids: typically the level of electric power installed is from 7kW to 15kW. An electric motor-generator is placed between the engines, the crankshaft and the transmission input. The motor-generator provides different functions as regenerative braking, Start & Stop and can supply some auxiliary on-board loads.

- Full hybrids: the electric power installed on-board is at least 30kW. The vehicle is able to sustain a limited full-electric range, shutting off the internal combustion engine. In this way, the complexity of the design is greater, but the full hybrid vehicle improves significantly the fuel savings and the performance.

In literature it is common to find the "Hybridization Factor" *HF* as the ratio of the electric power installed on the overall power:

$$HF = \frac{P_{EM}}{P_{EM} + P_{ICE}} \tag{1.1}$$

Figure 1.2 gives the other classification of the hybrid electric vehicle made on the configuration of on-board electric part. Three configurations are possible:

- Series: the propulsion comes only from one source.

- Parallel: the propulsion can be shared by the two sources.

- Series-Parallel: is a combination of the other configurations, but the battery can be directly charged by the internal combustion engine.

1.2.1   Series HEV

The series configuration is the simplest propulsion power flow (see Fig. 1.5). The speed and torque are controlled by the EM only. The ICE operates the generator and is task is only to charge the battery pack. This architecture is suitable both for small cars and for heavy-duty vehicles. This architecture is the simplest among the other ones, but it does not optimize the efficiency chain: the energy flows from the motor through the generator to the power converter and finally to the wheels through the EM and the mechanical transmission. This architecture can operate in different modes:

- Pure electric: the ICE is turned off and only the EM works.

- Pure engine: the battery can neither supply neither sink energy. The energy comes only by the generator towards power converter and EM act as a transmission from ICE to the wheels.

- Hybrid: the ICE and the battery supply energy together. In some case the ICE supplies both battery and EM.

- Regenerative braking: the energy is transferred from the load to the battery.

- Battery charging: the ICE is turned on for charging the battery. In some configurations the battery can be charged by an external plug-in charger.
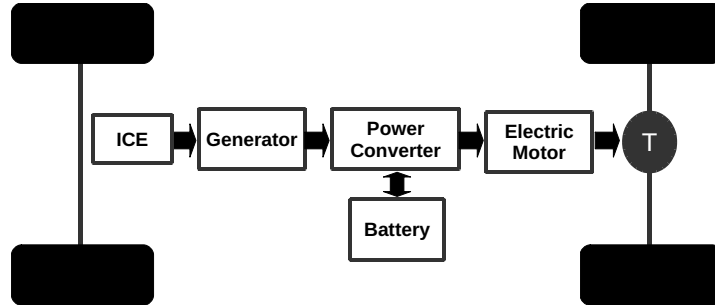

FIGURE 1.5: Series configuration of a hybrid electric vehicle.

This kind of configuration offers many advantages, as:

- because the traction is provided by an EM, the transmission system is simplified and the torque-speed profile results to be very close to the ideal one for traction. As shown in Fig. 1.6 the scope of the gearbox is to allow the ICE to operate inside an optimal and admissible speed range. The EM has a wider speed range and the gearbox may not be used.

- the working point of the ICE can be chosen properly to optimize its efficiency

- the direct driving of the wheel with two EMs can be adopted and this is suitable when is needed an advanced torque control at the wheels. This is the case of kinds of vehicles operating in difficult terrain conditions.
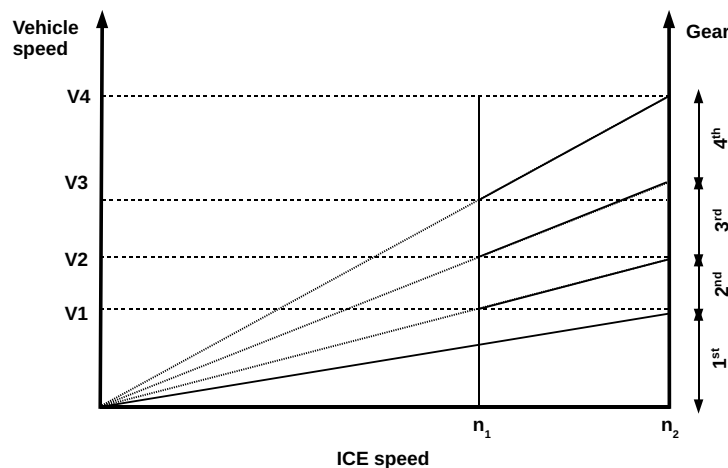

FIGURE 1.6: Vehicle speed with respect the ICE speed and gears.

Anyway the main disadvantages can be summarized in:

- the architecture does not optimize the energy flow in terms of efficiency.

- the EM is the final part of the power transmission and has to be designed in order to match all requirements in terms of vehicle performance (acceleration and dynamic performance). In the other kinds of configuration, the hybridization allows the downsizing of the single motor part because the power effort can be shared between the ICE and the EM.

1.2.2 Parallel HEV

In the parallel configuration, the ICE is assisted by the EM by means of mechanical coupling. Figure 1.7 shows the schematic architectures. There are two power flow paths: the mechanical path and the electrical path. Depending on the operating conditions of the vehicle the propulsion can work in these ways:

- the propulsion is only mechanical

- the propulsion is only electrical

- the propulsion is both electrical and mechanical

- the braking mode

- the ICE can provide propulsion and source the energy to charge the battery

Thanks to the dynamic of the electric part a quick torque response is achieved at different load and conditions. Typically the electric power is preferred at low speed and the ICE operates in the high speed range.

Due to parallel operation during the propulsion, this configuration is more compact with respect to the series configuration because of the downsizing of the ICE and of the EM. The number of conversion stages is lower and better efficiency can be obtained. Anyway, the resulting structure is more complex and the mechanical coupling is more challenging, as its control.
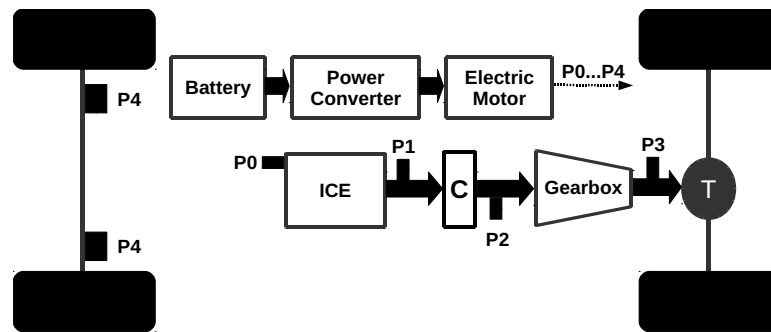

FIGURE 1.7: Parallel configuration of a HEV with P0, P1, P2, P3 and P4 implementation.

There are different ways to integrate the electric contribution along the power flow path of the vehicle [5]. From the ICE to the wheels, through the drivetrain, different mechanical point can be used to link the EM. Base on the location of the joint points, parallel HEVs are called:

- *P0*: the EM is connected to the crankshaft through the timing belt and can not be physically disconnected. This implementation is easily integrated in an already designed platform. The EM performs the classic generator function and starting motor for the ICE, providing a small torque assistance during the

driving. The efficiency of the Start & Stop is improved and energy is recovered during deceleration.

- *P1*: the EM is directly connected to the crankshaft before the clutch. It's not possible to travel in full-electric mode without particular arrangements. The Start & Stop and regenerative braking are supported by the EM, the flywheel can be completely or partially removed by proper control of the EM. The power of the EM is comparable to that of the ICE.

- *P2* and *P3*: the EM is located after the clutch (P2) or after the gearbox (P3). The decoupling from the ICE is possible and the vehicle can operate in full-electric mode. The power of the EM is comparable to that of the ICE. The P2 joint is adopted by most of mild hybrids and a set of planetary gears is employed. In other solution P2 and P3 joints coexist and are combined providing multiple operational modes improving the performance for all driving cycle topologies (urban, extra-urban and combined driving cycle).

- *P4*: in this configuration there is no mechanical connection of the EM with the rest of the power train, but the road is the only link with ICE. Therefore, the battery can be charged only when the vehicle is running. The EM is independently connected to the wheels (or to the rear axis). This solution allows the adoption of sophisticated vehicle control techniques by means the regenerative braking. The "electric support" during the acceleration phase can be maximized in terms of efficiency.

In summary, in parallel HEVs the control of the electrical and mechanical power may require to add more complexity to the design and the resulting system is more expensive.

1.2.3   Series-Parallel HEV

In the Series-Parallel configuration there are two EMs (one used as motor and one as generator) and one ICE, as shown in Fig. 1.8. By means of a planetary gear, the power flow can be managed with more flexibility. The addition of the second electric motor allows to have more efficient cycles and to obtain a better dynamic. In more general terms the "Series-Parallel" configuration can be used to indicate other types of configurations, different from that shown before. The operating modes are the same for the series architecture.
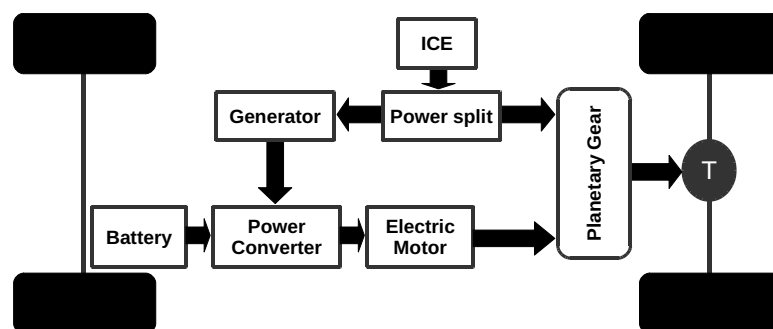

FIGURE 1.8: Series-Parallel configuration of a hybrid electric vehicle.

1.2.4 Plug-In HEV

A Plug-In Hybrid Electric Vehicle (PHEV) is a HEV that has an external plug used to charge the battery pack. The architecture can be any of that previously explained. Due to this possibility, the battery pack capability is incremented and is extended the resulting operating range of the vehicle. Figure 1.9 shows the architecture of the vehicle, which is the same as the previous ones. By means of a battery charger, the electric part can be reloaded directly from the electric grid.
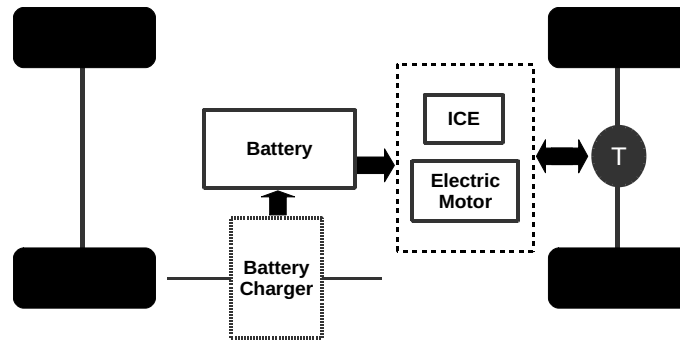
FIGURE 1.9: Plug-In Hybrid electric vehicle architecture.

1.3 Fully Electric Vehicles

A fully Electric Vehicle (EV) is a vehicle completely electrified. Nowadays, they represent the main solution for relieving the pollution problems related to transportations and gas emissions.
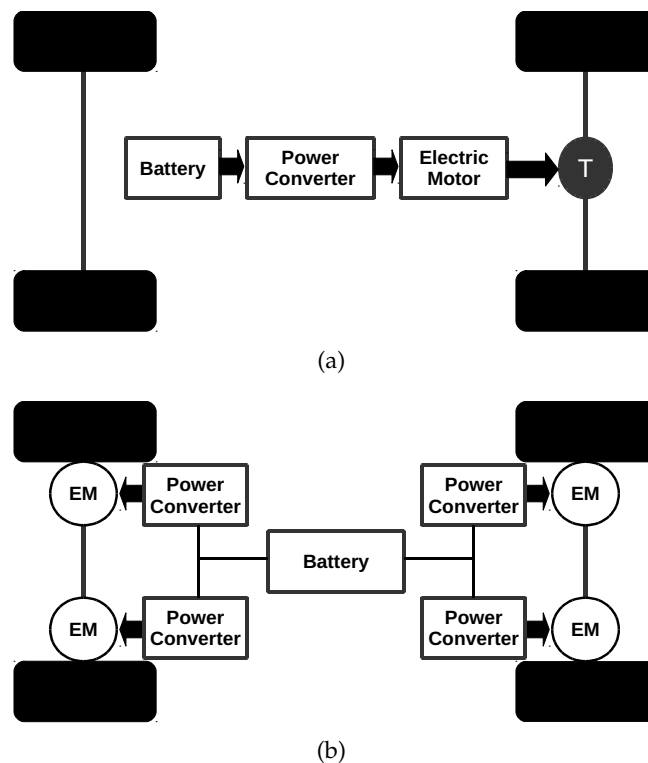
(a)

(b)

FIGURE 1.10: Fully EV structure: a) one EM with transmission; b) direct drive for each wheel.

The electricity is the only source for the power train. Electric machines are employed for this purpose. Many kinds of configuration can be adopted for an EV, Fig. 1.10 shows two kind of configurations.

The first one has only a central EM and by means of mechanical transmission, the power is transferred to the wheels. The symbol of the transmission is deliberately generic. It consists of a differential gear, gearbox and clutch. In fact, the gearbox may be adopted to match properly the operating speed of the EM with the rotating speed of the wheels.

In the second configuration is adopted the direct-drive solution [6], [7]. An EM is directly linked to each wheel and can independently be controlled. This solution simplifies the power train structure, limits the costs related to mechanical transmission and increases efficiency. However, more complexity is added to the design of the EM and more electronic is required to replace the function performed by the mechanical transmission. If the "running rules" of the vehicle are not strictly followed or the road condition changes (as the adhesion coefficient) the steering phase can be difficult. Hazards could arise and have to be managed by the control during the driving. These reasons were the main obstacles for the diffusion of this direct wheel driven configuration.

1.4 Vehicle electrical architecture and voltage level choice

The operating voltage of the on-board equipment is traditionally 12V, 24V or 48V. The choice of a *low* operating voltage (an application involving less than 60V is considered as such) brings the main advantage of electric risk reduction, but leads to use very high currents for high power applications. This requires large cross sections and more costs and weight result. When the application exceeds the ten of kilowatts the high DC voltage devices are more convenient, but safety measures are required to prevent the electric shock and the compliance with detailed standards has to be satisfied. The hazards that may be caused by high voltages are:

- Accidental arcs.

- Current flowing through the body (electric shock).

- The electromagnetic field interaction with biomedical devices (e.g pacemakers) or other kinds of interaction with the body health.

The severity of the electric shock is related to work made on the human body by the electric charge, namely to the amount of electrical current (not directly the value of the voltage) and to the amount of time it passes through the body. The resulting injuries can be distinguished in different typologies, involving the nervous system, the lesions of tissues and cells (burns and coagulation of the proteins) along the path followed by the current inside the body.

Based on these considerations [8], low voltage motor/generators are used when the required power does not exceed tens of kilowatts. This is the case of Micro and Mild hybrid vehicles. Full hybrids and full electric vehicles require higher power levels and adopt high voltage bus (300V − 400V). Typically, the electric architecture of the vehicle provides a layout with double bus system to maintain the adoption of traditional on-board low voltage equipment and guarantee safety at the same time. The high voltage bus is packaged and protected and supplies traction and the other high power loads (as HVAC). The low voltage bus, fed by the high voltage bus, is

distributed on the vehicle and supplies the other on-board equipment (infotainment, lighting system).

1.5   Battery charger typologies

The battery charger is one of the most important components for the usage of a PHEV or EV and affects the development and spread of the electric transports. The battery charger is a part of the Electric Vehicle Supply Equipment (EVSE). The main parts of EVSE are:

- Plugs and connectors

- Charging station (public or residential)

- Power outlets and protection equipment

- Battery Charger

The characteristics of the battery charger affect the lifetime and charge time of the battery pack and part of the cost of the vehicle is related to this. To match the grid requirements the battery charger may be able to sustain the grid when necessary managing a bidirectional power flow [9]. Battery charges are designed in two forms with unidirectional or bidirectional power flow:

- Off-board: the battery charger is outside from the vehicle and its efficiency is actually an important parameter to take into account during the design. With this solution, the vehicle can be recharged only if a suitable battery charger is available.

- On-board: the battery charger is placed inside the vehicle and allows battery charging at any time if necessary. In this case, many parameters have to be matched at the same time: efficiency, power density, light weight, reliability (as requested for automotive equipment).
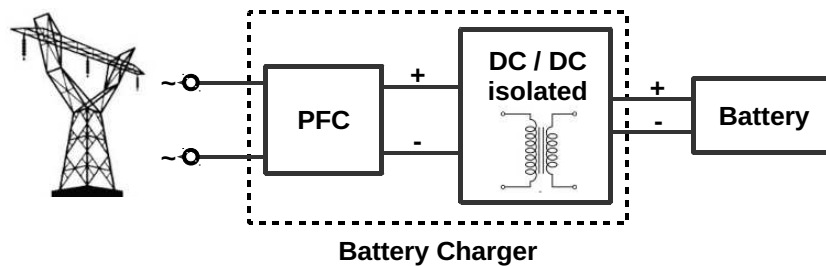

FIGURE 1.11: Battery charger simplified schematic structure.

Figure 1.11 shows the architecture of a unidirectional battery charger [10],[11]. It consists of two parts:

- The Power Factor Converter (PFC): the aim of the PFC is to correct the power factor and to regulate the output voltage. Typically the PFC is a boost converter.

- A DC/DC converter: the aim of this stage is to regulate the output voltage according to the load. Typically this converter is of step-down type and galvanic isolation is required. A suitable resonant typology is the LLC.

The power rate of the battery charger depends upon many aspects:

- size of the battery pack and life cycle

- cost

- battery technology

- equipment and effects on the grid

- required power density

- availability of charging points during the vehicle usage

- time to charge

- on-board available space and weight

With the ongoing promotion of sustainable development, more interest has been given to end-use energy efficiency and to the higher penetration of renewable energy. In the "smart grids" framework, the battery of the vehicle can be used as a storage element or can sustain the grid during peak hours. For this reason, intelligent and optimized Battery Management Systems (BMSs) are designed. The BMS of a Plug-In HEV or EV performs functions not only limited to the charge of the battery pack. Depending on:

- state of charge

- grid state and tariff setting

- energy consumption profile and habitual behaviour of the user

BMS can choose to charge the vehicle or to sustain the grid (bidirectional power flow). These two operating modes are identified as Grid to Vehicle (G2V) and Vehicle to Grid (V2G). These operations are critical because an uncoordinated charging of a huge number of vehicles can affect significantly the grid in terms of:

- increase in load profile during peak hour

- over loading of power system components

- transmission losses

- voltage/current fluctuations and ripple

- harmful harmonic pollution

- phase unbalance

- system stability

Anyway many features can also be obtained by the V2G mode, such as grid balancing, reactive power support, active power regulation and supportive of green energy sources.

Figure 1.12 summarizes the functions performed by the BMS. The aim of the system is to enhance the overall life cycle and performance of the battery pack. Protection against overcurrent, overvoltage/undervoltage, short circuit, overheating, data logging and haelth state monitoring are performed by sensors, relays and breakers incorporated into BMS and data shared with the vehicle by means of networking (GPS and CAN). The data are acquired and processed by means of functional and control algorithms. The fault diagnosis and assessment is not limited to the identification of the actual fault state. By means of input/output data record and the working state monitoring, the state of the system can be predicted and the necessary actions can be taken before the fault event.
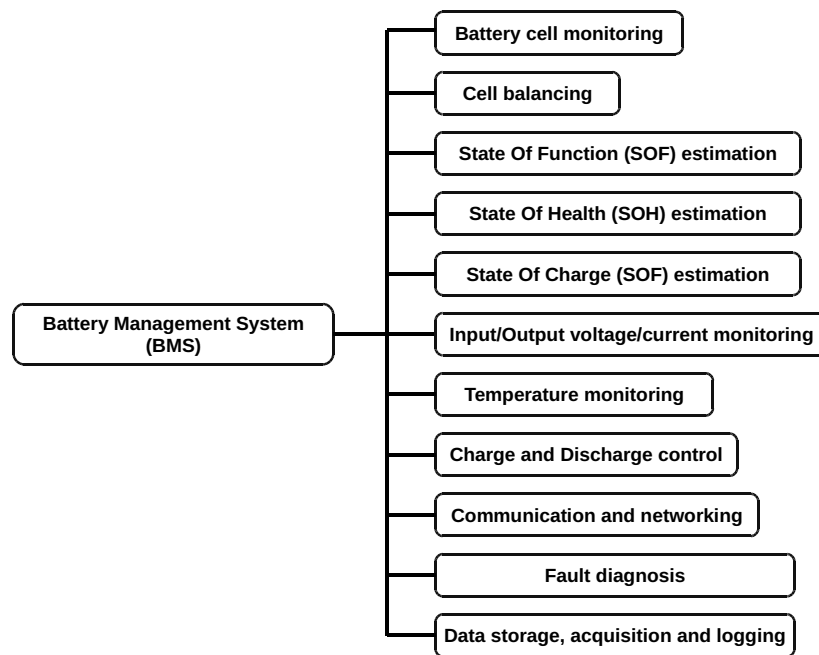

FIGURE 1.12: Functions performed by the BMS.

There are different international standards that describe charging power levels. The mainly regulatory body are: Society of Automotive Engineers (SAE), International Electrotechnical Commission (IEC) and CHAdeMO. Table 1.1 summarizes in general way the classification [12], [13].

Power Level type	Level 1	Level 2	Level 3
Power range	$< 3,7\text{kW}$	$3,7\text{kW-}22\text{kW}$	$> 50\text{kW}$
Charger topology	on-board	on-board / off-board	off-board
Grid supply	1-phase	1-phase / 3-phase	3-phase
Charging type	slow charge	semi-fast charge	fast charge
Expected charging time	11-36 hours	1-6 hours	<1 hour

TABLE 1.1: Battery chargers classification

By this classification, the Table 1.2 shows a comparison of on-board and off-board battery chargers.

on-board charger	off-board charger
Level 1 and *Level 2*	*Level 3*
Add weight and require space on vehicle	Remove weight from vehicle
BMS is managed by the vehicle	BMS is more complicated
Charging type	Slow charge

TABLE 1.2: Battery chargers comparison

1.6 Battery typologies for Electric Vehicles

Different technological characteristics should be taken into account about the type of battery for an electric vehicle. The evaluation is on energy density, power density, cost, safety, lifetime and maintenance. Various batteries and hydrogen fuel cells have the potential to succeed in commercial applications. A classification of the vehicle is made on the destination usage:

- Long-range: vehicles driven for long distance.

- Low-cost: vehicles that have as a primary concern the cost with respect to their driving. range

- High-utilization: a vehicle that experiences higher utilization as road freight vehicles.

Currently, batteries and ultra-capacitors (UCs) are the most common options. While the batteries can store many energy on-board, the UCs have high power density, long life cycle and fast-charging capability. A Fuel Cell (FC) is another solution in terms of energy density, but has a "long time constant" in terms of power source capability dynamic that require to support this technology with a storage system on the vehicle. At the present there is not a technology matching all requirements for a vehicle.

The battery technology used for EVs are listed in the following (see Fig. 1.13) [14], [15], [16]:

- Lead-Acid: the spongy lead is the negative active material, lead oxide is the positive active material and diluted sulfuric acid is the electrolyte. This is mature low-cost technique related to 50 years of usage technology and the main advantages are massive production already available. The lead battery has poor energy and power density due to the weight and can not operate in deep discharge over 20% of its rated capacity. They take much time to charge. Many research activities have been made on this technology by Advanced Lead Acid Battery Consortium [17]. The aim is to increase the performance of carbon-enhanced lead batteries in order to make sure they will continue being the choice in automotive and storage applications. The research activity has concentrated on: new cells design to enhance charge and discharge ability, adding carbon and other additives to avoid the degradation of the negative plate and study of proper battery management.

- Nickel-Cadmium (Ni-Cd): this battery is made of nickel oxide hydroxide and metallic cadmium as positive and negative electrodes, respectively. The main advantages are long life and fully discharge without damage. Anyway, this battery is expensive and cadmium is a heavy metal dangerous for the environment.

- Nickel-Metal Hydride (NiMH): nickel oxide hydroxide is used as a positive electrode and a hydrogen-absorbing alloy as a negative electrode. The alloy is made of vanadium, nickel, titanium, aluminium and other metals. This battery can operate at high temperature, long life cycles and high energy density. This technology allows the fast-charge.

- Nickel-Zinc (Ni-Zn): this battery is suitable for high drain application and has high energy and power density. Due to the extended temperature operating range they can be used in severe working conditions. However, they suffer from poor life cycles.

- Redox Flow Battery (RFB): this technology is under research and is relatively young technology. These batteries are designed for deep charge and discharge cycles. They can support up to 10,000 cycles, have a good response to changes of load or input and the SOC can be easily and accurately measured. Further, power and energy are easily separated during the design. The power depends on the size of the reactor. The energy depends on the amount and concentration of reactants and the size of the reactants tank. These characteristics make RFB suitable for bulky storage system subject to frequent deep discharging cycles.

- Lithium-Ion (Li-ion): this technology has an excellent performance in terms of high energy density, high temperature working range, self-discharging time, specific energy and specific power. The positive electrode is made of an oxidized cobalt material and the negative electrode is made of carbon material. The lithium salt in an organic solvent is used as the electrolyte. Lithium is recyclable and can match the environmental aspect. The main disadvantages are related to the costs and protection requirement to limit current and voltage. The Li-ion batteries have five different categories:

    - Li-Cobalt (LCO)
    - Li-Manganese (LMO)
    - Li-Phosphate (LFP)
    - Lithium Nickel Manganese Cobalt Oxide (NMC)
    - Lithium Nickel Cobalt Aluminium Oxide (NCA)
    - Li-Titanate (LTO)

    The phosphate-based battery is the safest typology of Li-ion and offers a discharging rate up to 50C (suitable for high acceleration phase). However, this technology contains less energy density. Commonly LMO and NMC are mixed to improve the performance and are adopted for most EVs. Lithium Oxygen (Li-O) battery is another technology base on lithium. These batteries are theoretically ten times energy density with respect Li-ion, but the researchers are trying to extend the life cycles (limited to 50 cycles).

    Li-ion batteries still are the better compromise in terms of: energy density, power density, cost and are the most common choice for EV applications.
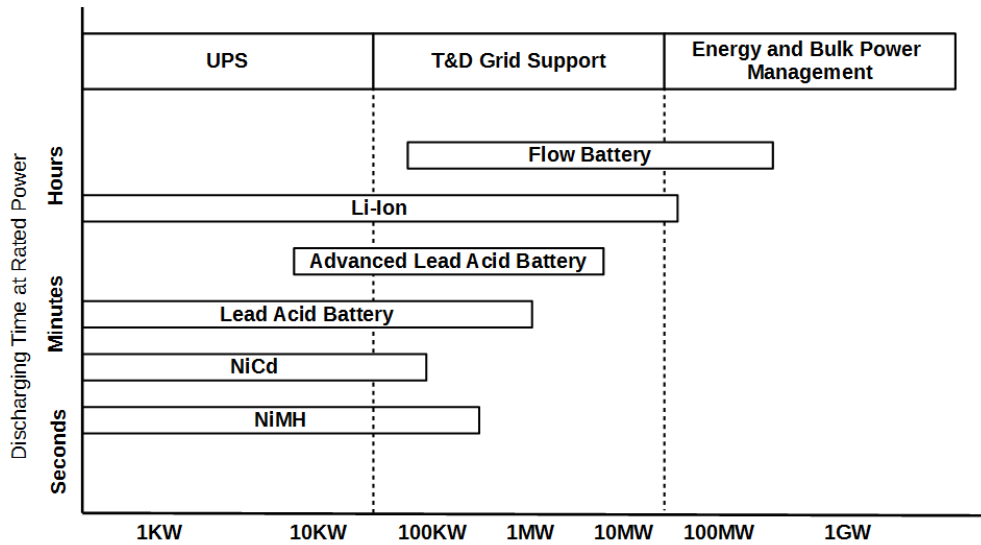
FIGURE 1.13: Battery technologies chart.

1.7 Ultracapacitors

The Ultracapacitors (UCs) store energy on two separated plates (positive and negative) divided by an insulator [18]. The structure is shown in Fig. 1.14. With respect to an ordinary capacitor, the plates have a much bigger area and the distance between them is much smaller (in this way more energy is stored inside the capacitor). In an UC the plates are made from a porous electrode metal coated. The plates are soaked in an electrolyte and separated by a thin separator (just one molecule thick). When the plates are charged up an opposite charge is formed on either side of the separator, creating an electric "double-layer". Often the UCs are referred to "double-layer capacitors". UCs are characterized by long life cycles because on the electrodes there is any chemical variation. The UCs have low energy density and high power density. They have low internal resistance and the terminal voltage is directly proportional to the state of charge. The research activity is focus to increase the surface area of the electrodes to further improve the energy storage capability. In HEVs or Full EVs both batteries and UCs are connected in parallel to cover the short-term power fluctuations. The UCs are adopted with Fuel Cell [19] for improving the performance [20] of the EV or for "dynamic" Wireless Power Transfer to supply the energy along the trip of the vehicle [21]. The UCs are very appropriate in capturing energy from regenerative braking and quickly supply energy for the acceleration phase. Five technologies are available for the electrodes:

- carbon/metal fibre composites

- foamed carbon

- carbon particulate with a binder

- doped conducting polymer films on a carbon cloth
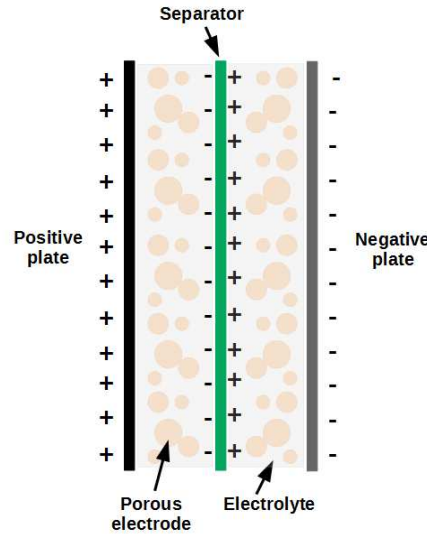
- mixed metal oxide coating on a metal foil

FIGURE 1.14: Ultracapacitor structure.

1.8 Fuel Cell

Fuel Cells (FCs) are electrochemical devices that convert the energy stored in a fuel into electrical energy through electrochemical reactions. The FCs are considered as an electrochemical conversion device and not an energy generator. Hydrogen and oxygen are combined to produce electricity and water is the final result of this reaction. They have received may attention in the last years because of their efficiency, low emission, long driving range suitability [22]. Further, the refill time is relatively short. In contrast, the major issues are related to the high cost and the lack of hydrogen refilling station infrastructures [23]. The most common FCs for an electric vehicle are the Proton Exchange Membrane Fuel Cell (PEMFC) and alkaline FC [2]. Figure 1.15 shows the operations of the two type:

- PEMFC: the electrolyte membrane is designed to allow only hydrogen ions to pass through. At the anode, the hydrogen gives up its electron with the help of the catalyst. At the cathode, the hydrogen ions, the oxygen and the electrons form water, while electrons flow from the anode to the cathode through the load.

- Alkaline FC: alkaline electrolyte only allows hydroxide to pass through. At the anode, hydrogen combined with hydroxide generates water and electrons that flow through the load. At the cathode, oxygen, water, and electrons are combined to create hydroxide.
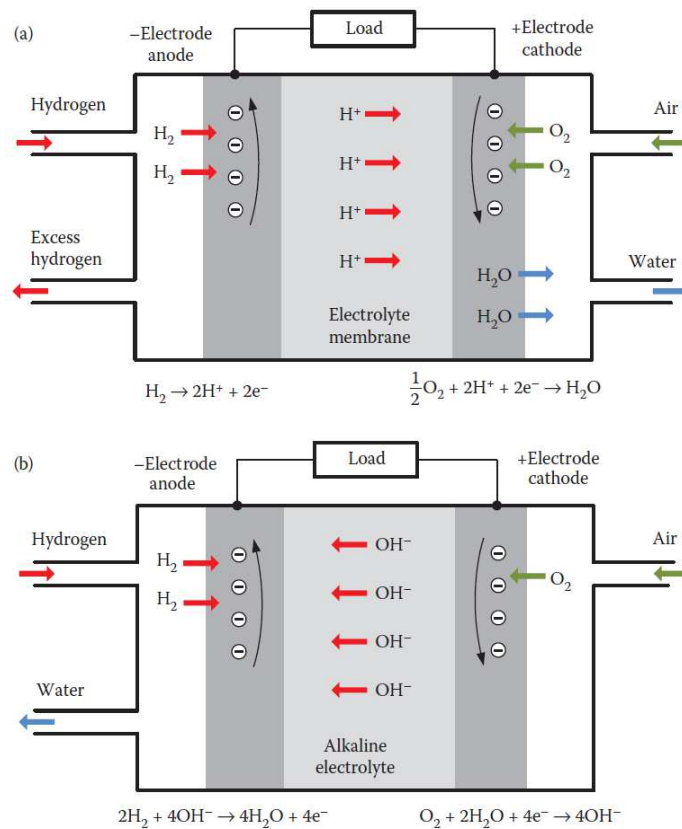
FIGURE 1.15: Fuel Cell operations: a) PEMFC, b) Alkaline FC [2].

Typically the FCs are combined with other energy storage device as UCs or batteries. During the generating phase, the UCs can assist the FCs and the energy coming from regenerative braking can be stored into the batteries. The flywheel can be a mechanical alternative way to store the energy during this phase. Figure 1.16 shows the structure of an EV equipping with FCs.
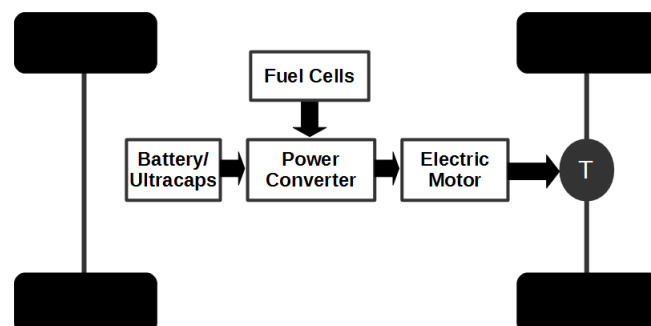

FIGURE 1.16: Structure of a EV equipped with Fuel Cells

1.9   Conclusion

This chapter has been presented with a brief introduction to green transportation. The key role of power electronics has been carried out for partial (hybrid) or total (full) vehicle electrification. The state of art of the different typologies of an electric vehicle has been investigated, highlighting how a DC-DC converter take part in the vehicle propulsion and how is interfaced to the drive train. Some of the significant aspects the design focus on are efficiency, power density, light weight, reliability, robustness, wide voltage capability. The kinds of energy sources adopted by electric vehicles are batteries and Fuel Cells, while the ultracapacitors are adopted as fast storage element to store energy during a regenerative braking phase or to stabilize the DC-link. Many kinds of technologies have been developed to build batteries and because of their characteristics, the Li-ion based is the common choice for EVs. The FCs is a promising solution to extend the range capability of the vehicle. Anyway, the high cost and the lack of hydrogen refilling station infrastructures are the major obstacles to their adoption. The battery charger is an essential part of the EVSE and many aspects make challenging its design. Some of these are size, power rate and compliance with the normative for interfacing to the grid.

In the following chapters of the treatment will be presented the design of two DC-DC power converters with wide voltage/power range capability. The converters are addressed to be the part of the electric drive of the vehicle or to be used as the power stage of the battery charger. The final part of this work deals with the electric drive developed for light vehicles. The flux-weakening strategy is adopted to extend the speed range, but some issues arise during fast torque transition. An enhanced control strategy is proposed for improving the operating region profiles.

Bibliography

[1] Mehrdad Ehsani, Yimin Gao, and Ali Emadi. *Modern Electric, Hybrid Electric, and Fuel Cell Vehicles: Fundamentals, Theory, and Design, Second Edition*. 2nd ed. CRC Press, Dec. 2017. ISBN: 9781420053982.

[2] Ali Emadi. *Advanced Electric Drive Vehicles*. 1st ed. CRC Press, Mar. 2017. ISBN: 1138072850.

[3] S. J. Rind, Y. Ren, Y. Hu, J. Wang, and L. Jiang. "Configurations and control of traction motors for electric vehicles: A review". In: *Chinese Journal of Electrical Engineering* 3.3 (Dec. 2017), pp. 1–17. ISSN: 2096-1529. DOI: `10.23919/CJEE.2017.8250419`.

[4] C. C. Chan, A. Bouscayrol, and K. Chen. "Electric, Hybrid, and Fuel-Cell Vehicles: Architectures and Modeling". In: *IEEE Transactions on Vehicular Technology* 59.2 (Feb. 2010), pp. 589–598. ISSN: 1939-9359. DOI: `10.1109/TVT.2009.2033605`.

[5] Wei Liu. *Hybrid Electric Vehicle System Modeling and Control*. 2nd ed. Wiley, Apr. 2017. ISBN: 9781119279327.

[6] Guilin Tao, Zhiyum Ma, Libing Zhou, and Langru Li. "A novel driving and control system for direct-wheel-driven electric vehicle". In: *IEEE Transactions on Magnetics* 41.1 (Jan. 2005), pp. 497–500. ISSN: 1941-0069. DOI: `10.1109/TMAG.2004.838999`.

[7] R. Hou, L. Zhai, T. Sun, Y. Hou, and G. Hu. "Steering Stability Control of a Four In-Wheel Motor Drive Electric Vehicle on a Road With Varying Adhesion Coefficient". In: *IEEE Access* 7 (2019), pp. 32617–32627. ISSN: 2169-3536. DOI: `10.1109/ACCESS.2019.2901058`.

[8] Lorenzo Morello Giancarlo Genta. *The Automotive Chassis Volume 2: System Design*. 2nd ed. Springer, Aug. 2016. ISBN: 9402404848.

[9] H. N. de Melo, J. P. F. Trovão, P. G. Pereirinha, H. M. Jorge, and C. H. Antunes. "A Controllable Bidirectional Battery Charger for Electric Vehicles with Vehicle-to-Grid Capability". In: *IEEE Transactions on Vehicular Technology* 67.1 (Jan. 2018), pp. 114–123. ISSN: 1939-9359. DOI: `10.1109/TVT.2017.2774189`.

[10] A. Stippich et al. "Key components of modular propulsion systems for next generation electric vehicles". In: *CPSS Transactions on Power Electronics and Applications* 2.4 (Dec. 2017), pp. 249–258. ISSN: 2475-742X. DOI: `10.24295/CPSSTPEA.2017.00023`.

[11] M. Grenier, M. G. Hosseini Aghdam, and T. Thiringer. "Design of on-board charger for plug-in hybrid electric vehicle". In: *5th IET International Conference on Power Electronics, Machines and Drives (PEMD 2010)*. Apr. 2010, pp. 1–6. DOI: `10.1049/cp.2010.0101`.

[12]   S. Habib, M. M. Khan, F. Abbas, L. Sang, M. U. Shahid, and H. Tang. "A Comprehensive Study of Implemented International Standards, Technical Challenges, Impacts and Prospects for Electric Vehicles". In: *IEEE Access* 6 (2018), pp. 13866–13890. ISSN: 2169-3536. DOI: 10.1109/ACCESS.2018.2812303.

[13]   M. C. Falvo, D. Sbordone, I. S. Bayram, and M. Devetsikiotis. "EV charging stations and modes: International standards". In: *2014 International Symposium on Power Electronics, Electrical Drives, Automation and Motion*. June 2014, pp. 1134–1139. DOI: 10.1109/SPEEDAM.2014.6872107.

[14]   E. Chemali, M. Preindl, P. Malysz, and A. Emadi. "Electrochemical and Electrostatic Energy Storage and Management Systems for Electric Drive Vehicles: State-of-the-Art Review and Future Trends". In: *IEEE Journal of Emerging and Selected Topics in Power Electronics* 4.3 (Sept. 2016), pp. 1117–1134. ISSN: 2168-6785. DOI: 10.1109/JESTPE.2016.2566583.

[15]   Zachary P. Cano et al. "Batteries and fuel cells for emerging electric vehicle markets". In: *Nature Energy* 3 (Apr. 2018), pp. 279–289. DOI: 10.1038/s41560-018-0108-1.

[16]   M. A. Hannan, M. M. Hoque, A. Hussain, Y. Yusof, and P. J. Ker. "State-of-the-Art and Energy Management System of Lithium-Ion Batteries in Electric Vehicle Applications: Issues and Recommendations". In: *IEEE Access* 6 (2018), pp. 19362–19378. ISSN: 2169-3536. DOI: 10.1109/ACCESS.2018.2817655.

[17]   A. Cooper and P. Moseley. "Advanced Lead-Acid Batteries – the Way forward for Low-Cost Micro and Mild Hybrid Vehicles". In: *World Electric Vehicle Journal* 3 (Mar. 2009). DOI: 10.3390/wevj3010061.

[18]   A. Khaligh and Z. Li. "Battery, Ultracapacitor, Fuel Cell, and Hybrid Energy Storage Systems for Electric, Hybrid Electric, Fuel Cell, and Plug-In Hybrid Electric Vehicles: State of the Art". In: *IEEE Transactions on Vehicular Technology* 59.6 (July 2010), pp. 2806–2814. ISSN: 1939-9359. DOI: 10.1109/TVT.2010.2047877.

[19]   Y. Wu and H. Gao. "Optimization of Fuel Cell and Supercapacitor for Fuel-Cell Electric Vehicles". In: *IEEE Transactions on Vehicular Technology* 55.6 (Nov. 2006), pp. 1748–1755. ISSN: 1939-9359. DOI: 10.1109/TVT.2006.883764.

[20]   H. Yoo, S. Sul, Y. Park, and J. Jeong. "System Integration and Power-Flow Management for a Series Hybrid Electric Vehicle Using Supercapacitors and Batteries". In: *IEEE Transactions on Industry Applications* 44.1 (Jan. 2008), pp. 108–114. ISSN: 1939-9367. DOI: 10.1109/TIA.2007.912749.

[21]   A. F. Burke. "Batteries and Ultracapacitors for Electric, Hybrid, and Fuel Cell Vehicles". In: *Proceedings of the IEEE* 95.4 (Apr. 2007), pp. 806–820. ISSN: 1558-2256. DOI: 10.1109/JPROC.2007.892490.

[22]   J. Lai and M. W. Ellis. "Fuel Cell Power Systems and Applications". In: *Proceedings of the IEEE* 105.11 (Nov. 2017), pp. 2166–2190. ISSN: 1558-2256. DOI: 10.1109/JPROC.2017.2723561.

[23]   D. Wood. "Impacting Rapid Hydrogen Fuel Cell Electric Vehicle (FCEV) Commercialization". In: *Impacting Commercialization of Rapid Hydrogen Fuel Cell Electric Vehicles (FCEV): System Cost Reduction and Subcomponent Performance Enhancement*. SAE, 2016, pp. i–xviii. ISBN: 9780768083002. URL: https://ieeexplore.ieee.org/document/8504519.

Chapter 2

LLC resonant converter design

2.1 Introduction to resonant converters

The onset of EV mobility opened the way to the widespread adoption of various on-board power electronics converters for the electric drivetrain. Switching converters are used to drive the electrical motor or to supply various on-board electric loads. Even on modern EV, the low voltage on-board system was inherited from the internal combustion engine (ICE) vehicles without particular adaptations: a large number of auxiliary functions of the vehicle depend on the on-board low voltage power supply and among them, many are related to the safety of the vehicle and of the driver: electric power steering, anti-lock braking system, lighting systems, electronic ignition, regenerative systems [1]. In an EV, a galvanically insulated auxiliary power module of suitable power size is employed to interface the high-voltage main energy storage battery to the low voltage (12V/24V/48V) auxiliary loads [2]. The desired features of the converter are high efficiency, high power density, compactness and size reduction, low weight, low Electromagnetic Interference (EMI). By increasing the switching frequency can be reduced the size of the power converter, especially of passive component like magnetics. However, the switching losses are directly proportional to switching frequency and traditional PWM converters suffer efficiency with higher switching frequency, in terms of thermal management and size reduction. The development of architectures with Zero Voltage Switching (ZVS) operation, like resonant topologies, has been a cornerstone of this effort. Figure 2.1 shows the architecture of a resonant converter with the fundamental blocks. A square wave voltage is produced from the DC source by the switching network. The spectrum contains the fundamental switching frequency plus harmonics. The generated AC wave is applied to the input of the resonant tank. The resonant tank consists of L-C networks whose voltage and current waveform vary during every switching period. The resonant tank results to be transparent when the switching frequency matches its resonant frequency. The output waveforms are essentially sinusoidal and in this case, the amplitude of the voltage and current waves is not altered. The magnitude of the current and voltage applied to the load can be controlled by changing the switching frequency (increasing or decreasing). Typically a transformer is adopted for obtaining galvanic insulation. The most popular topologies of resonant converters are (see Fig. 2.2):
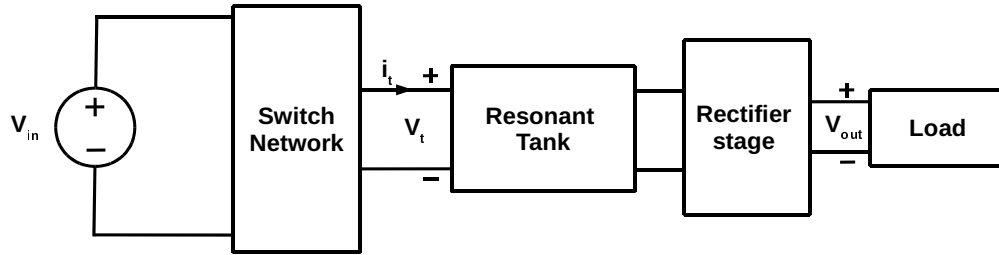
FIGURE 2.1: Resonant Converter Basic Structure.

- Series Resonant Converter (SRC): the resonant tank is in series with respect to the load. This configuration is not a good candidate for DC/DC converter due to light load regulation problem, high circulating energy and turn-off current at high input voltage. As advantages, it has an intrinsic short circuit protection and possible DC voltage block.

- Parallel Resonant Converter (PRC): the resonant tank is still in series with respect to the load, but the resonant capacitor is in parallel. This configuration allows step-down and step-up characteristic. Similarly to SRC problems this topology is not chosen.

- Series Parallel Resonant Converter (SPRC): the resonant tank has three resonant components and is a combination of SRC and PRC configuration. This configuration present two resonant frequency (it is a multi-resonant system). The advantages of SRC and PRC configuration are merged. In LLC configuration at the resonant frequency, the ZVS operation is achieved and the efficiency is maximized.
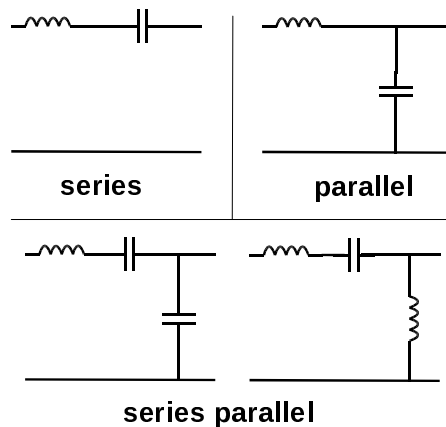
FIGURE 2.2: Resonant tank topologies

From the previous considerations, the LLC configuration is commonly adopted as a typology for a resonant converter. This typology has been widely investigated in the literature. The principal characteristics are in summary:

- Simple structure

- ZVS operation in a wide range of load conditions

- High efficiency at high input voltage

- The leakage inductance of the transformer is considered as a part of the series resonant inductor L_r. In low power application L_r can be fully integrated into the transformer.

Figure 2.3 shows two possible configurations for the switch network: full-bridge (FB) and half-bridge (HB). Although the half-bridge configuration minimizes the number of devices and the costs, the rms current is twice that of full-bridge configuration. Thus, the losses are greater and this configuration is adopted when the application has low primary currents and the power density is desired. The gain of the converter C_g is given by:

$$C_g = B_g \cdot T_g \cdot n \tag{2.1}$$

where B_g is the switch network gain, T_g is the resonant tank gain at a given frequency and n is the turns ratio of the transformer (if present). When the switch network is realized by a full-bridge the gain is equal to 1. When the half-bridge configuration is adopted the gain is equal to $0,5$. This results from the Pulse Frequency Modulation (PFM) with a fixed 50% of the duty cycle.
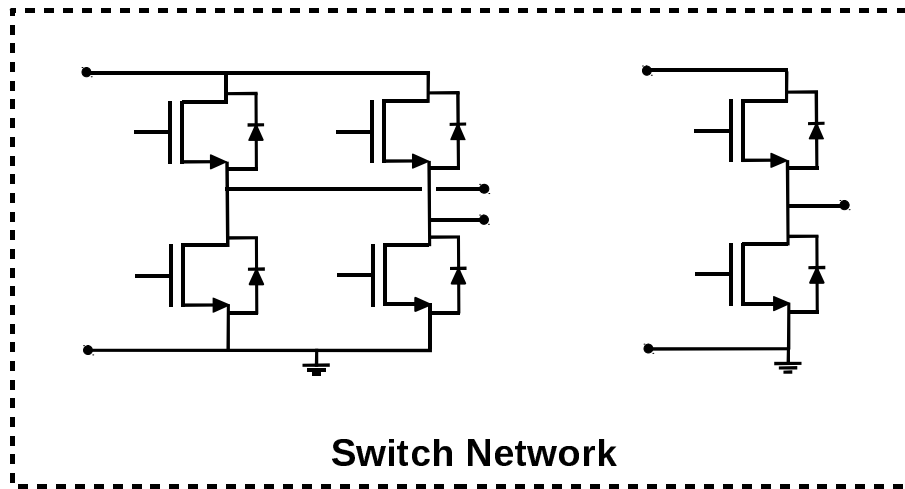
Switch Network

FIGURE 2.3: Possible configuration of the switch network: full-bridge (left side) or half-bridge (right side)

Figure 2.4 shows two different configurations of resonant tank. The traditional one includes the resonant capacitance C_r realized by a single capacitor. In the second one C_r is split in two capacitors [3] with clamping diodes. In a traditional PWM converter, the overcurrent limiting is achieved by reducing the duty cycle. For an LLC converter, this task is obtained increasing the switching frequency up to the maximum value. Then a burst modulation or duty cycle reduction are adopted as sequent action. Reducing the duty cycle the soft-switching condition is lost. The overcurrent condition occurs during overload, short circuit or at the start-up phase when the resonant capacitance is uncharged. With this configuration during an overcurrent condition:

- The voltage across the capacitors is limited to the bus voltage by clamping diodes. In this way, the resonant capacitor can be chosen of low voltage rating.

- By limiting the voltage across the capacitors the resulting maximum current of the resonant tank (and the output current as consequence) is limited each switching cycle.

- The current protection is an intrinsic characteristic of this configuration and act as soon as the overcurrent condition occurs.

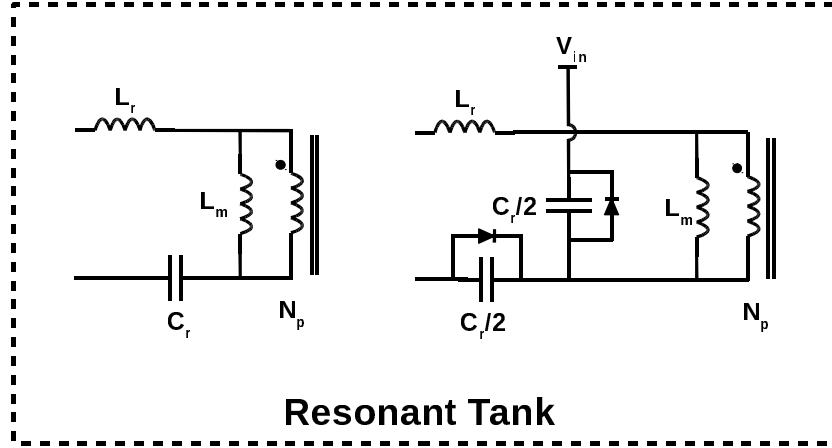- The design of resonant tank values is not affected.

FIGURE 2.4: Resonant Tank in standard configuration (left side) and with splitted resonant capacitance (right side).

The last stage of the resonant converter is the rectifier stage. It can be chosen between two types of configurations, as shown in Fig. 2.5:

- Full-bridge rectifier (the transformer has one secondary winding).

- Center tapped or "*Full wave rectifier*" (the transformer has two secondary windings).

The center tapped configuration reduces the number of diodes and the resulting conduction losses are halved with respect to the full-bridge. On the other hand, the transformer requires two identical secondaries carrying a current $\sqrt{2}$ of rms current of the full-bridge [4]. Thus, the resulting copper losses are twice. The diodes have to sustain a double voltage with respect to the full-bridge configuration. By this consideration, the center tapped configuration is suitable for low voltage - high current applications. The diodes are replaced with MOSFETs turned on during the conduction time, to increase the efficiency. The rectification takes the name of "synchronous rectification" (known also as "active rectification").
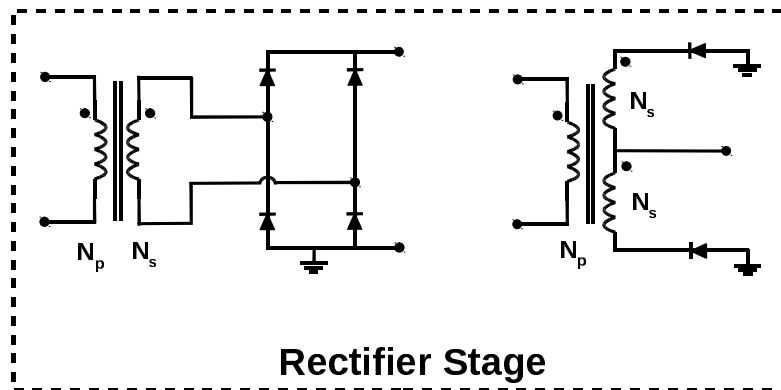

FIGURE 2.5: Rectifier stage configuration with one secondary - full-bridge rectifier (left side) and center tapped configuration (right side).

A circuit schematic representation of an LLC with resonant capacitance split and center tapped configuration with synchronous rectification is given by the Fig. 2.6.
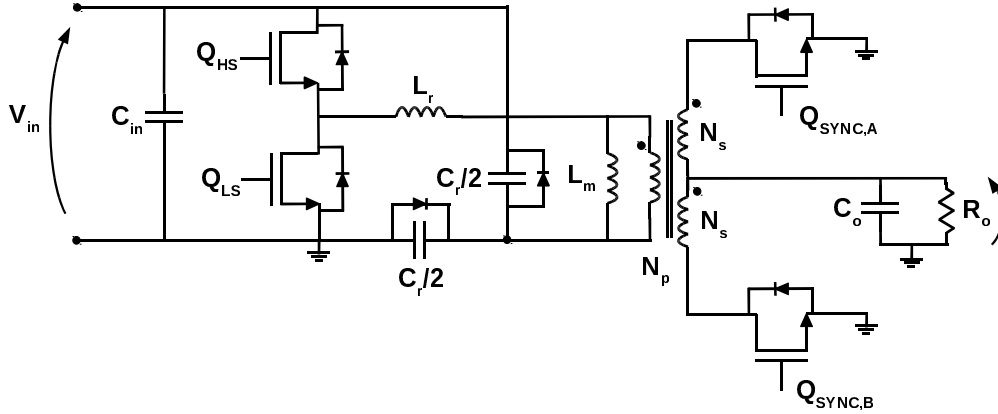

FIGURE 2.6: LLC converter circuit scheme.

The design procedure of a resonant LLC converter must take into consideration various aspects, that can be conflicting. An industry common design procedure is based on the First Harmonic Approximation (FHA) [5]. The static gain function of the LLC can be seen as a voltage gain K, namely a mathematical relation between input and output voltages, at a given frequency. Under the assumption the converter operates near to the resonant frequency, the current circulating into the resonant tank can be considered sinusoidal and all higher harmonics are ignored. Figure 2.7 shows the FHA equivalent resonant circuit. In terms of normalized resonant frequency F_x the gain K is equal to:

$$K(Q, m, F_x) = \left| \frac{V_{out}}{V_{in}} \right| = \frac{F_x^2 (m-1)}{\sqrt{(m \cdot F_x^2 - 1)^2 + F_x^2 \cdot (F_x^2 - 1)^2 \cdot (m-1) \cdot Q^2}} \qquad (2.2)$$

where:

- Quality factor:

$$Q = \frac{\sqrt{L_r/C_r}}{R_{ac}}$$

- Load seen at the primary side:

$$R_{ac} = \frac{8}{\pi^2} \cdot \frac{N_p^2}{N_s^2} \cdot R_o$$

- Normalized switching frequency:

$$F_x = \frac{f_s}{f_r}$$

- Resonant frequency:

$$f_r = \frac{1}{2\pi \sqrt{L_r \cdot C_r}}$$
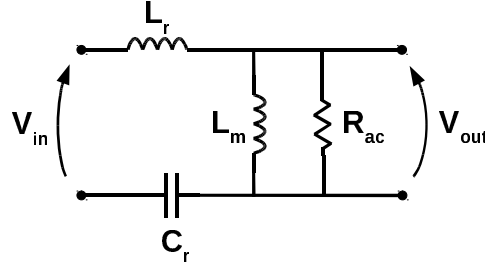
- Inductance ratio:

$$m = \frac{L_r + L_m}{L_r}$$

FIGURE 2.7: First Harmonic Approximation equivalent resonant circuit.

Figure 2.8 shows the output voltage gain K Vs frequency characteristics of an LLC converter. Three distinct regions of operation can be identified: the first and second one are zero voltage switching (ZVS) operating regions, while the third one is zero current switching (ZCS) and should be avoided. In regions 1 and 2 the behaviour is "inductive". It means that the current anticipates the voltage and as a result the reverse diode turns on before the next on-state MOSFET will conduct, providing the soft-switching condition. In Region 2, the converter acts as a boost and the output voltage can be raised above the transformer's turn ratio. Low Q values belong to lighter load, while high values represent heavy loads. All Q curves cross at the resonant frequency, where the gain of the resonant tank is equal to 1.
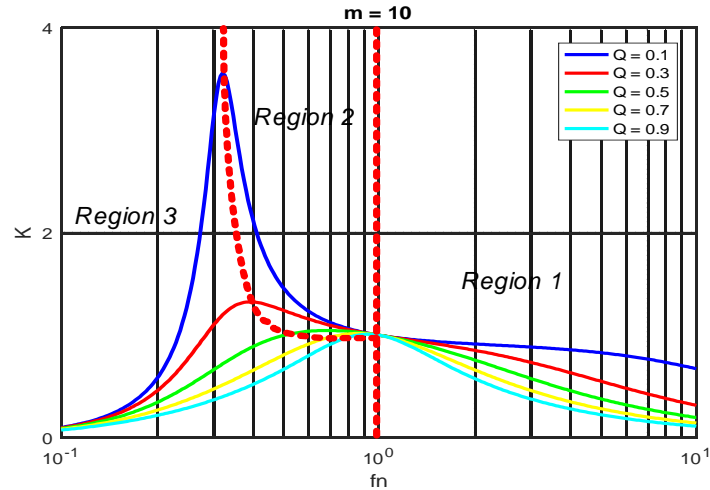
FIGURE 2.8: LLC resonant tank gain K Vs frequency of operation (normalized to resonance frequency) and different *Ro* values.

Figure 2.9 illustrates the effects of the parameter m on the gain k. Lower values of m give a higher boost gain and narrower range frequency. On the other hand, the magnetic inductance L_m is smaller and the conduction losses are greater as a result of more circulating current.
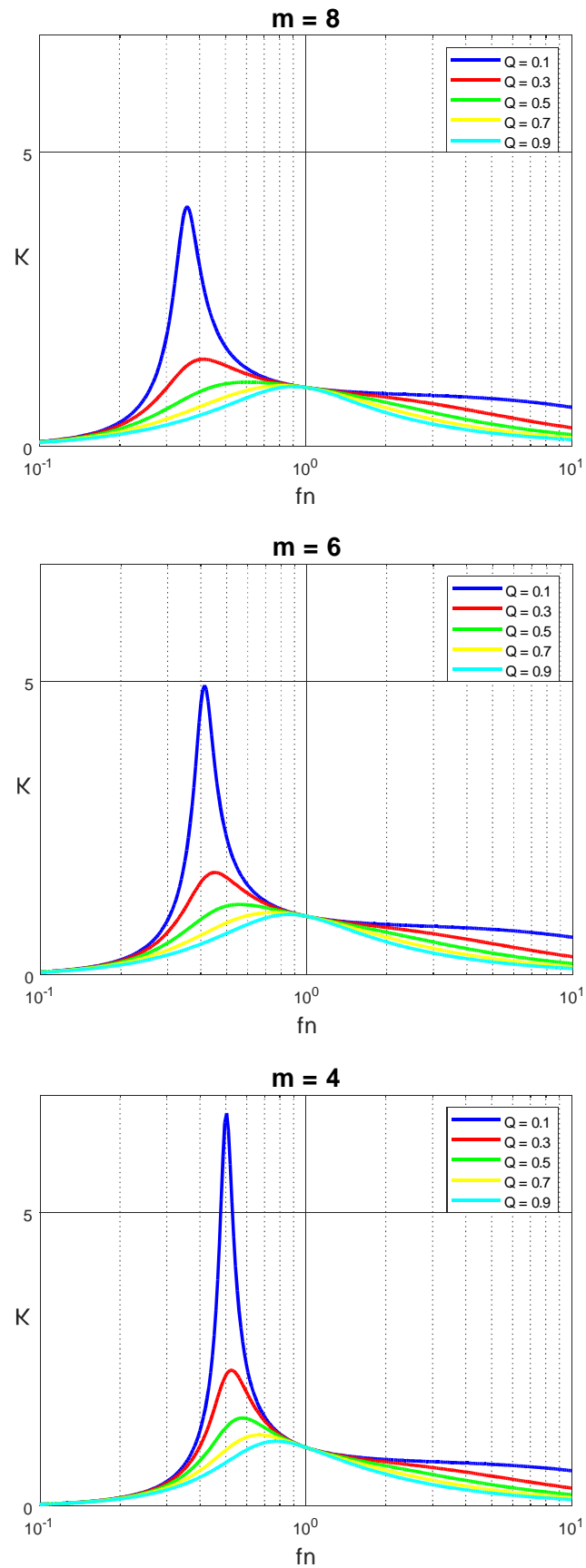
FIGURE 2.9: LLC resonant tank gain *K* for different m and Q values with respect to the normalized switching frequency.

2.2   Wide voltage LLC resonant tank design

In this section is described the design of a 2*kW* converter by referring to the schematic circuit of Fig. 2.6. The converter is designed to match the output voltage regulation range (48*V* − 20*V*) required by on-board vehicle's auxiliary loads. Table 2.1 reports the specifications of the design and the resonant tank values. The designed resonant tank is not obtained in a straightforward way. An iterative procedure is needed. Many aspects have to be considered before selecting the resonant tank values:

- The resonant capacitance value affects the voltage stress of the capacitors.

- The mechanical size restrictions affect the shape of magnetics. Starting from a core shape the magnetic inductance has to be physically realized in terms of wires and turns.

- The same aspects related to the magnetic inductance concern the resonant inductance. The minimum value is determined by the leakage inductance of the transformer that is precisely known once the transformer is designed. It can be also integrated into the transformer, but thermal losses are added to the core.

- The design has to consider the tolerance about 20% on the value of the realized magnetics.

- Once the resonant tank values have been selected, the converter is modelled on software as PLECS and current waveform are simulated. The capacitors part number, the magnetic cores shape and relative wire windings can be selected. Typically, the resonant tank values are redefined on the basis of physical realizability of the magnetics (dimensional and mechanical constraints, core losses, saturation) and costs of the components.

Name	Value
V_{in} [V]	390
V_{out_max} [V]	50
V_{out_nom} [V]	48
V_{out_min} [V]	20
P_{out_max} [W]	2000
I_{out_max} [A]	42

TABLE 2.1: LLC specification and resonant tank values

The first parameter selected is the transformer's turns ratio n. Considering that the maximum efficiency of a resonant converter is obtained at the resonant frequency, the turns ratio is determined in order to obtain the nominal output voltage at the resonant frequency. The converter gain C_g is given by the eq. 2.1 at the resonant frequency when the half-bridge configuration is selected as Switching Network:

$$C_g = \frac{Vout}{Vin} = 0.5 \cdot 1 \cdot n \Rightarrow n = \frac{V_{out}}{0.5 \cdot V_{in}} \tag{2.3}$$

In this way the turns ratio is equal to:

$$n = \frac{N_s}{N_p} = \frac{V_{out}}{0,5 \cdot V_{in}} = \frac{48}{0,5 \cdot 390} = \frac{1}{4} \tag{2.4}$$

The quality factor is selected using the plot of Fig. 2.10 obtained for a given *m* value. As the figure shows, HB switching frequency is the principal mean of regulation of an LLC converter, as there is an inverse relationship between frequency and power delivered to the output. It is to be pointed out that in case of light load operation / low output voltage regulation, an operating frequency significantly higher than the resonance frequency is required. The value of Q is such that the curve of the gain K crosses both horizontal lines, representing the maximum and minimum gain requested to regulate the maximum and minimum output voltage. At the same time, a narrow regulation frequency range is desired. It's convenient for the design to take a good margin for the nominal output voltage. A maximum output voltage is chosen to allow the regulation into the ZVS region below the resonant frequency.
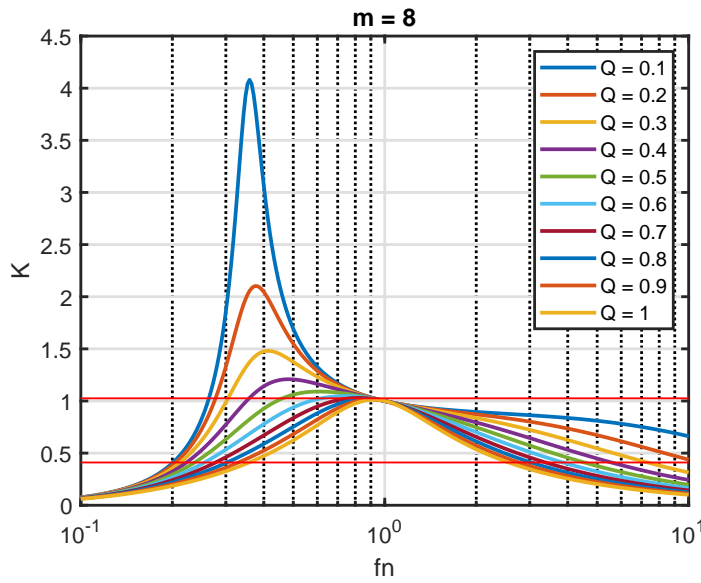
FIGURE 2.10: Static gain K for different Q values and a given m with respect to the normalized switching frequency.

Once the resonant frequency f_r, the quality factor Q and the inductance ratio m are known, the resonant tank parameters can be calculated as:

$$
\begin{aligned}
C_r &= \frac{1}{2\pi f_r Q_{max} R_{ac}} \\
f_r &= \frac{1}{2\pi \cdot \sqrt{L_r \cdot C_r}} \\
L_r &= (Q_{max} R_{ac})^2 \cdot C_r \\
L_m &= (m-1) \cdot L_r
\end{aligned}
\tag{2.5}
$$

The resulting values obtained by this iterative process are listed in Tab. 2.2.

Name	Value
C_r [μF]	324
L_r [μH]	38
L_m [μH]	250
f_r [kHz]	45
$n = N_s/N_p$	1/4

TABLE 2.2: Resonant tank values and transformer turns ratio.

Figure 2.11 shows the static gain in two conditions at nominal output power :

- The intersection between the blue Q curve and the horizontal blue line corresponds to the working point for maximum output voltage. The converter operates at a switching frequency lower than the resonant frequency in the boost region.

- The green Q curve and the horizontal green line corresponds to the working point for minimum output voltage. The converter operates at a switching frequency not too far from the resonant frequency.
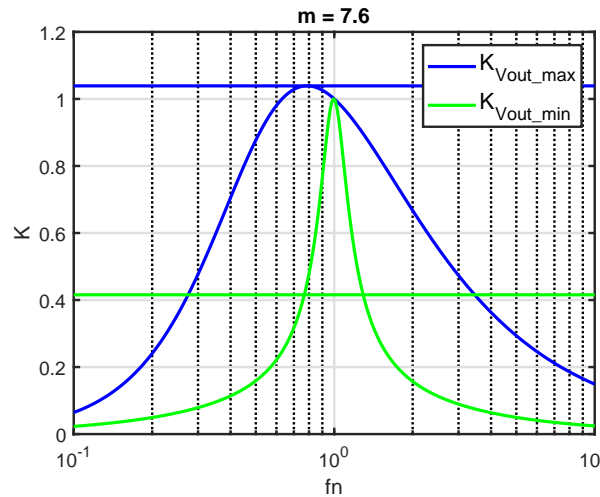
FIGURE 2.11: K curves resulting from the resonant tank and maximum output current listed in Tab. 2.1 with respect to the normalized switching frequency.

2.2.1 Transformer Design

The power transformer is a critical element of the LLC resonant converter. Many aspects make the design difficult and have to be satisfied at the same time. The main ones concern the dimensional constraint and thermal management. The final definition of the design procedure is the core shape, the number of primary and secondary turns, the air gap. Other aspects to be defined are the typology of wires used for the primary and secondary windings (litz wire or single strand) and their section. In Appendix A are given the fundamentals of electromagnetism useful for the theory behind the magnetic cores design.

Figure 2.12 shows the reference condition design of a impressed voltage transformer. In Fig. 2.13 is given a simplified illustration of a magnetic core. The iron

section A_{fe} and the number of turns N are determined in order to keep magnetic flux density below the maximum admissible value. Considering the Faraday-Lenz law it can be written:

$$|V_{\max}| = \frac{\Delta \phi_c}{\Delta t} \qquad (2.6)$$

where ϕ_c is the flux linked, equal to the product of the number of turns N, the section A_{fe} and the magnetic flux density B:
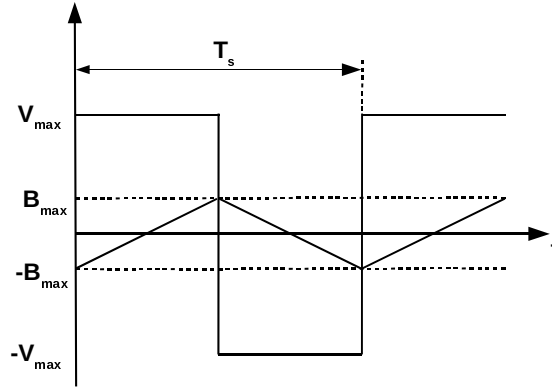
$$\phi_c = N \cdot A_{fe} \cdot B \qquad (2.7)$$

FIGURE 2.12: Impressed voltage transformer working condition.
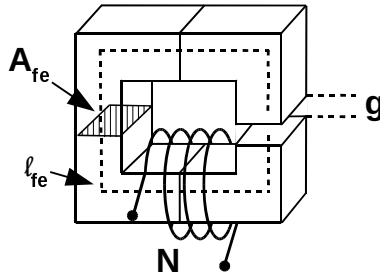
FIGURE 2.13: Magnetic core with turns N and sectional area A_{fe}.

Looking at the Fig. 2.12, where T_s is the switching period (defined by the switching frequency $f_s = 1/T_s$), the expression of V_{max} becomes:

$$V_{\max} = \frac{N \cdot A_{fe} \cdot 2B_{\max}}{\frac{T_s}{2}} = 4N \cdot A_{fe} \cdot B_{\max} \cdot f_s \qquad (2.8)$$

Rearranging the terms is possible to obtain a formula to compute the number of turns:

$$N = \frac{V_{\max}}{4 \cdot A_{fe} \cdot B_{\max} \cdot f_s} \qquad (2.9)$$

Considering the turn ration $n = N_s/N_p$ and the number of the primary turns N, given by the eq. 2.9, the number of secondary turns is equal to:

$$N_s = n \cdot N_p \qquad (2.10)$$

From the *rms* value of the current at the primary side $i_{p,rms}$ and secondary side $i_{s,rms}$, the respective sectional areas of the coils S_p and S_s are obtained considering the current density J_a:

$$
\begin{aligned}
S_p &= \frac{i_{p,rms}}{J_a} \\
S_s &= \frac{i_{s,rms}}{J_a}
\end{aligned}
\tag{2.11}
$$

If the litz wire is chosen, the values obtained are used as "equivalent sectional area" and are used to select the proper typologies.

The magnetic inductance L_m is realized with the air gap g. By the definition of inductance:

$$
L_m = \frac{N_p^2}{R}
\tag{2.12}
$$

where the reluctance R is given by: the permeability of iron μ_{fe} and air μ_0, the magnetic path length through the iron l_{fe}, the air gap g and the respective cross sectional areas A_{fe} and A_0:

$$
R = \frac{l_{fe}}{\mu_{fe} A_{fe}} + \frac{g}{\mu_0 S_0}
\tag{2.13}
$$

From the expression of eq. 2.12 and eq. 2.13 is possible to obtain the value of g for a given L_m and number of turns N:

$$
g = \left(\frac{N^2}{L_m} - \frac{l_{fe}}{\mu_{fe} A_{fe}} \right) \mu_0 A_0
\tag{2.14}
$$

Once the air gap is defined two checks have to be verified: the air gap has to be physically realizable (normally no more than 1mm are admissible) and the available window area A_w of the selected core has to be sufficient to contain the coils. The required window area $A_{w,r}$ can be computed by sequent formula, where k_f is the filling factor. A practical value of k_f typically is $0,6$:

$$
A_{w,r} = \frac{N_s A_s + N_p A_p}{k_f} < A_w
\tag{2.15}
$$

The transformer is realized as "center tapped" as shown by the schematic circuit of Fig. 2.14. The design of the transformer is made with the parameters listed in Tab. 2.3. The parameters were obtained simulating the converter on PLECS using the converter characteristics shown in Tab. 2.1 and in Tab. Tab. 2.2 at the nominal output voltage and maximum output power. The switching frequency considered for the design is the resonant frequency with a certain margin. As can be seen in Fig. 2.11 the transformer operates at a lower switching frequency when maximum voltage is regulated at the output.
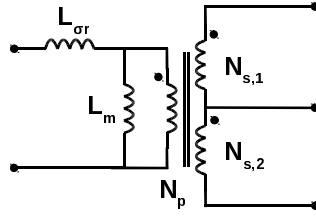
FIGURE 2.14: Trasformer Center Tapped.

Parameter	Value
Current density J_a $[\text{A}/\text{m}^2]$	6
Primary rms winding current $i_{rms,p}$ $[\text{A}]$	13,4
Secondary rms winding current $i_{rms,s}$ $[\text{A}]$	37,1
Applied voltage $V_{max} = V_{in}/2$ $[\text{V}]$	195
Switching frequency, f_s $[\text{kHz}]$	40
Magnetic inductance L_m $[\mu\text{H}]$	250
Filling factor k_f	0,6

TABLE 2.3: Specification parameter for transformer design.

To realize the transformer a planar shape is chosen. Many benefits are obtained by the adoption of this typology shape [6, 7, 8]. The main ones are:

- Compactness and low package profile matching higher power density requirements and miniaturization.

- Easily terminations for multiple windings.

- Minimum losses due to skin and proximity effect [9]. It allows high working frequency (up to MHz).

- The windings are formed using common PCBs or copper plates properly isolated. Considering the scale production this reduces the cost of manufacturing.

- Optimization of the size with respect to the form factor of many applications (flat geometry of monitors, smartphones, tablet, TVs, etc.).

- Improving of the thermal management.

- Suitable technology for 3-D packaging.

Table 2.4 reports the data obtained from the datasheet of TDK ELP64 N97 core chose to manufacturing the transformer and used for the design. Figure 2.15 is an extract of its datasheet.

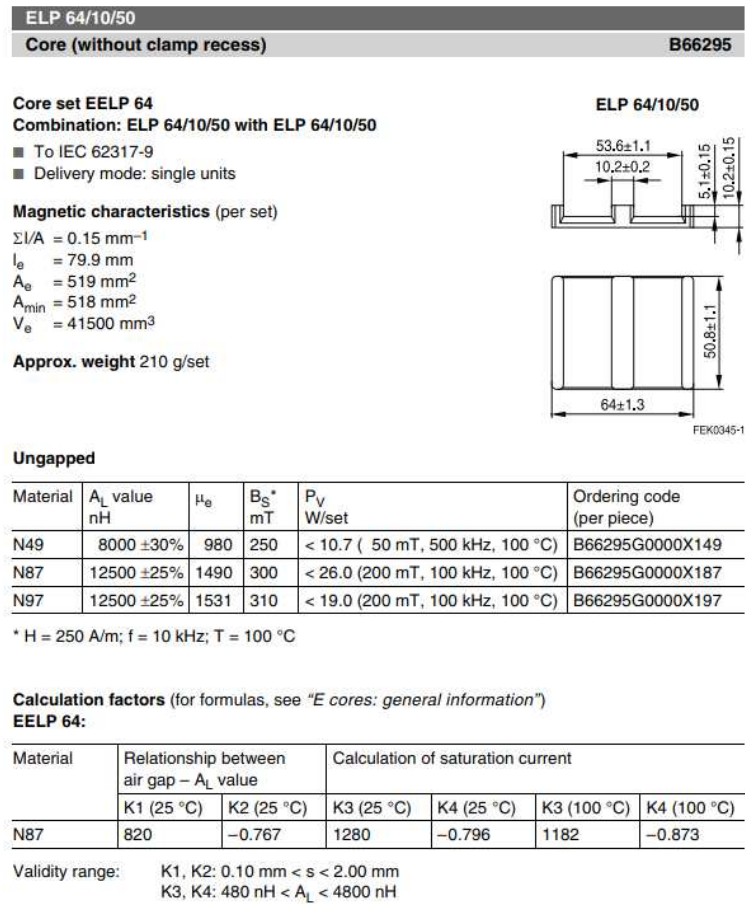| Parameter	Value
Manufacturer	TDK
Core ID	ELP 64/10/50
Material	N97
Winding area A_w [mm^2]	221, 34
Core section area A_{fe} [mm^2]	519
Maximum flux density B_{max} [mT]	290
Magnetic path lenght l_{fe} [mm]	79, 9
Iron relative magnetic permeability $\mu_{r,fe}$ [ad]	1531
Air magnetic permeability μ_o [H/m]	$1,26\mu$

TABLE 2.4: ELP64 core data

FIGURE 2.15: TDK ELP64 doc sheet extract.

Using the eq. 2.9 is possible to compute the number of turns of the primary side N_1. The applied voltage to the turns is half of the available voltage at the input due to the half-bridge configuration:

$$N_p = \frac{V_{\min}/2}{4 \cdot A_{fe} \cdot B_{\max} \cdot f_s} = \frac{195}{4 \cdot 519 \times 10^{-6} \cdot 290 \times 10^{-3} \cdot 40 \times 10^3} = 8 \qquad (2.16)$$

(a)   (b)
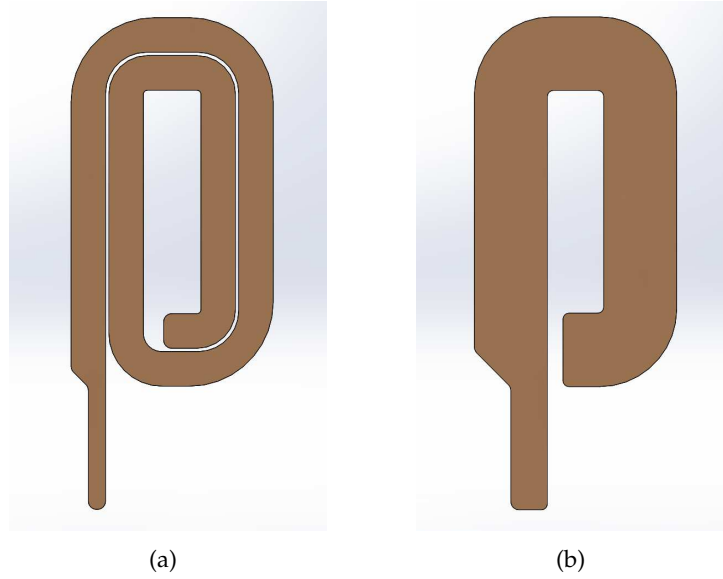
FIGURE 2.16: Rendering of single layer of primary (a) and secondary turns (b).

The secondary turns value is obtained from eq. 2.10:

$$N_2 = n \cdot N_1 = \frac{1}{4} \cdot 8 = 2 \tag{2.17}$$

The air gap value is computed with the eq. 2.14, where $A_0 = A_{fe}$ and $\mu_{fe} = \mu_{r,fe} \cdot \mu_o$:

$$
\begin{aligned}
g &= \left(\frac{N_p 1^2}{L_m} - \frac{l_{fe}}{\mu_{fe} A_{fe}} \right) \mu_0 A_0 = \\
&= \left(\frac{8^2}{250 \times 10^{-6}} - \frac{79,9 \times 10^{-3}}{(1531 \cdot 1,26 \times 10^{-6}) \cdot 519 \times 10^{-6}} \right) \cdot 1,26 \times 10^{-6} \cdot 519 \times 10^{-6} = \\
&= 0.115 \text{mm}
\end{aligned}
$$

$$\tag{2.18}$$

The eq. 2.18 refers to a generic model of a core with a single interruption along with the ferrite material (case illustrated by Fig. 2.13). Considering the E shape of the core, the air-path length is distributed over two interruptions and the distance to realize between the two core is the half value of g.

The eq. 2.11 are used to check the current density of the primary and secondary turns. The coils are realized by a copper plate of 400μm of thickness t_{cp}. Figure 2.16 shows the rendering of the primary and secondary turns. The coils are realized by laser cutting of copper plate and joined by a tin soldering process.

Coil	turns x layer	number of layers	trace width	t_{cp}
Primary	2	4	8, 6mm	400μm
Secondary	1	2	18, 1mm	400μm

TABLE 2.5: Summary of primary and secondary coil characteristics

Table 2.5 summarizes the characteristics of the primary and secondary coils. The current density is obtained from the indicated width of the trace of each layer:

$$J_{a,p} = \frac{i_{p,rms}}{S_p} = \frac{13,4}{(8,6 \cdot 0,4)} = 3,88 \frac{A}{(mm)^2}$$

$$J_{a,s} = \frac{i_{s,rms}}{S_s} = \frac{37,1}{(18,1 \cdot 0,4)} = 5,1 \frac{A}{(mm)^2}$$

(2.19)

Characteristics	value
Turns ratio N_p/N_s	1/4
Magnetic Inductance L_m [μH]	250
Leakage inductance at primary side $L_{\sigma r}$ [μH]	2,0
Air gap $g/2$ [mm]	0,05
Primary winding	**value**
Number of turns N_p	8
Current density $J_{a,1}$ [A/(mm)^2]	3,88
Secondary winding	**value**
Number of turns N_s	4
Current density $J_{a,2}$ [A/(mm)^2]	5,10
Insulation specifications	**value**
Coils to core [kV]	1,5
Primary to secondary [kV]	3
Between secondaries [kV]	functional

TABLE 2.6: Planar transformer parameters and building specifications.
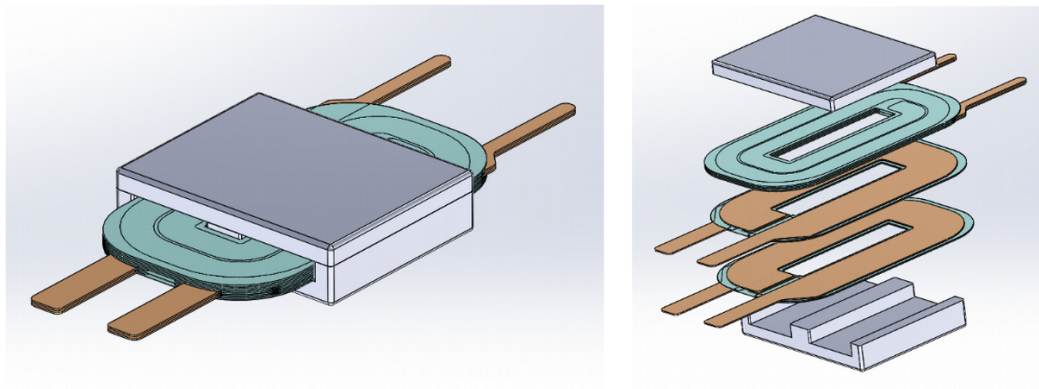
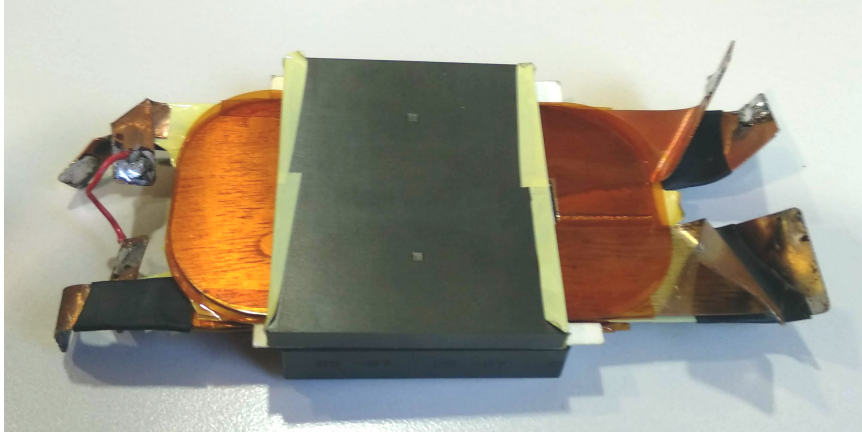FIGURE 2.17: Rendering of Planar transformer TDK ELP64/10/50 with exploded view.

FIGURE 2.18: Planar transformer made with TDK ELP64/10/50 core.

Table 2.6 summarizes the characteristics of the realized transformer. Figure 2.17 and Fig. 2.18 are the renderings and pictures of the transformer, Fig. 2.19 gives a detailed illustration of the layer stack. Each layer is separated from the other one by a 75μm Kapton HN sheet. Each layer is folded with 3M "56-YELLOW-1"X72YD*" tape to reinforce the insulation and to ensure the correct housing inside the core.
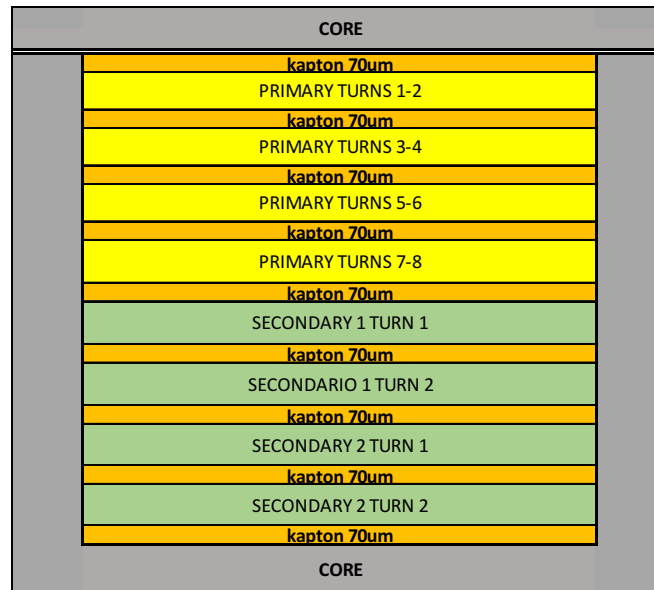

FIGURE 2.19: Trafo layer stack. Each color corresponds to a single layer with the corresponding turns as indicated by the Tab. 2.6

2.2.2 Resonant Inductor Design

The resonant inductance L_r in place at the primary side in series to the transformer as illustrated in the schematic circuit of Fig. 2.6. It realizes with the leakage inductance of the transformer $L_{\sigma,r}$ the resonance inductance of the resonance tank. The value of inductance is computed as the difference between the resonant tank series inductance and the leakage inductance of the transformer:

$$L_r = L_{r,tank} - L_{\sigma,r}$$

The design of the inductor is made on the maximum peak current i_{max} and the maximum admissible magnetic flux $\phi_{B,max}$. The parameters to be determined by the design are: the number of turns N and the air gap g. The Hopkinson's law expressed by the eq. A.28 relates the magnetic flux and linkage flux inside the core. It is used to compute the number of turns:

$$N = \frac{Li_{\max}}{\phi_{B,max}} = \frac{Li_{\max}}{B_{\max}A_{fe}} \tag{2.20}$$

Where the magnetic flux ϕ_B has been considered given by the product between the maximum magnetic flux density B_{max} and the iron cross-sectional area of the core A_{fe}.

The value of the air gap is obtained from the definition of reluctance $\mathcal{R}$:

$$\mathcal{R} = \left(\frac{l_{fe}}{\mu_{fe}A_{fe}} + \frac{g}{\mu_0 A_0} \right) \tag{2.21}$$

The expression is rearranged to make explicit the air gap and the reluctance is substituted using the definition of inductance given by the eq. A.27. The cross sectional area through the iron A_{fe} is considered to be the same through the air A_0:

$$g = \mu_0 \left(\mathcal{R}A_0 - \frac{l_{fe}}{\mu_{fe}} \right) = \mu_0 \left(\frac{N^2}{L}A_0 - \frac{l_{fe}}{\mu_{fe}} \right) \tag{2.22}$$

On the same consideration explained for the air gap of the transformer, the distance to realize between the cores is half of the computed value.

The inductor is realized according to the parameter listed in Tab. 2.7. Table 2.8 lists the characteristics of the ETD34 core.

Parameter	Value
Current density J_a [A/m^2]	4
Peak winding current i_{peak} [A]	18, 94
Peak winding current i_{rms} [A]	13, 39
Switching frequency, f_s [kHz]	40
Inductance L_r [µH]	36
Filling factor k_f	0, 5

TABLE 2.7: Specification parameter for resonant inductor design.

Parameter	Value
Manufacturer	TDK
Core ID	ELP 34/17/11
Material	N97
Winding area A_w [mm^2]	171, 10
Core section A_{fe} [mm^2]	97, 10
Maximum flux density B_{max} [mT]	340
Magnetic path lenght l_{fe} [mm]	74, 4
Iron relative magnetic permeability $\mu_{r,fe}$ [ad]	1710
Air magnetic permeability [µH/m]	1, 26

TABLE 2.8: ETD34 core data

The number of turns is obtained using the eq. 2.20:

$$N = \frac{L I_{\max}}{B_{\max} A_{fe}} = \frac{36 \cdot 18,94}{340 \times 10^{-3} \cdot 97,1 \times 10^{-6}} = 21 \qquad (2.23)$$

The air gap value is obtained by the eq. 2.22:

$$g = \mu_0 \left(\frac{N^2}{L} A_0 - \frac{l_{fe}}{\mu_{fe}} \right) =$$

$$= 1,26 \times 10^{-6} \left(\frac{21^2}{36 \times 10^{-6}} \cdot 97,1 \times 10^{-6} - \frac{70,4 \times 10^{-3}}{\left(1670 \cdot 1,26 \times 10^{-6} \right)} \right) = \qquad (2.24)$$

$$= 1,5 \text{mm}$$

The skin effect limits the cross sectional area of the conductor increasing the resistance. The skin depth δ is the section conductor's thickness effectively crossed by current. The value is a function of AC current frequency f, permeability μ and resistivity ρ:

$$\delta = \sqrt{\frac{\rho}{\pi f \mu}} \qquad (2.25)$$

To mitigate skin effect the windings are realized using the litz wire. The choice of the litz wire typology starts from the required cross section $A_{w,\delta}$. It is obtained from the current density J_a and the rms current i_{rms} flowing through the winding:

$$A_{w,\delta} = \frac{i_{rms}}{J_a} = \frac{13,39}{4} = 3,35 \text{mm} \qquad (2.26)$$

AWG 12 is the corresponding AWG standard value. The litz wire is chosen to match the switching operating frequency and the equivalent AWG section from catalogue tables. In this case, a litz of 300 strands of AWG 38 is chosen.
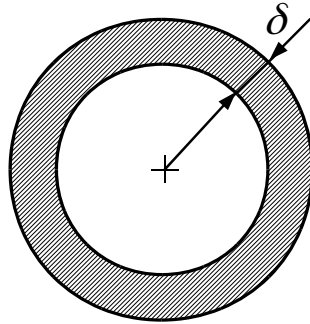

FIGURE 2.20: Skin dept δ of a wire of section $A_{w,\delta}$.

2.3 Consideration on the dead time for soft-switching operation

Resonant converters are controlled by Pulse Frequency Modulation (PFM) with fixed 0,5 duty cycle value. To guarantee soft-switching operation two conditions must be met:

- The operating point has to be inside regions 1 or 2 (see Fig. 2.8).

- A correct amount of dead time t_d has to be introduced.

Figure 2.21 shows the LLC converter schematic with parasitic capacitances and the stray resistance in evidence. The total equivalent capacitance C_{MP} seen at the midpoint of the half-bridge can be expressed as:

$$C_{MP} = 2C_{ds} + C_s \tag{2.27}$$

where C_{ds} is the "time related" equivalent drain-source capacitance [10] of the chosen devices and C_s is the stray capacitance due to PCB layout and parasitics.
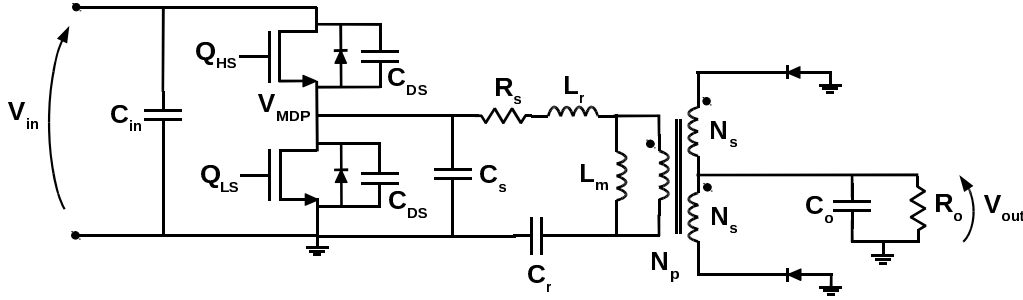

FIGURE 2.21: Circuit of LLC half-bridge converter with center-tapped output rectification stage and detailed parasitics components at primary side.

The output capacitance of a MOSFET cannot be accurately measured by a single measure. The value is drain-source voltage dependent. In a datasheet of a device are indicated two values of capacitance:

- The "energy related": it's the value measured when the output capacitance is charged with a constant current. This value is used to model energy losses. The energy stored in the output capacitance is dissipated every charge-discharge cycle.

- The "time related" capacitance: it's the value measured when the output capacitance is charged with a constant voltage. This value is taken into account for the dead time selection of a resonant converter.

In order to ensure ZVS condition over the entire operating regions, it is necessary to calculate the minimum time required to fully charge/discharge C_{MP}. This process is guaranteed by the primary current, but if the dead time is too long the current may reverse its direction and the ZVS condition is lost. Typically a maximum value of 1µs is the upper limit of dead time. Depending on the load condition different values of primary current flow at the primary side. A minimum and a maximum value of dead time are identified to fully charge C_{MP}: $t_{d-needed,min}$ and $t_{d-needed,max}$. C_{MP} is charged by the circulating current in the transformer primary winding and the worst time charge condition is the light load operation. In this case, the time that has to be guaranteed is equal to [11]:

$$t_{d-needed,max} = \frac{C_{MP} \cdot V_{DC}}{I_{pri,pk\_min}} \tag{2.28}$$

Under this condition, there is almost no current transfer to the secondary side and the current in the resonant tank is just the magnetizing current of the transformer. It is to be pointed out that under this condition the operating frequency is maximum. The value of current is equal to:

$$I_{pri,pk\_min} = \frac{V_{out}}{4 \cdot n \cdot f_{sw,max} \cdot (L_r + L_m)} \tag{2.29}$$

Hence to limit the conduction losses at full load operation, adaptive dead time between $t_{d-needed,min}$ and $t_{d-needed,max}$ was proposed and adopted in certain commercial LLC controllers. Without adaptive dead time the t_d has to be chosen equal to $t_{d-needed,max}$.

All these considerations, in particular the constraint resulting from eq. 2.28, impose an upper limit to the maximum frequency of operation (f_{MAX}) of the LLC converter. Other limiting factors are:

- Increased copper losses in the magnetic components due to skin effect.

- Limitations of peripherals resolution in case of fully digital implementations.

- Finite rise and fall time of the power semiconductors.

2.4 PWM adotption at light load condition

The industry standard modulation techniques for LLC converters is the PFM coupled with burst mode or skip-cycle operation at light load [12], Fig. 2.22(a). At light load operation, once the maximum frequency f_{MAX} is reached, the controller enters burst mode operation. The burst mode consists of a continuous switching period of fixed length, interleaved with a stop period t_{stop} of variable length. By adjusting the stop time regulation at light load is achieved, Fig. 2.22(b).
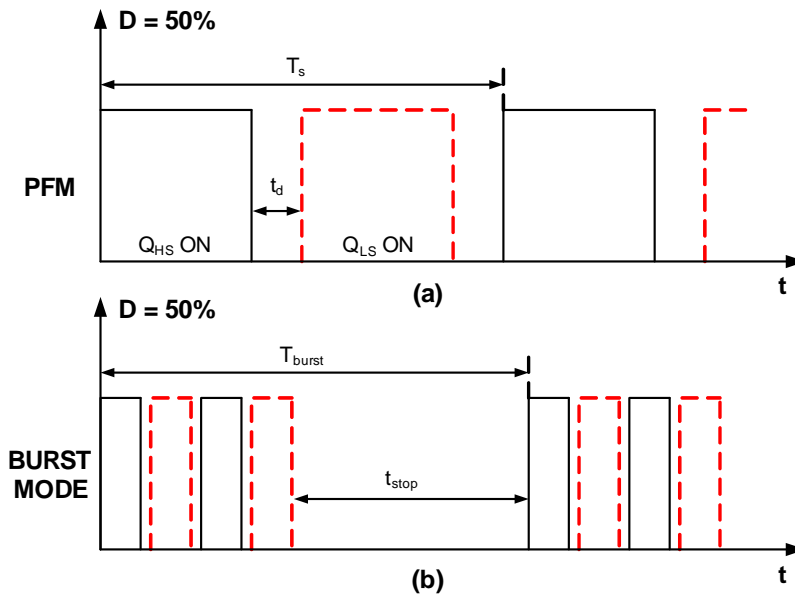

FIGURE 2.22: PFM modulation with dead time (a) and Burst Mode operation at light load (b)

In case of high power applications, characterized by wide output voltage regulation, PWM can be beneficially adopted to extend the continuous modulation operation at low output voltage / low output power. At light load operation, once f_{MAX} is reached, the controller enters PWM modulation: the frequency remains constant at the maximum value, while the duty cycle is reduced from 0,5 down to the minimum value. The simplest implementation of PWM modulation is shown in Fig. 2.23(a). With this modulation, both the high side and the low side switches have increased turn-on losses because of the presence of hard-switching commutations. Since in PWM modulation $t_{off} >> t_d$ the condition for ZVS commutation (current always leading voltage) is not guaranteed. An enhanced solution is shown in Fig. 2.23(b): the low side switch Q_L is turned on after the t_d under ZVS conditions. This kind of "asymmetric" PWM modulation is adopted by certain advanced ASIC LLC controllers [13]. With this modulation, the overall switching losses are reduced, but power dissipation is allocated to the switch that begins the PWM sequence (in this instance, Q_H). The benefit PWM over PFM coupled with burst mode or skip-cycle operation is the reduction of output voltage ripple for a given size of the required output capacitor.
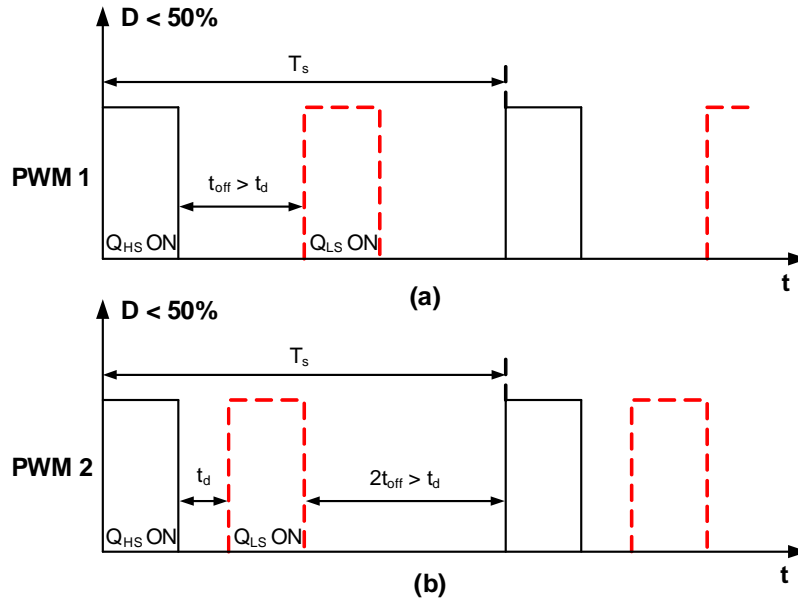
FIGURE 2.23: Classic PWM modulation with dead time (a) and enhanced PWM modulation with reduced losses (b)

2.5   Benefits of PWM on the output voltage regulation

As explained in the previous section 2.4 the PFM control regulates the frequency to a higher value for increasing the impedance of the resonant tank. In this way, the output voltage is reduced until the maximum allowable frequency is reached. The burst control is adopted to regulate the output voltage at light load condition. During t_{stop} the modulation is interrupted and a voltage ripple is experienced at the output. The voltage ripple is limited avoiding the modulation break by PWM adoption. The benefits of PWM modulation can be seen comparing Fig. 2.24 and Fig. 2.25 that report the output voltage ripple in case of burst and PWM control respectively. The captures are obtained by PLECS simulation model implementing a burst control and a PWM control. In burst mode a ripple more than 1V is associated

with each train pulse generated by the control to sustain the output voltage setpoint. Every burst cycle is composed of an equal number of turning on of the high side and low side device to avoid a DC offset on the primary side of the transformer. This constraint prevents the generation of train pulse of equal duration. This kind of instability inside the burst cycle causes some ripple having a higher peak value.
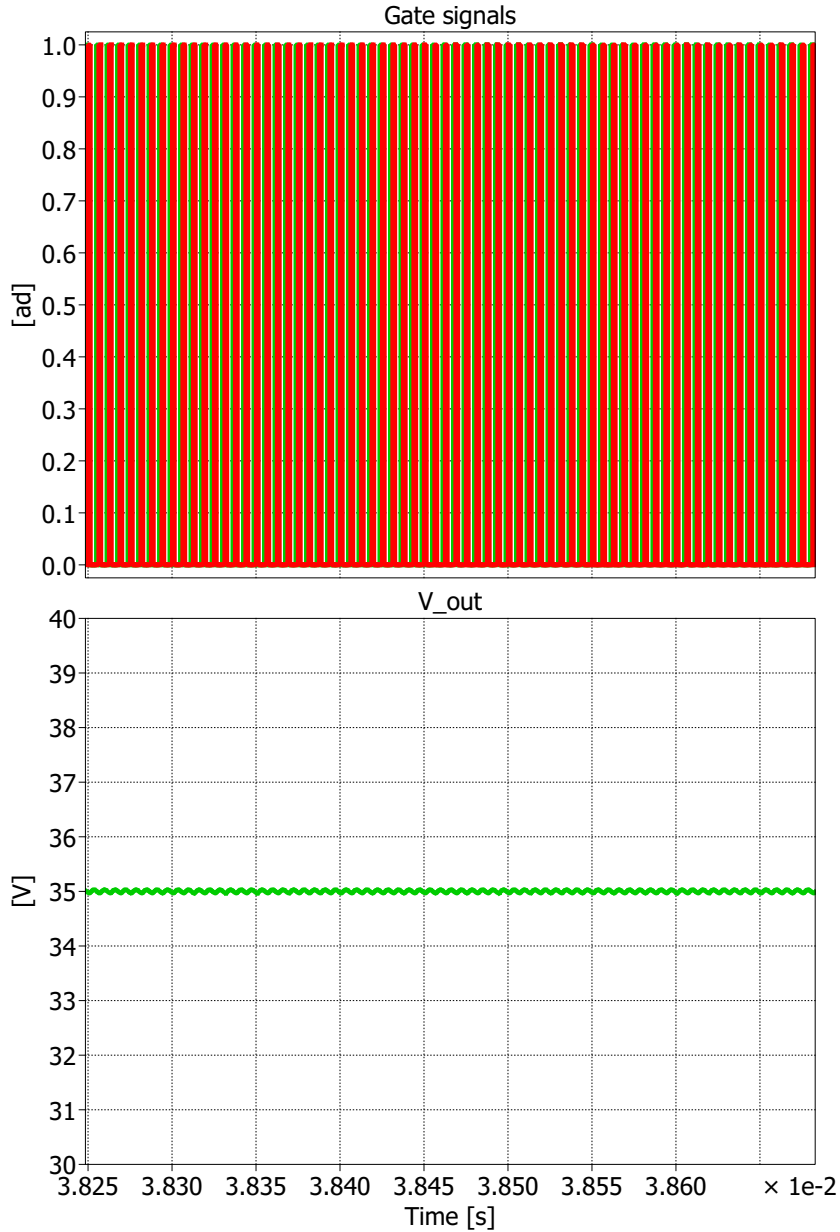

FIGURE 2.24: Output voltage ripple in PWM modulation. Working point $7A_{out}$ - $35V_{out}$ $f_{sw} = 160\text{kHz}$ $duty = 0.23$
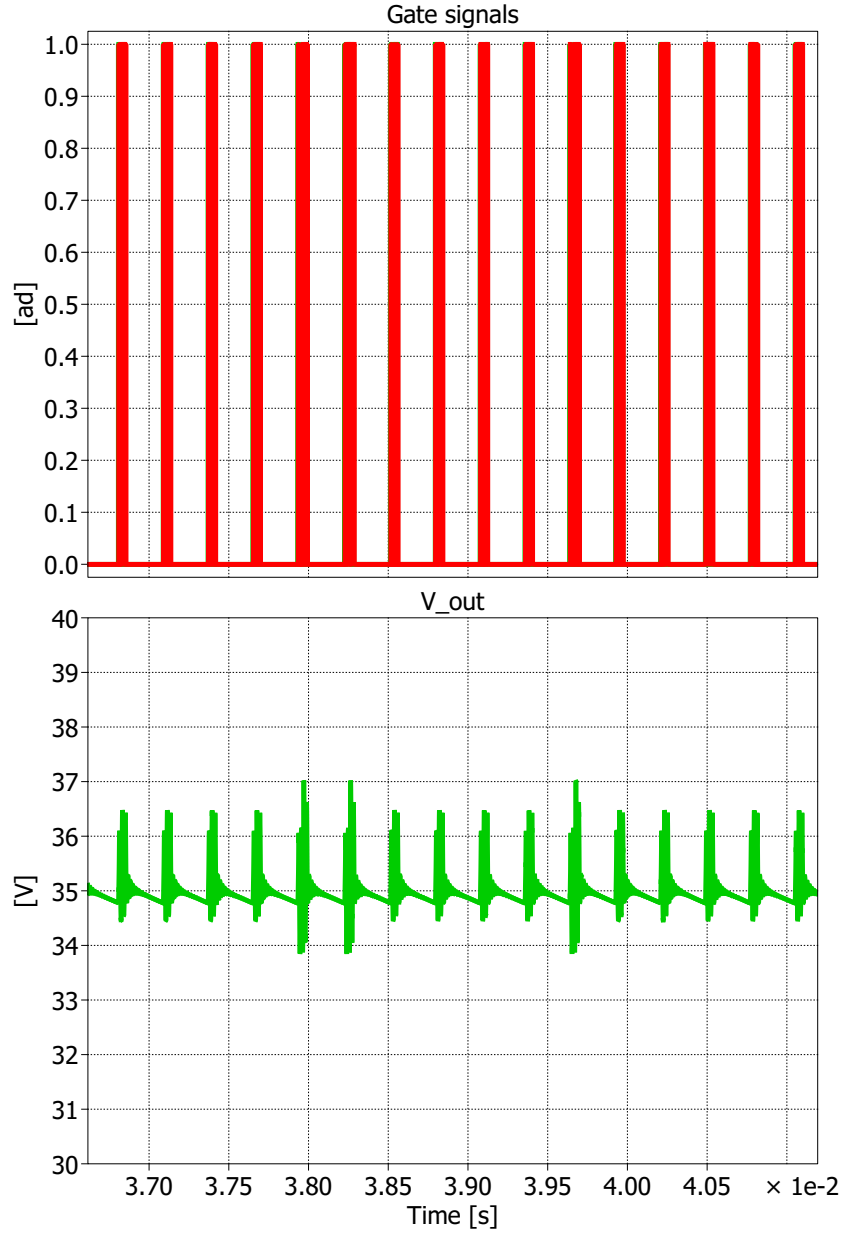
FIGURE 2.25: Output voltage ripple in burst control. Working point
7A$_{out}$ - 35V$_{out}$ $f_{sw} = 160$kHz

2.5.1   Considerations on losses

The enhanced PWM adoption benefits the output regulation in terms of reduced voltage ripple with respect to the burst mode. Another interesting aspect concerns the amount of switching and conduction losses, but the comparison is not easily achieved. These differences characterize the two type of modulation:

- In burst modulation, only the first commutation of the pulse train is in hard-switching condition, while in PWM modulation a hard-switching event happens every switching cycle on the device that starts the modulation.

- In PWM modulation, the conduction losses are related to the duty cycle value, while in burst mode the duty cycle is always 50% and duration of the pulse train is determined by the burst period T_{burst}.

On the basis of these considerations a detailed analysis will be the subject of future work. The following sections will be focused on the minimization of the switching losses in PWM operation.

2.6 PWM stop time equivalent circuit

As stated in the section 2.4 during PWM operation more power is allocated on the device that begins the modulation. In the following sections, a technique is proposed to mitigate the turn-on losses by the analysis of the free oscillation during PWM stop time and adapting on it the gate signals generated by the LLC controller.
The equivalent capacitance at the midpoint C_{MP} of the half-bridge poses a restraint on the minimum and maximum dead time in case of PFM operation. When PWM operation is employed at light load, due to the duty cycle lower than $0,5$, the t_{off} duration is much larger than the maximum allowable dead time. Hence is useful to investigate the HB behaviour, with the help of the equivalent circuit shown in Fig. 2.26, where R_S is the sum of all stray resistances of: copper traces, primary transformer winding and ESR of C_r capacitor.
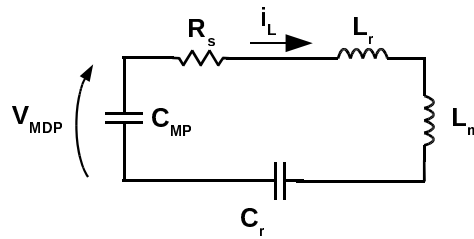

FIGURE 2.26: Equivalent circuit used to investigate free oscillation during light load operation in case of PWM modulation.

In the circuit is omitted the resistance modelling the output load (that should be placed in parallel to the magnetic inductance) because at light load condition it can be neglected. It affects the damping factor of the free oscillation, while the period is mainly affected by the C_{MP}. Figure 2.27 shows the change of the free oscillation, changing the C_{MP} value from 100pF to 1000pF and maintaining a fixed output load of 100Ω. Figure 2.28 refers to the case where the output load is changed from 1Ω to 100Ω with a fixed value of C_{MP} equal to 100pF. These simulations were obtained in open loop with the resonant tank parameters listed in Tab. 2.2 and the working condition indicated by Tab. 2.9 and Tab. 2.10.

An interesting research topic, that will be object of future work, is the investigation of the effects of resonant tank parameters together with the parasitics on the free oscillation during the stop time t_{off} at different output loads. The evolution of the current and voltage waves during the stop time does not occur if PFM modulation is used, but with PWM modulation the analysis of them gains interest. While this work does not deal with this topic, it may investigate the design of the resonant tank taking into account the free oscillation, finding the dependency of the damping factor with the duty cycle, switching frequency and the output load.

C_{MP}	V_{out}	P_{out}	f_{sw}	R_{out}	duty cycle
100pF					
500pF	40V	16W	50kHz	100Ω	15%
1000pF					

TABLE 2.9: Working points for different C_{MP} values at fixed output
load.

An external capacitor of a specific value could be added to manage the free os-
cillation or an enhanced PWM control with a variable switching frequency linked to
the duty cycle value could be realized. In the following, the case of study will con-
cern the light load condition and the midpoint stray capacitance will be considered
to be determined by the characteristics of MOSFETs adopted for the half-bridge and
by parasitics. After the analysis of the free oscillation effects over the half-bridge op-
eration, a control for mitigating the hard-switching commutations will be presented.
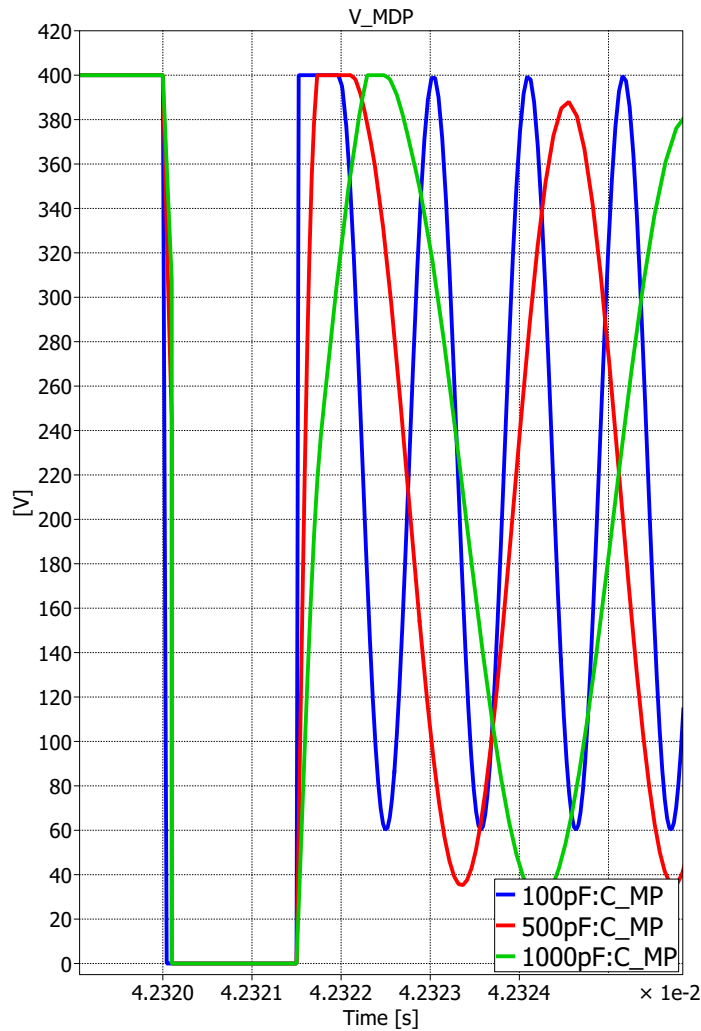
FIGURE 2.27: Free oscillation amplitude at different values of C_{MP}.
Working conditions indicated by Tab. 2.9.
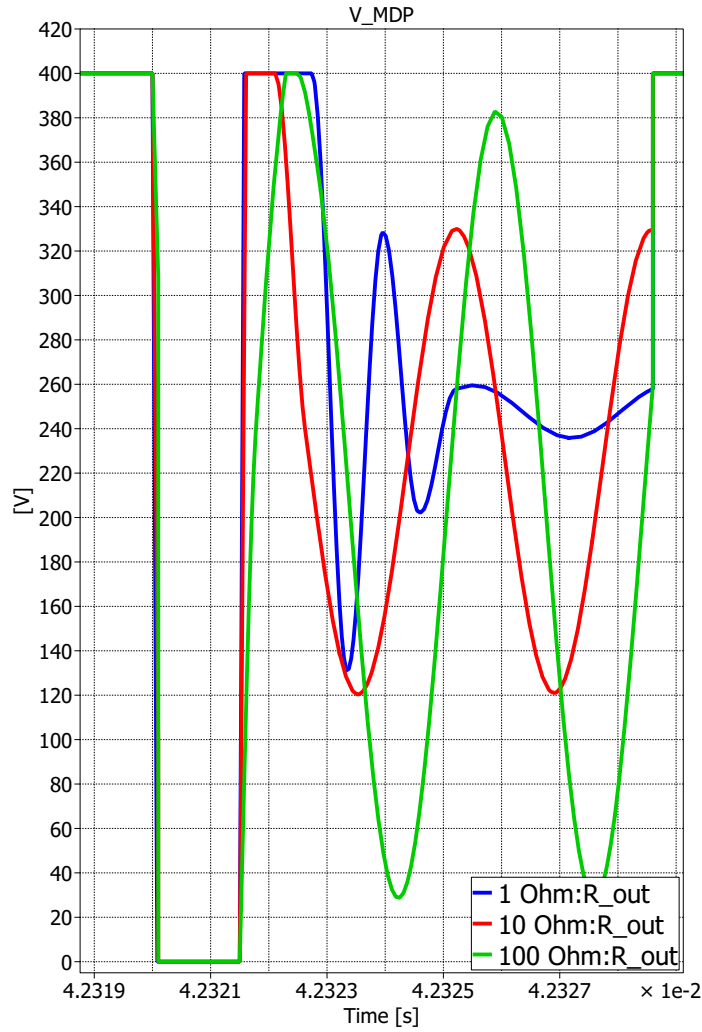
FIGURE 2.28: Free oscillation amplitude at different values of R_{out}. Working conditions indicated by Tab. 2.10.

R_{out}	V_{out}	P_{out}	f_{sw}	C_{MP}	duty cycle
10Ω	5V	16W			
100Ω	15V	46W	50kHz	1000pF	15%
1000Ω	40V	16W			

TABLE 2.10: Working points for different R_{out} values at fixed output load.

2.7 Free oscillation during PWM stop time

The free oscillation frequency of the current i_L (and of course of the midpoint voltage V_{MDP}), when both switches ant their body diodes are turned off, is [14]:

$$f_{fo} = \frac{1}{2\pi\sqrt{\frac{(L_m + L_r)C_{MP}C_R}{C_{MP} + C_R}}} \tag{2.30}$$

Figure 2.29 gives a representation of a free oscillation in PWM modulation. Since the free oscillation frequency is dominated by the C_{MP} term (usually much lower than C_r in case of low power applications), its value is usually one (or more) order of magnitude higher than the resonant frequency of the LLC converter. In the case of high-power, high-efficiency designs, low R_{dson} Si devices are characterized by large values of C_{DS}. This can shift the free oscillation frequency closer to f_{MAX} of the LLC converter, resulting in a longer settling time of the free oscillation.
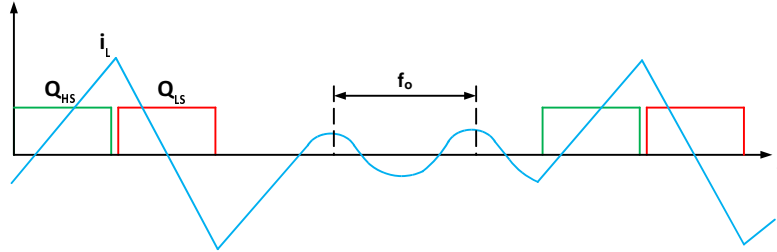
FIGURE 2.29: Free oscillation waveform during PWM modulation.

Typically, after one period of free oscillation, neither upper or lower diode of HB enter conduction. Since in High-Power LLC the designed damping factor of the resonant circuit of Fig. 2.26 is extremely low to minimize power losses, the resulting free oscillation does not subsides before the end of t_{off}. As a result, the following cycle switch commutation can take place with the switching-on device drain-source voltage V_{DS} ranging from a few Volts (almost ZVS commutation) up to V_{DC} (complete hard-commutation). In hybrid PWM controllers typically the entering in PWM mode happens with the maximum frequency of the PFM, f_{MAX}. In order to minimize the switching voltage, the value of f_{MAX} and the duty cycle range should be chosen in a proper way, since with Si devices the value of f_{fo} can be only slightly modified with a proper choice of power transistors (C_{DS}) and PCB design (C_s). Adopting SiC devices a good benefit can be obtained on the free oscillation frequency because the C_{DS} of a SiC device is lower than that of Si device. The other components of the equivalent circuit (see Fig. 2.26) are the result of the design procedure of the resonant tank. A design verification step requires that the working point in PWM modulation is admissible in terms of hard-switching commutation and dissipation for the devices. Figure 2.11 plots the static gain at nominal output power. As can be seen, the working point is near to resonant in both case (blue and green lines) and ZVS condition is guaranteed. Figure 2.30 shows the working point in light load operation (200W). The switching frequency of working point at the minimum output is 5 times the resonant frequency. In this case, the advanced PWM modulation is adopted and hard-switching commutation on the high side device happens every switching cycle when the load is regulated at low voltage. For a wide variation of PWM duty cycle, the turn-on commutation is almost random with respect of free oscillation waveforms, resulting in increased losses at light load. Moreover, the losses are almost all allocated to the first device starting the PWM sequence: in this example Q_{HS}.

A reduced switching voltage of this commutation could happen with the use of an adaptive t_{off} related to free oscillation. In low power LLC converters typically the free oscillation subsides before the end of t_{off} resulting in a first commutation with $V_{DS} = \frac{V_{DC}}{2}$. This can be considered a soft-switching condition with respect the case of free oscillation does not subside and the commutation may start at the peak of drain-source voltage.
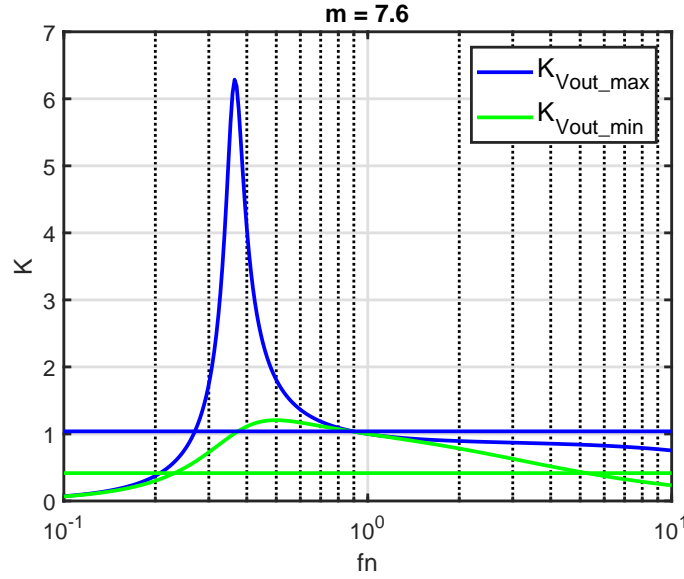
FIGURE 2.30: K curves at light load (200W) with respect to the normalized switching frequency.

A possible solution to this unwanted behaviour is the introduction of adaptive PWM techniques, where the controller waits for one of the valleys in Q_{HS} drain voltage to switch on. Adaptivity can be reached by discretely adjusting the duty cycle or by varying the PWM frequency. Another possible solution is to evenly distribute the losses among the HB devices by alternating the device starting the PWM commutation: i.e. the last device turned off is the first one to be turned on in the following cycle. Since PWM operation occurs at f_{MAX}, the risk of transformer saturation is avoided.

(a)   (b)   (c)
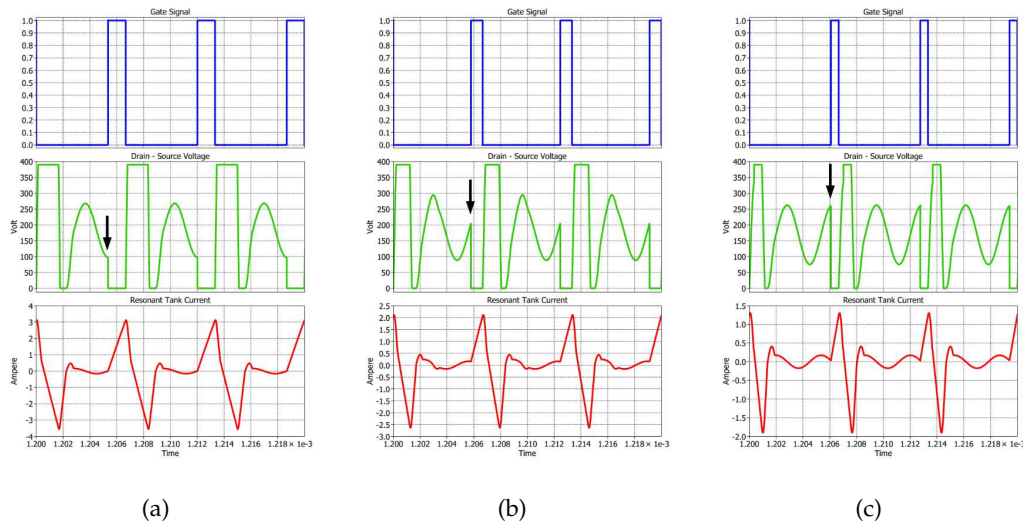
FIGURE 2.31: Commutation of Q_{HS} at different point of free oscillation: valley of free oscillation (a); mid free oscillation (b); peak of free oscillation (c).

2.8   Adaptive PWM

This section describes the proposed adaptive PWM control and its implementation in a simulation model. In order to appreciate the benefits introduced by adaptive PWM, it is useful to start by analyzing the influence of the under-damped free oscillation on turn-on losses of Q_{HS} during light load PWM operation. This is investigated via numerical simulations in PLECS environment: the simulation parameters are the same listed in Table 2.1 considering a maximum switching frequency of 150kHz during PWM operation. The comparison was first carried out at light load condition, in PWM modulation with a 20% duty cycle value. Three values were identified for the commutation: at the valley, at the peak and at the midpoint of the V_{DS} free oscillation, as shown in Figs. 2.31(a)-2.31(c).

Switching Condition	STW56N65M2	STW57N65M5	SCT3080AL
Valley	1,0 µJ / 153,60 mW	0,62 µJ / 93,12 mW	0,32 µJ / 48,0 mW
Mid	6,40 µJ / 960,0 mW	3,88 µJ / 582,0 mW	2,0 µJ / 300,0 mW
Peak	10,80 µJ / 1622,40 mW	6,60 µJ / 983,6 mW	3,38 µJ / 507,0 mW

TABLE 2.11: Turn-on losses comparison at 150kHz

Table 2.11 summarizes the turn-on losses under different conditions identified previously. Three simulation sets were performed with different power semiconductor devices: STW56N65M2 optimized for soft-switching operation and Si MOSFET STW57N65M5 and SiC MOSFET SCT3080AL optimized for hard-switching operation. As it can be seen, by implementing a suitable adaptive PWM strategy it is possible to greatly reduce the turn-on losses during light load operation.
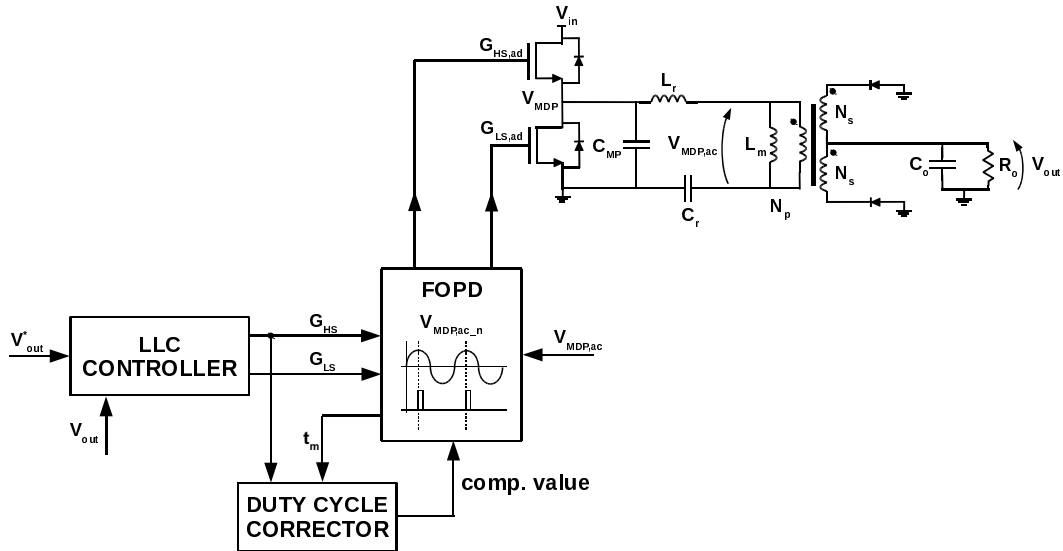

FIGURE 2.32: Adaptive PWM control scheme represented with functional blocks: LLC Controller generating the PWM signals, FOPD block that masks the PWM signal until the ZVS condition is detected and Duty Cycle Corrector block for Q_{LS} duty compensation.

The proposed adaptive PWM control implementation is summarized by the control scheme in Fig. 2.32. The working principle is based on Quasi-Resonant operation: the midpoint voltage $V_{MDP,ac}$ is provided to the Free Oscillation Peak Detector (FOPD) circuit. The measure of $V_{MDP,ac}$ is taken after the resonant capacitor to bypass half-bridge DC offset. The function of this block is to allow the Q_{HS} turn-on only on a minimum value of V_{DS}, which corresponds to a peak of V_{MDP} during free oscillation phase. When the output of PWM generator of the LLC controller is high (as to restart modulation after a free oscillation phase), the gate signals are masked by FOPD until a peak is detected. The next section 2.9 gives a detailed description of the FOPD working principle.

Due to the damping of free oscillation, a better ZVS condition can be achieved during the first few cycles. In fact the V_{MDP} transient tends to run out to $\frac{V_{DC}}{2}$ value. As shown in Fig. 2.34 the adaptive PWM reduces the effective duty cycle applied to Q_{HS} device. Without compensation, adaptive PWM would result in an offset in the modulation (i.e. Q_{HS} on-time is lower than Q_{LS} on-time).
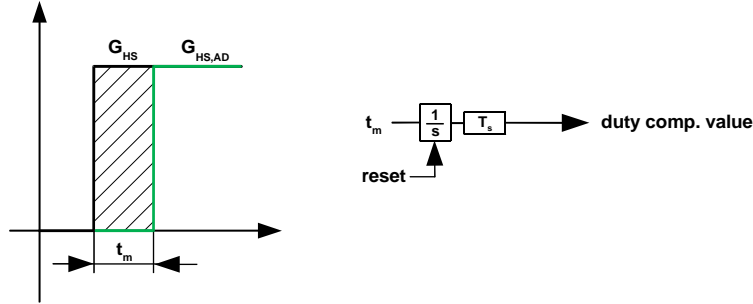
FIGURE 2.33: Duty Cycle Corrector: the duty cycle of the low side device is computed by the value obtained from the masking time t_m.

The Duty Cycle Corrector (DCC) block introduces a compensation to the reference used by the PWM generator responsible for Q_{LS} duty cycle. The schematic circuit of Fig. 2.33 shows the working principle, the simulation parameters are the same of Tab. 2.2 with PWM switching frequency equal to 150kHz and with $C_{MP} = 1$nF. The interval of masked time t_m among the original and the adapted gate signal of Q_{HS} device is integrated and rescaled proportionally to the switching period. Then the computed value is subtracted to the reference used for the Q_{LS} gate signal generation. As a result, the falling edge of the Q_{LS} gate signal is properly anticipated and the symmetry between the two gate signals is maintained. The integrator is reset on the rising edge of the Q_{HS} gate signal. In Fig. 2.35 the Q_{LS} gate signal is compensated by the duty corrector according to the masking time and the t_{on} periods are the same for both devices.
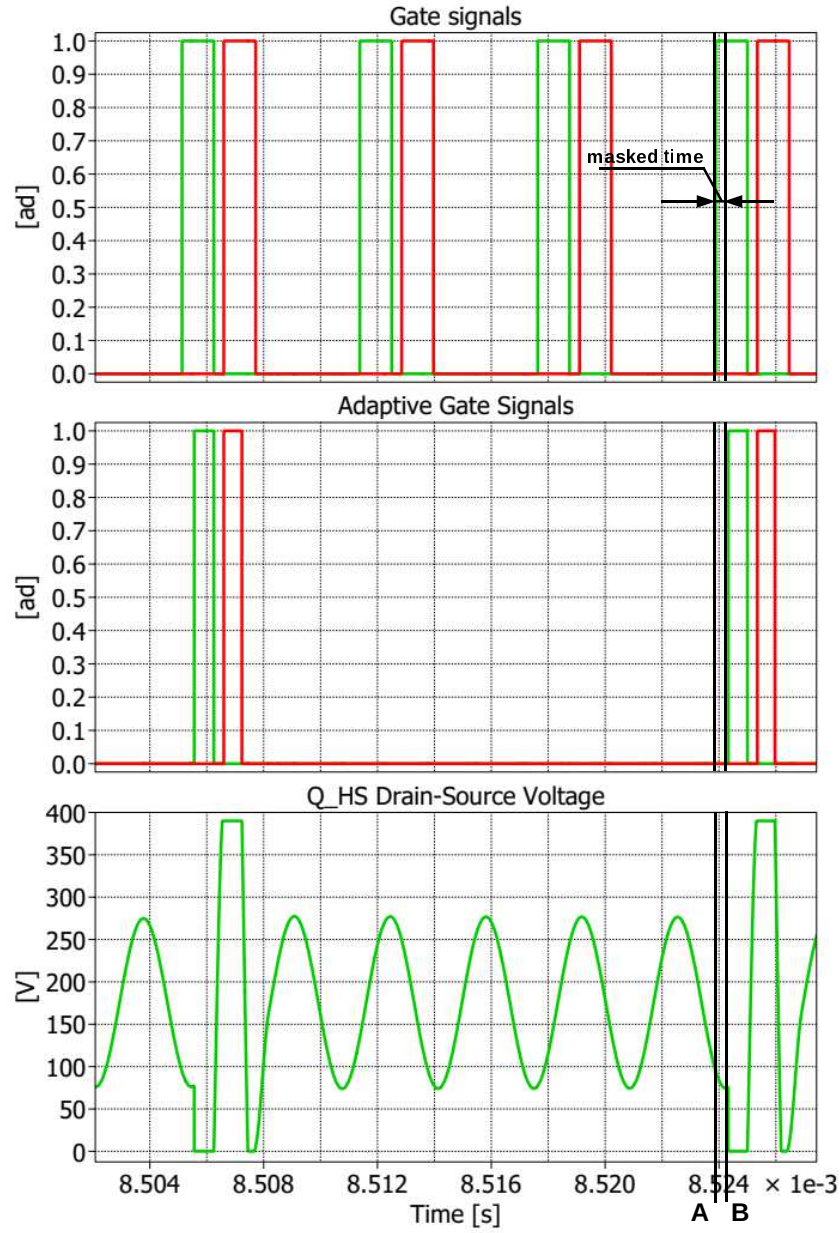
FIGURE 2.34: Adaptive commutation in PWM mode at 150kHz and with $C_{MP} = 1$nF. First plot: G_{HS} -green- and G_{LS} -red-. Second plot: Adapted $G_{HS,ad}$ -green- and $G_{LS,ad}$ -red. Third plot: Drain-source voltage of Q_{HS}. The cursors A and B define the masking time.
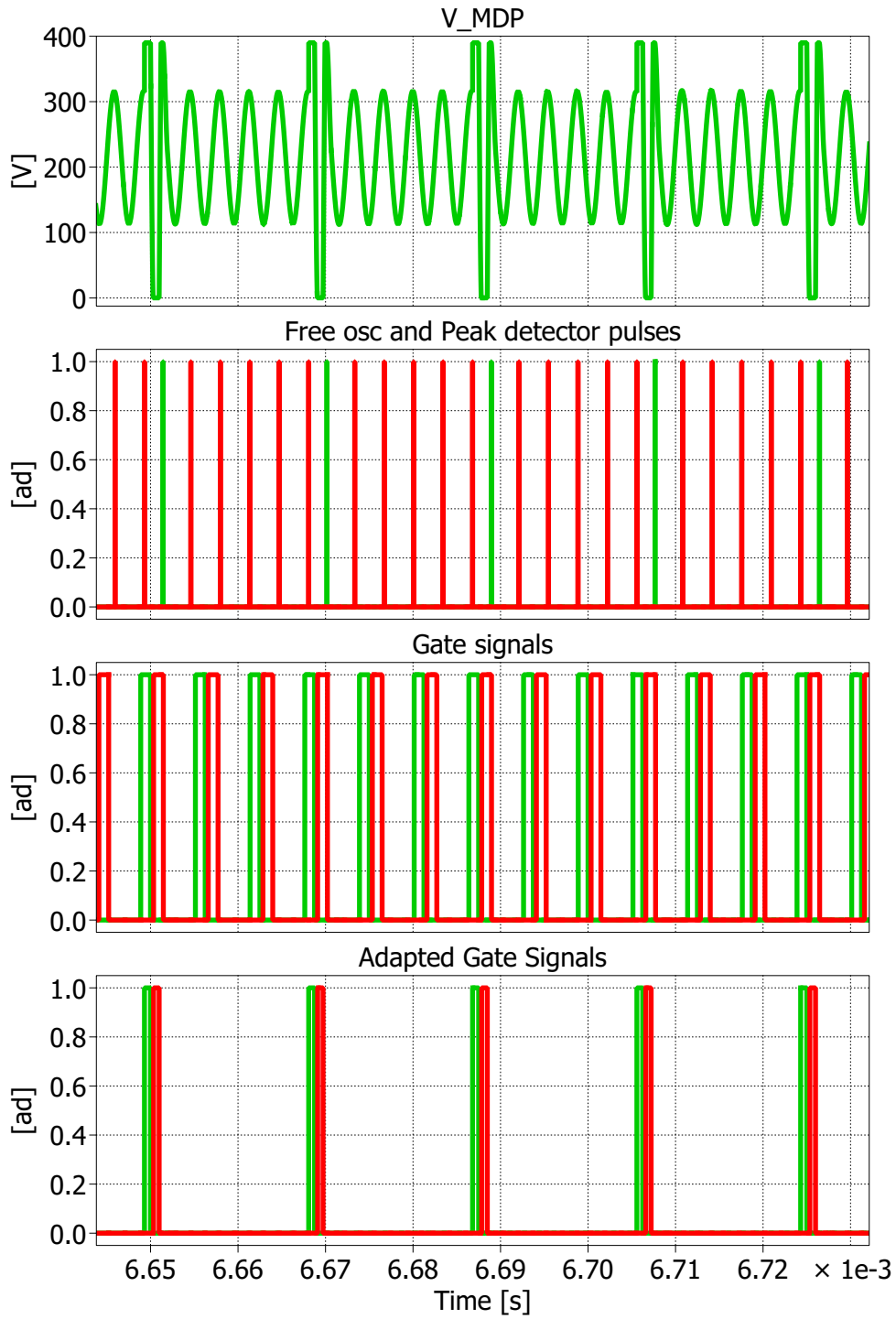
FIGURE 2.35: Adapted gate signals by duty corrector (PWM mode at 150kHz and C_{MP} = 1nF). First plot: midpoint voltage V_{MDP}. Second plot: Free Oscillation Detector pulse -green- Peak Detector Pulse - red-. Third plot: G_{HS} gate signal - green- and G_{LS} gate signal - red-. Fourth plot: $G_{HS,ad}$ gate signal - green; $G_{LS,ad}$ gate signal - red

2.9 Free Oscillation Peak Detector circuit and Peak Detector design

This section describes the FOPD illustrated in Fig. 2.36. In the figure are shown three function blocks: the *Free Oscillation Detector*, the *PWM Masking* and the *Peak Detector*. The first two blocks can be realized by combinational logic circuits and is not interest of this section their practical implementation. The proposed Peak Detector differs from the traditional circuit [15, 16, 17]. The intended circuit identifies the peak of the input signal generating a pulse every occurrence, while the main function of traditional peak detectors is to detect the peak value of an input signal and track the peak over time.

At the input are given the $V_{MDP,ac}$, the PWM signals generated by the LLC controller and the compensation value of the duty cycle computed by the DCC. The PWM signals state is used to detect when the PWM cycle is completed and the free oscillation starts. As shown in Fig. 2.37, a pulse is generated by Free Oscillation Detector block when both gate signals are low for a time greater than the dead time t_d. This trig disables PWM signals G_{HS} and G_{LS} and enables the Peak Detector pulse generation.
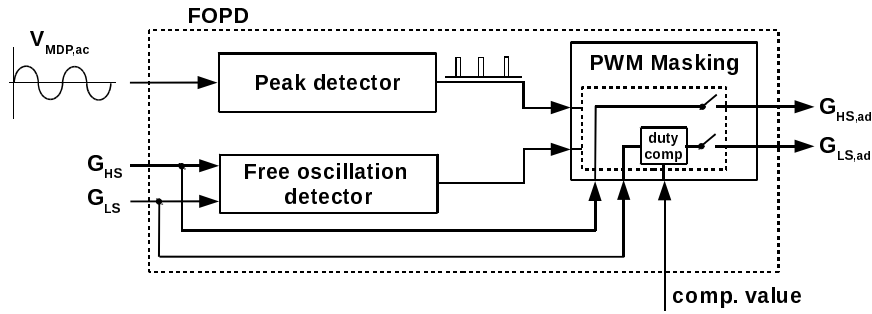
FIGURE 2.36: Free oscillation peak detector circuit (FOPD).

The PWM modulation is renabled when peak detector pulse is received on the high state of G_{HS}. The PWM cycle is skipped if the correspondence between the high state of G_{HS} and peak detector pulse is lost. When the peak detector pulse happens during the high state of G_{HS} signal, the adapted PWM gate signals $G_{HS,ad}$ and $G_{LS,ad}$ are generated. The compensation value computed by the duty corrector is used to compensate the value of the duty cycle for the low side gate signal. The function logic of FOPD is summarized by the flow chart of Fig. 2.38 and an example of operation is reported in Fig. 2.35.
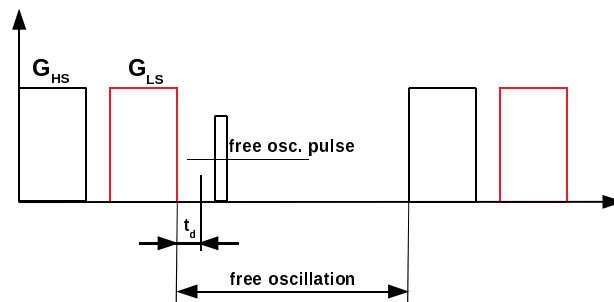

FIGURE 2.37: Pulse generated by Free Oscillator detector during the free oscillation time.
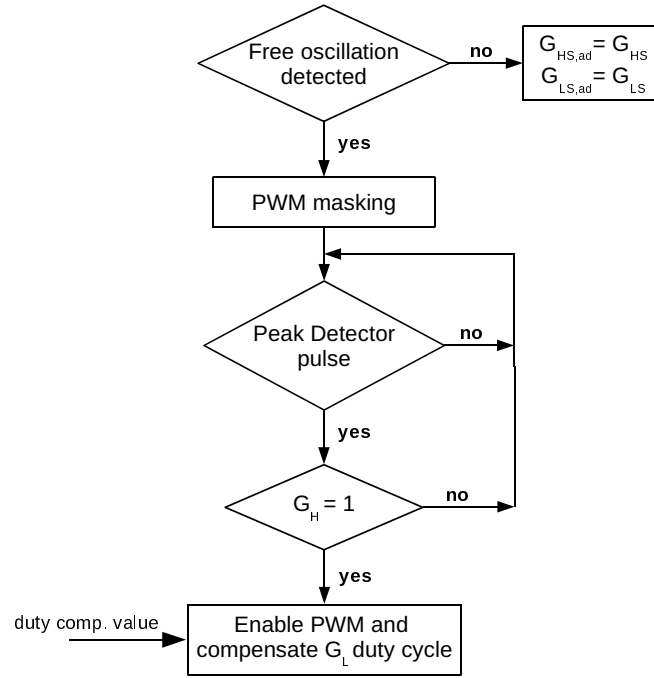
FIGURE 2.38: Flow chart of the FOPD.

2.9.1 Design of the Peak Detector

This section deals the design of the peak detector circuit of Fig. 2.39 for a practical implementation. The midpoint voltage $V_{MDP,ac}$ given at the input of the FOPD block is measured by means of an auxiliary winding and rescaled by the turn ratio to V_{MDP,ac_n}. The respective DC signal is obtained adding V_{offset} through a *non-inverting Level Shifter*. Then the $V_{MDP,dc}$ signal is compared with its delayed form $V_{MDP,phs}$ generated by the *All-pass Filter*. The square wave obtained at the output of the *Square wave generator* has the rising edge in correspondence of $V_{MDP,dc}$ peak (that corresponds to a valley of the drain-source voltage of the high side device). A pulse of amplitude t_p is generated by the final *Rising Edge Detector* stage, making the logic AND operation between the original square wave and the inverted square wave delayed of t_p by the inverter.
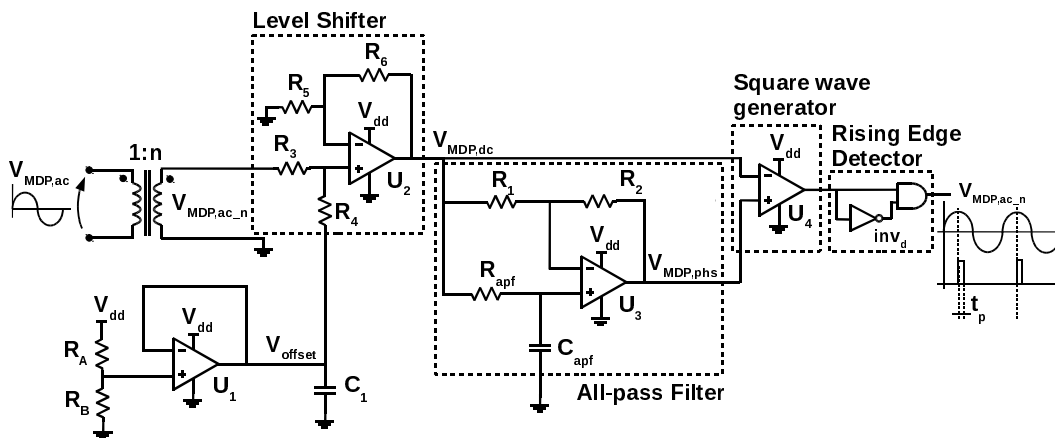

FIGURE 2.39: Peak detector circuit.

The turns ratio of the galvanic transformer set the amplitude of V_{MDP,ac_n} to match the full scale V_{fs} of the logic circuits supplied at V_{dd}. The voltage divider R_A, R_B generates the offset voltage V_{offset}, equal to half V_{fs}:

$$V_{offset} = \frac{V_{fs}}{2} = V_{dd} \frac{R_B}{R_A + R_B} \tag{2.31}$$

The values of the voltage divider come out by choosing:

$$V_{dd} = 5V$$

$$V_{fs} = 3V$$

$$R_A = 10k\Omega$$

$$R_B = \frac{R_A V_{offset}}{\left(V_{DD} - V_{offset}\right)} = \frac{10000 \cdot 1,5}{5 - 1,5} = 4220\Omega \tag{2.32}$$

The op-amp U_2 is configured as non-inverting level shifter for adding to V_{MDP,ac_n} the offset voltage V_{offset} generated by U_1 :

$$V_{MDP,dc_n} = A_{out} \cdot V_{MDP,ac_n} + A_{offset} \cdot V_{offset} \tag{2.33}$$

The gains applied to the output A_{out} and the gain of the offset voltage A_{offset} are equal to:

$$A_{out} = \frac{R_4}{R_5} \cdot \frac{(R_5 + R_6)}{(R_3 + R_4)}$$
$$A_{offset} = \frac{(R_5 + R_6)}{R_5} \cdot \frac{R_3}{(R_3 + R_4)} \tag{2.34}$$

If $R_5 = R_3$ and $R_6 = R_4$, the gains become:

$$A_{out} = \frac{R_4}{R_5}$$
$$A_{offset} = \frac{R_3}{R_5} \tag{2.35}$$

The resistors R_3, R_4, R_5 and R_6 are all set equal to 10kΩ, for obtaining the gains equal to one in the sum of the eq. 2.33.
A square wave having the rising edge aligned with the peak of $V_{MDP,dc}$ is generated by the comparator U_4. The signal is compared with its phase shifted form $V_{MDP,phs}$. The phase shifted signal is generated by the All-pass Filter realized with the op-amp U_3. The resistances R_1 and R_2 are of the same value of 1kΩ and R_{apf} and C_{apf} are used to set the phase shift of the delayed output signal $V_{MDP,phs}$. The transfer function of the All-pass Filter is given by:

$$H(s) = \frac{V_{MDP,phs}}{V_{MDP,dc}} = \frac{-1 + \tau s}{1 + \tau s} \tag{2.36}$$

where the time constant is equal to:

$$\tau = R_{apf} C_{apf} \tag{2.37}$$

The phase of $H(s)$ is the argument of $H(s)$:

$$
\begin{aligned}
\varphi = \angle H(s) = \\
= \tan^{-1} \frac{\Im\{\text{num}[H(s)]\}}{\Re\{\text{num}[H(s)]\}} - \tan^{-1} \frac{\Im\{\text{den}[H(s)]\}}{\Re\{\text{den}[H(s)]\}} = \\
= \tan^{-1} \left(\frac{\omega\tau}{-1} \right) - \tan^{-1} \left(\frac{\omega\tau}{1} \right) = \\
= -2\tan^{-1}(\omega\tau)
\end{aligned}
\tag{2.38}
$$

Setting the value of R_{apf} equal to 1Ω the value of the capacitance is obtained rearranging the eq. 2.38, where f_{apf} is the frequency at which the shift φ is desired:

$$
C_{apf} = \frac{1}{R_{apf}} \cdot \frac{\tan\left(-\frac{\varphi}{2}\right)}{2\pi f_{apf}}
\tag{2.39}
$$

The voltage difference at the inputs of the comparator U_4 is generated by phase shift φ, that should be as small as possible in order to obtain the final output pulse synchronized with the peak of the input wave. However, the phase shift has to be sufficient to generate a voltage difference that matches the minimum identifiable threshold by the comparator.

The free oscillation frequency is computed from the eq. 2.30, where the C_{MP} value comes from the eq. 2.27. A value of 1nF is chosen accordingly to STW56N65M2 MOSFET part number and PCB layout. From these considerations is obtained:

$$
\begin{aligned}
f_{fo} = \frac{1}{2\pi\sqrt{\frac{(L_m + L_r)C_{MP}C_R}{C_{MP} + C_R}}} = \\
= \frac{1}{2\pi\sqrt{\frac{(250\times10^{-6} + 38\times10^{-6})1\times10^{-9}\cdot324\times10^{-9}}{1\times10^{-9} + 324\times10^{-9}}}} = \\
= 297\text{kHz}
\end{aligned}
\tag{2.40}
$$

The value of the capacitance C_{apf} is defined accordingly to the value of the desired phase shift φ between the signals $V_{MDP,dc}$ and $V_{MDP,phs}$. The phase shift is defined in terms of time delay t_φ between the two signals:

$$
\begin{aligned}
t_\varphi = 100\text{ns} \\
\varphi = 2\pi f_{apf} \cdot t_\varphi = 2\pi \cdot 297 \times 10^3 \cdot 100 \times 10^{-9} = 0,18\text{rad}
\end{aligned}
\tag{2.41}
$$

The resulting capacitance C_{apf} value is equal to:

$$
C_{apf} = \frac{\tan\left(-\frac{0,18}{2}\right)}{2\pi \cdot 297 \times 10^3} = 1\text{nF}
\tag{2.42}
$$

The final output pulse is produced identifying the rising edge of the square wave generated by the comparator U_4 of the Square Wave Generator.
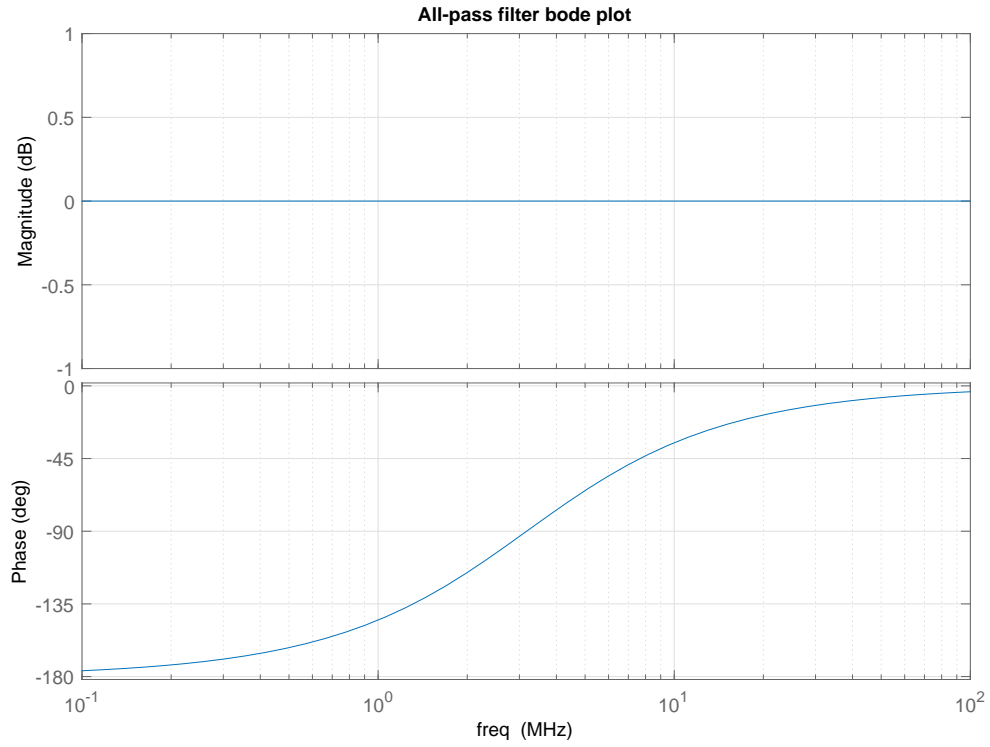
FIGURE 2.40: Bode plot of the designed All-pass Filter: $10,7°$ ($t_{apf} = 2ns$ @ 297kHz.

The plot of Fig. 2.40 shows the Bode plot of the resulting All-pass Filter, that match at f_{apf} the designed phase shift. Figure 2.41 shows the simulation of the circuit with LTspice software. All component are considered ideals and the pulse coincides with the peak of $V_{MDP,dc}$.
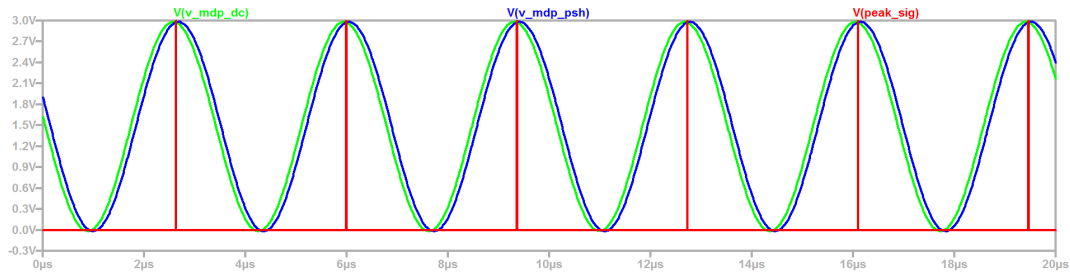
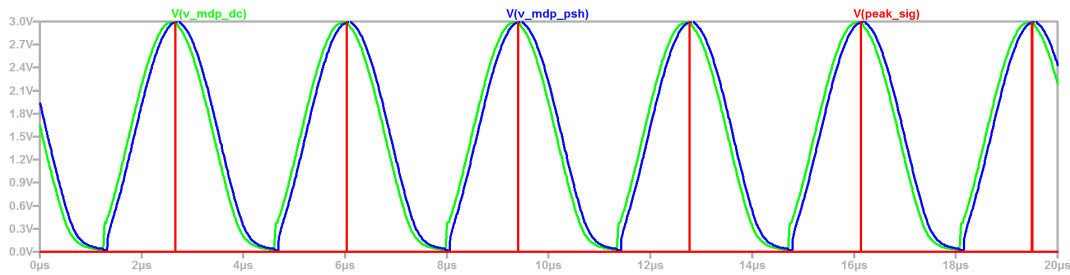

FIGURE 2.41: Peak detector LTSpice simulation with ideal devices. $V_{MDP,dc}$ -green-; $V_{MDP,phs}$ -blue-; peak detector pulse -red-.

The not idealities affecting the synchronism between the peak of $V_{MDP,dc}$ and the pulse signal are:

- The gain bandwidth product of the operational amplifier that describes the flatness of the gain with respect the frequency.

- The speed of the comparator and the value of the threshold that defines the minimum identifiable voltage difference at the inputs.

- The signal propagation delays from the input to the output of each circuit.

Due to these limits, the phase shifted signal results to be attenuated at high frequency. A minimum phase shift is required to make identifiable the difference between the two signals at the inputs of the comparator. Further, an additional propagation delay is added to the delay generated by the phase shifting. Simulation of Fig. 2.43 shows the waveform of the model in Fig. 2.42 with not ideal devices. The simulation implements AD8091 as high speed op-amp and high-speed-low propagation delay comparator LTC6752. Due to the no-idealities the signals are distorted and the pulse generated by the peak detector does not match perfectly the peak of $V_{MDP,dc}$ signal.
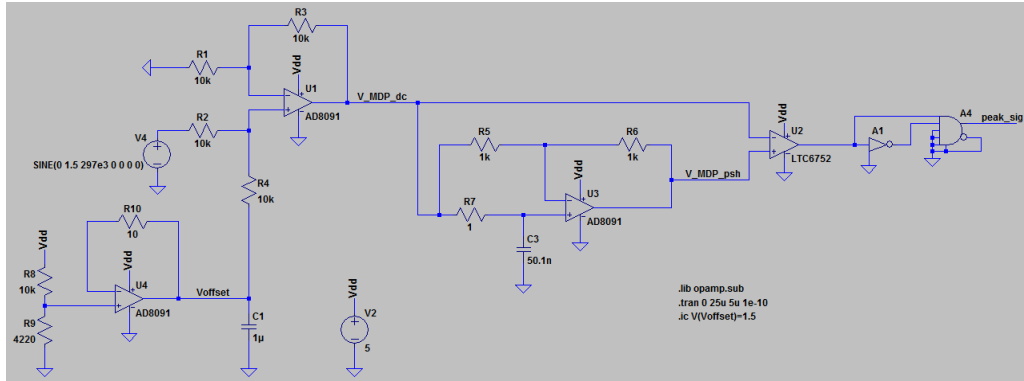
FIGURE 2.42: Peak detector modelled on LTSpice with not ideal devices.

FIGURE 2.43: Peak detector LTSpice simulation with real devices. $V_{MDP,dc}$ -green-; $V_{MDP,phs}$ -blue-; peak detector pulse -red-.

2.10 Experimental results

This section deals with the analysis and the experimental evaluation of a prototype LLC converter (Fig. 2.44). The converter was built with the characteristics described in section 2.2. The LLC control is performed by the FAN7688 controller that implements a hybrid modulation strategy:

- PFM modulation for nominal condition up to light load.

- PWM 2 for light load condition down to duty cycle $D = 0,12$ without adaptive turn-on.

FIGURE 2.44: LLC prototype under test.

An evaluation concerning the effect of the stray capacitance of the Si and SiC devices on the free oscillation will be illustrated. The MOSFET used for the half-bridge is STW56N65M2 as Si device and SCT3080AL as SiC device. Thermal imaging is obtained via a SEEK Reveal PRO thermal camera. The prototype is connected to a variable DC voltage source. A DC electronic load EA-ELR 9080-170 is used to vary the output current of the LLC converter between $1A$ (light load PWM operation) and $50A$ (rated load PFM operation). Efficiency tests were carried out using N4L PPA5530 (3-phase 50A version) power analyzer.
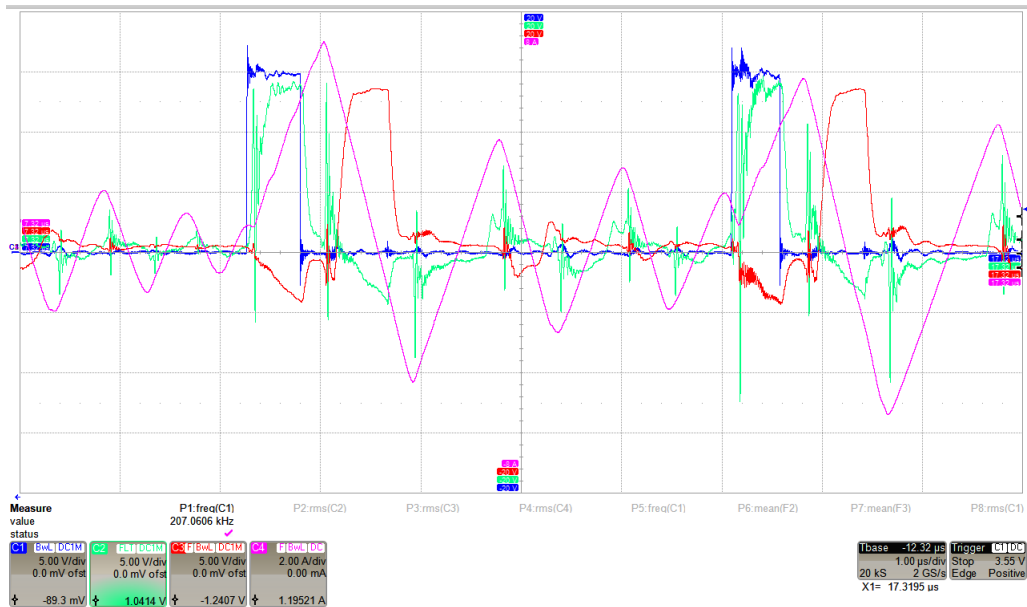
FIGURE 2.45: Oscilloscope capture of free oscillation during PWM t_{off} with Si-MOSFETs STW56N65M2. Turn-on commutation not synchronous with free oscillation. HS gate drive input - blue; Q_{HS} V_{GS} - green; Q_{LS} V_{GS} - red; resonant tank current - purple.
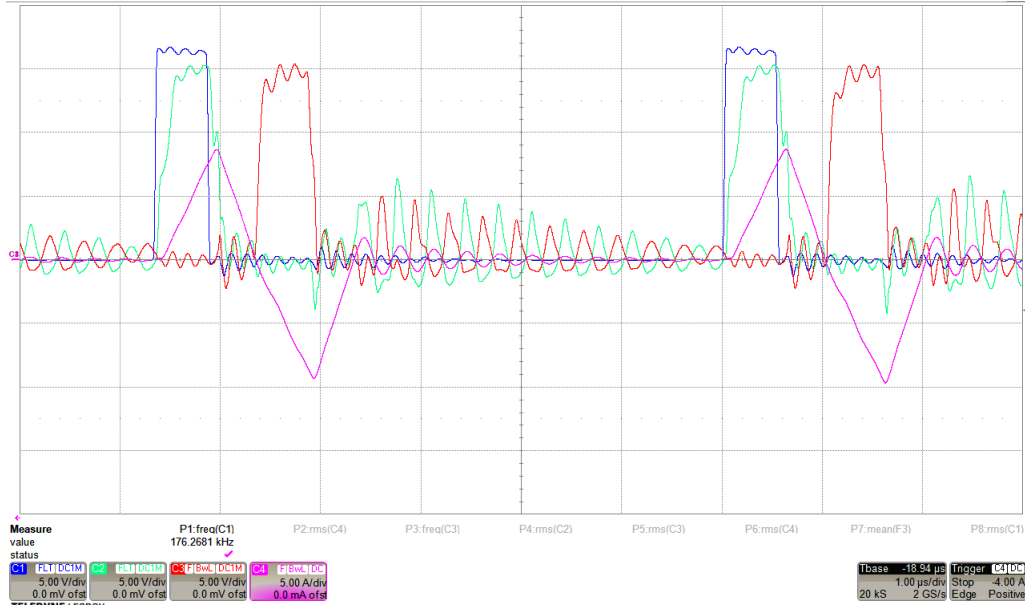
FIGURE 2.46: Oscilloscope capture of free oscillation during PWM t_{off} with SiC-MOSFETs SCT3080AL. Free oscillation decays before gate signal turn-on. HS gate drive input - blue; Q_{HS} V_{GS} - green; Q_{LS} V_{GS} - red; resonant tank current - purple.
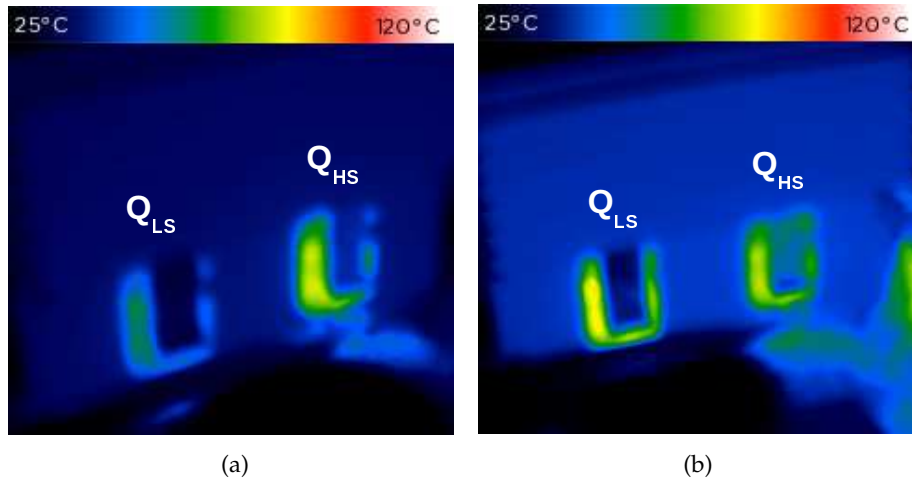

FIGURE 2.47: a): Increased power losses during PWM light load operation with STW56N65M2. Q_{HS} temperature $78°C$. b): Equally distributed losses during PFM nominal load operation with STW56N65M2. Q_{HS}, Q_{LS} temperature $75°C$.

The free oscillation shown in Fig. 2.45 is acquired during a PWM modulation at light load. A hard-switching event of the high side device occurs when the current of free oscillation in not completely ended. This results from an equivalent midpoint capacitance that is dominated by the output capacitance value of the devices. Figure 2.46 shows the same operating condition with SiC devices: because of the lower C_{ds}, the resulting free oscillation frequency is higher and decays faster compared with the silicon counterpart, reducing the likelihood of a full voltage hard-switching turn-on. Comparing Fig. 2.47(a) against Fig. 2.47(b) (obtained at thermal regime) it is possible to observe the increased power losses associated with PWM operation. The

first hard-switching commutation of the PWM mode induces higher dissipations on the high side device Q_{HS} with respect the low side one Q_{LS}.

Figure 2.48 shows the oscilloscope acquisition at maximum output power 2kW and 48V$_{out}$. In this working point, the converter operates in resonant condition. Thanks to soft-switching operation the temperatures of the devices are limited to 50°C as measured with the thermal acquisition of Fig. 2.49. Figure 2.50 and Fig. 2.51 show the temperatures of the resonant inductor and planar transformer in the same working condition.
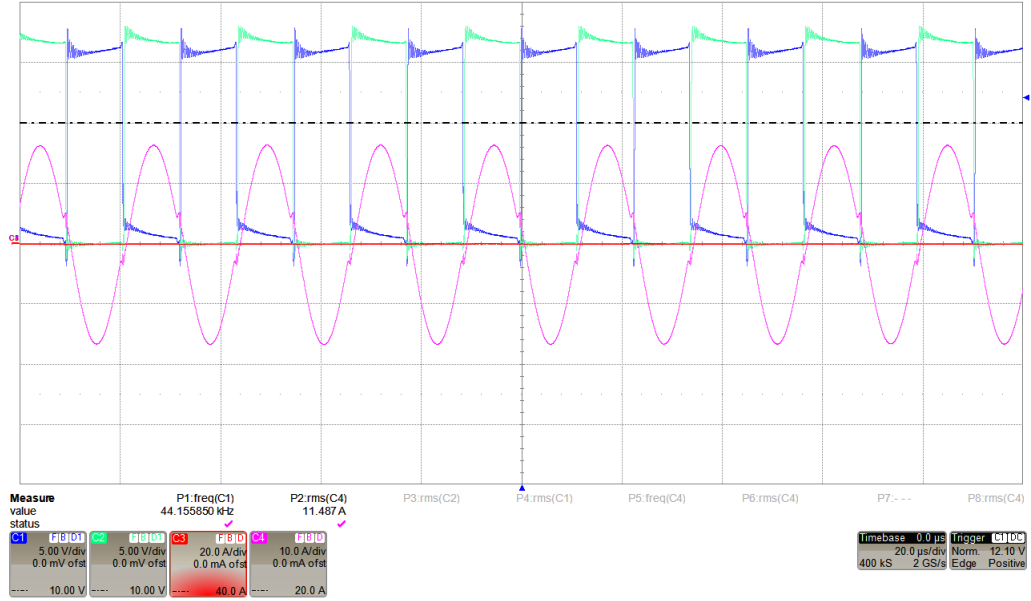

FIGURE 2.48: Oscilloscope acquisition at 48V$_{out}$ and 42ampere; Q_{HS} V_{GS} - green; Q_{LS} V_{GS} - blue; resonant tank current - purple
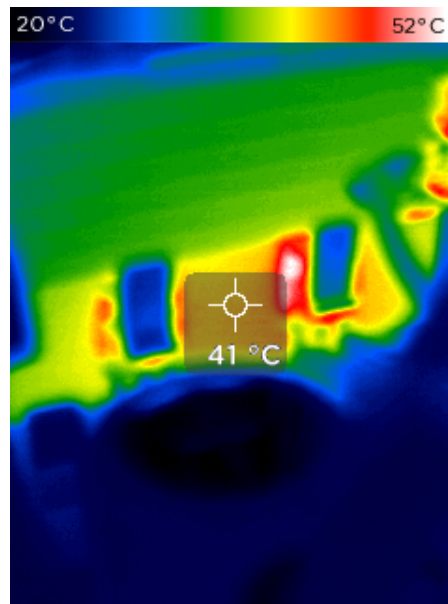

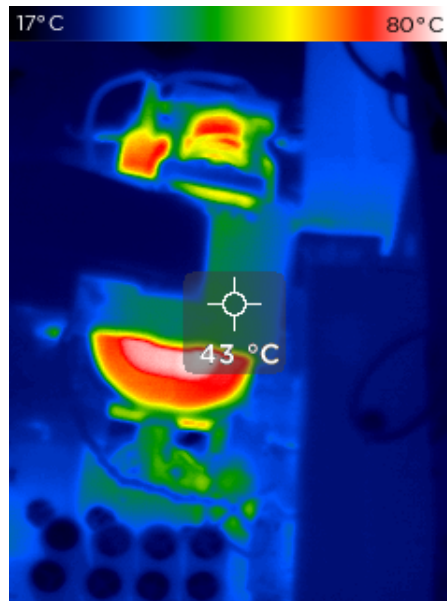FIGURE 2.49: Thermal acquisition of half-bridge with SiC device at $P_{out,max}$.

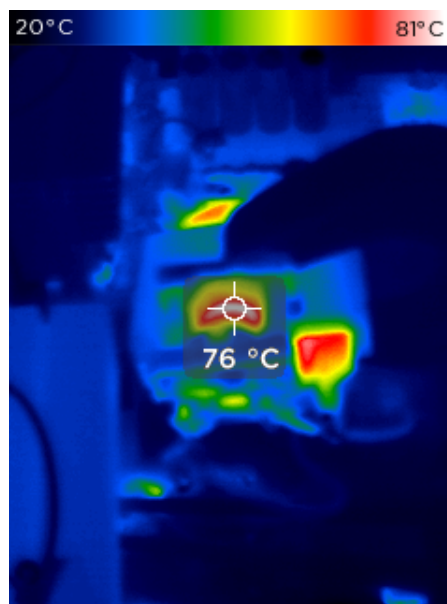FIGURE 2.50: Thermal acquisition of planar transformer (ELP64 core) at $P_{out,max}$.

FIGURE 2.51: Thermal acquisition of resonant inductor at $P_{out,max}$.

Efficiency tests were carried out at different output voltages from light to full load, as shown in Fig. 2.52, 2.53, 2.54, 2.55. The PWM operation influence over efficiency is shown by the comparison of the plot of Fig. 2.56 and Fig. 2.57. In the first one is shown the efficiency is plotted with respect to the output voltage and output current and in the second one, the PFM or PWM operation can be identified for a given couple of the same parameters. As can be seen, the efficiency is degraded when the converter operates in hard-switching condition.
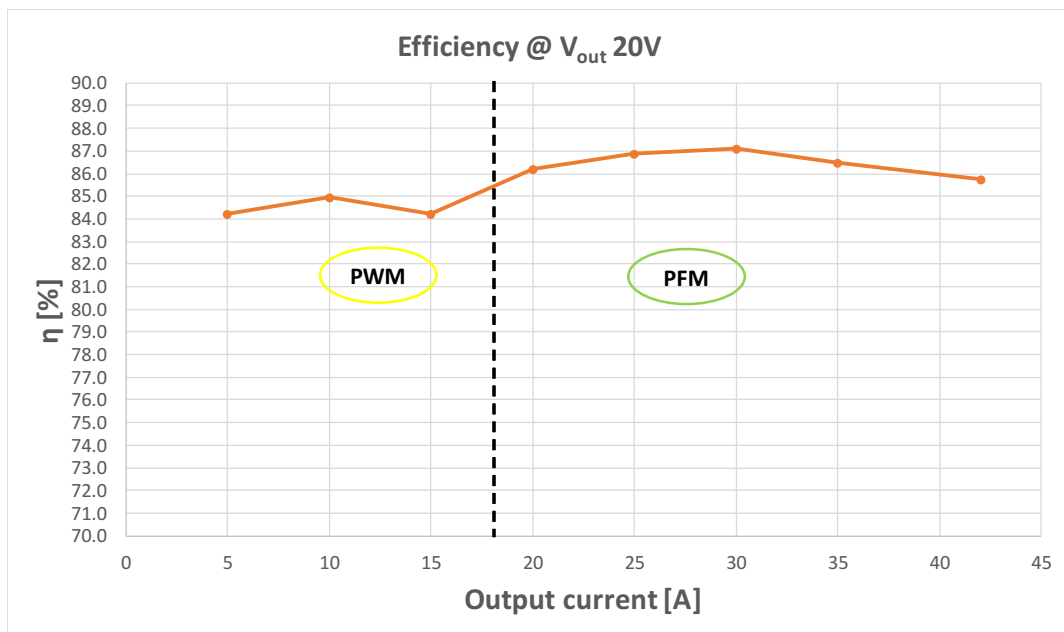
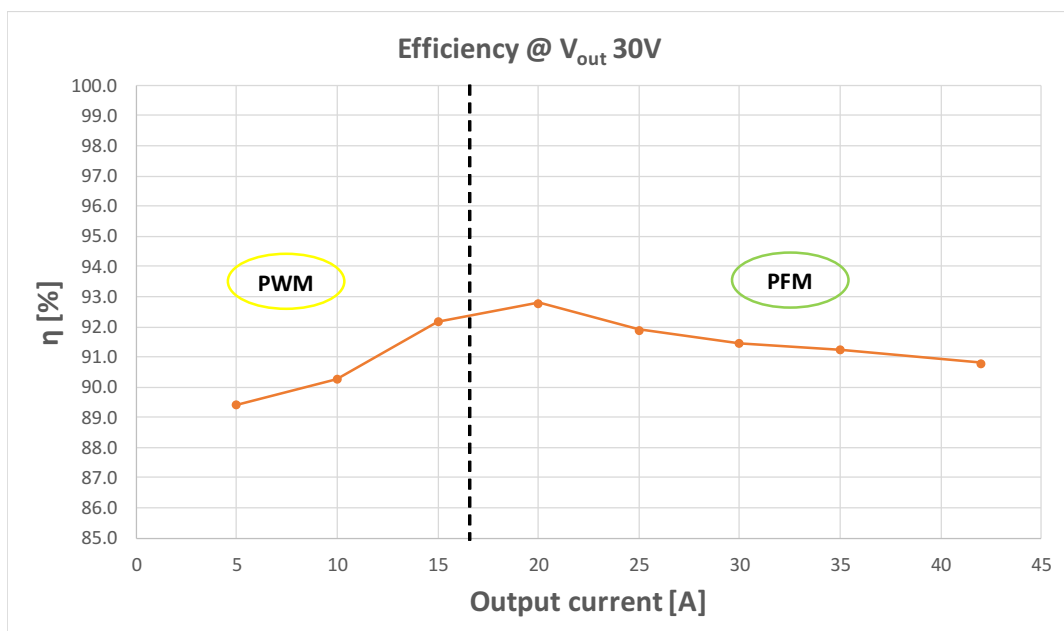FIGURE 2.52: Efficiency at 20V output from 5A to 42A

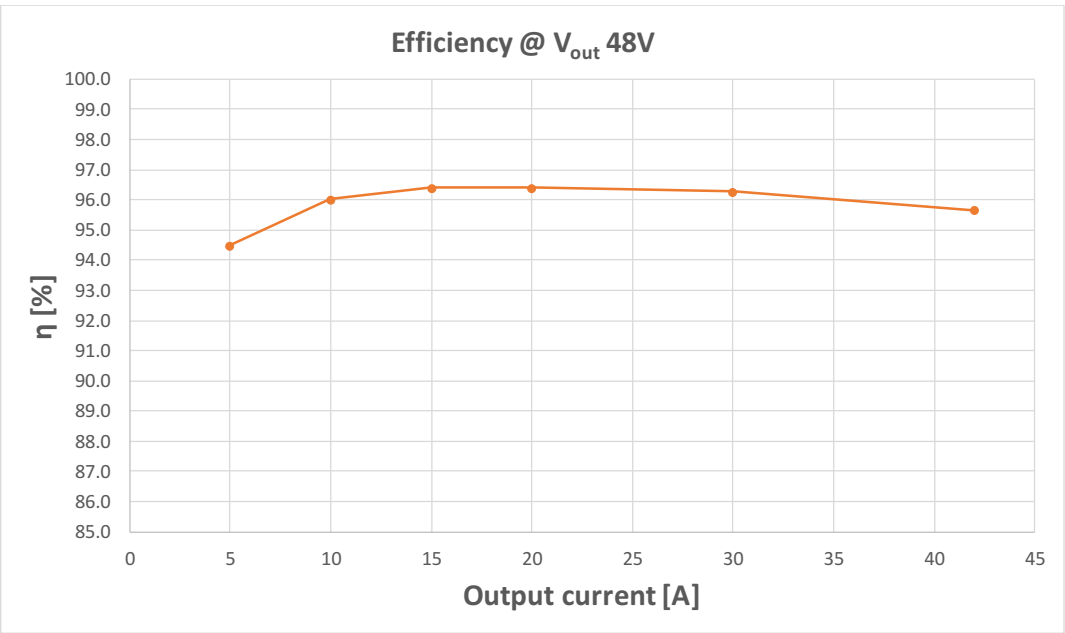FIGURE 2.53: Efficiency at 30V output from 5A to 42A

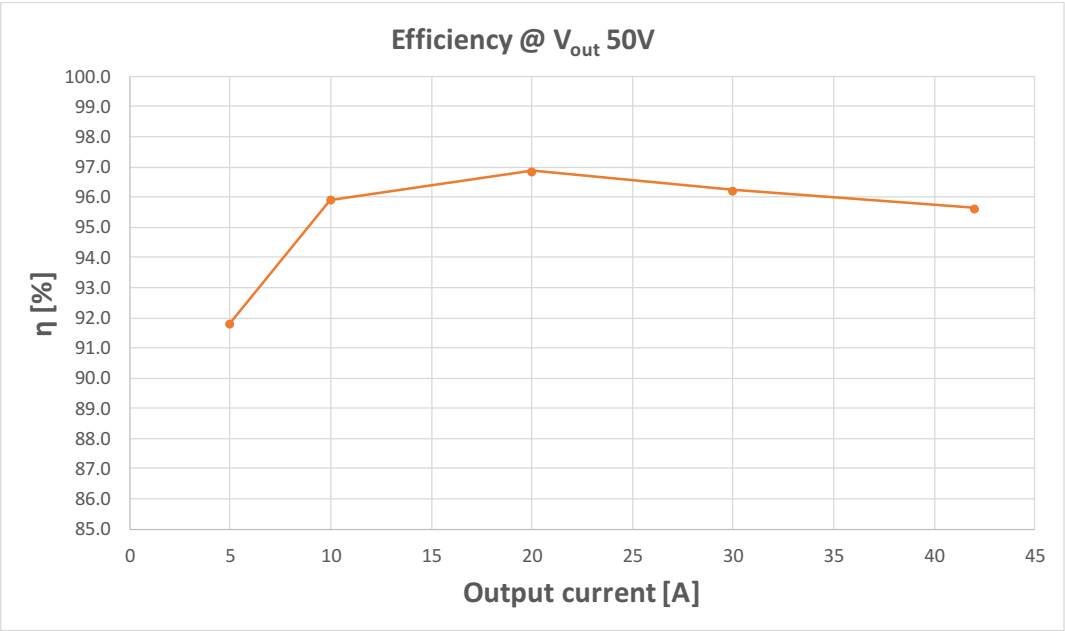FIGURE 2.54: Efficiency at 48V output from 5A to 42A

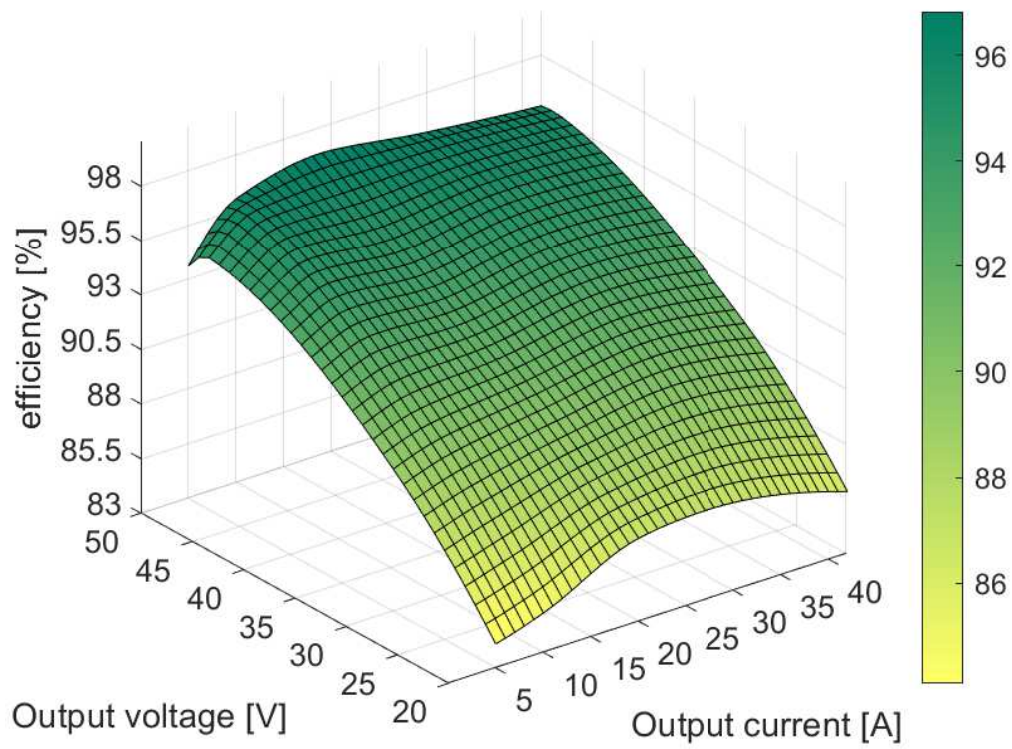FIGURE 2.55: Efficiency at 50V output from 5A to 42A

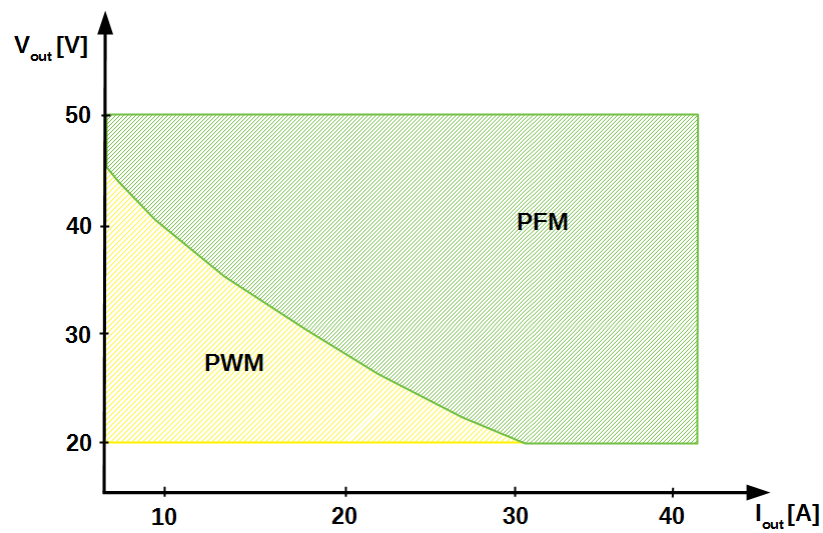FIGURE 2.56: Efficiency 3D plot of the 2kW LLC converter.

FIGURE 2.57: Working regions in PFM or PWM modulation.

2.11 Secondary leakage inductance effects on rectifier diodes

Figure 2.58 shows the presence of the secondary leakage inductances $L_{\sigma s}$ at the secondary windings of the transformer. These inductances model the secondary leakage inductance of the transformer and parasitic inductance of the PCB traces.

In center tapped configuration the diode of each branch has to sustain the doubled value of output voltage plus the voltage spike generated by the leakage inductance. The spike $V_{pk,spike}$ is due to the reverse recovery current generated by the turning off phase of the diode itself. The value of peak is equal to:

$$V_{pk,spike} = 2 \cdot V_{out} + L_{\sigma s} \frac{\Delta i_{rec}}{\Delta t_{rec}} \tag{2.43}$$

where i_{rec} and t_{rec} are the reverse recovery current and reverse recovery of the diode. The configuration of the resonant tank with an external resonant inductor and a transformer with minimum leakage inductance limit this phenomenon. The adoption of Transient Voltage Suppressors (TVS) may be necessary to protect the active devices. For the prototype, the model IPP051N15N5 is adopted as the device for the synchronous rectification stage. Two devices are paralleled in each branch to minimize the resulting $R_{ds,on}$. The MOSFET signals $Q_{SYNC,A}$ and $Q_{SYNC,B}$ are turned on by the FAN7688 LLC controller, bypassing the body diodes.
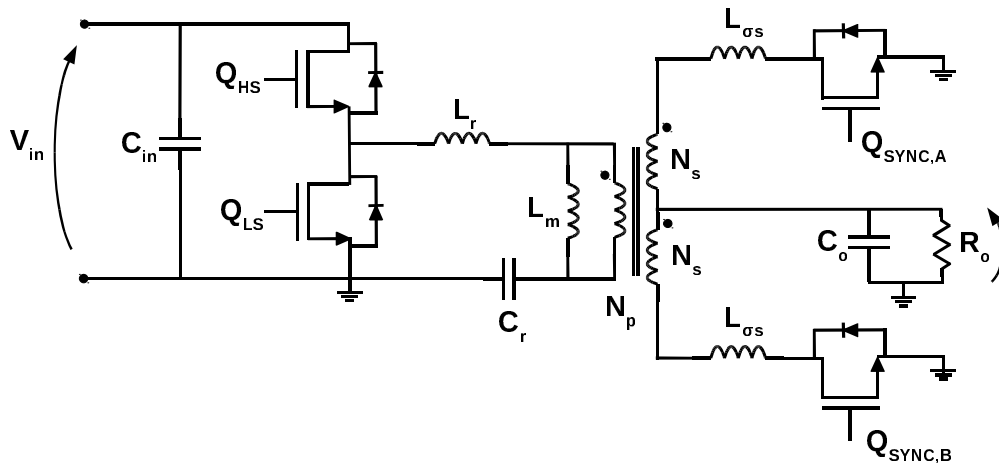
FIGURE 2.58: LLC schematic circuit with secondary leakage inductance.

Figure 2.59 shows the caption during operation ($37A_{out}$ - $48V_{out}$) without TVS installation. The spike on the source-drain voltage is near to 150V drain-source absolute maximum rating. TVSs are installed in parallel to the devices of each branch for limiting the maximum working voltage. In the caption of Fig. 2.60 the spike is sustainable by the devices.
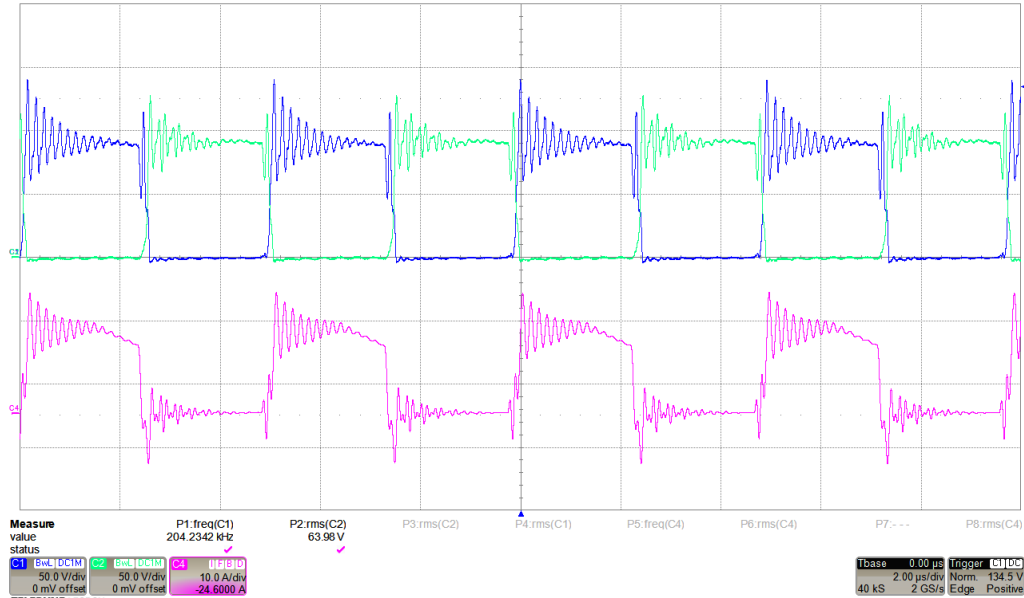
FIGURE 2.59: Synchronous rectification output stage caption without
TVSs installation. Working point: 37A$_{out}$ - 48V$_{out}$: blue and green
- drain-source voltages of MOSFET; magenta - current of MOSFET
green signal.
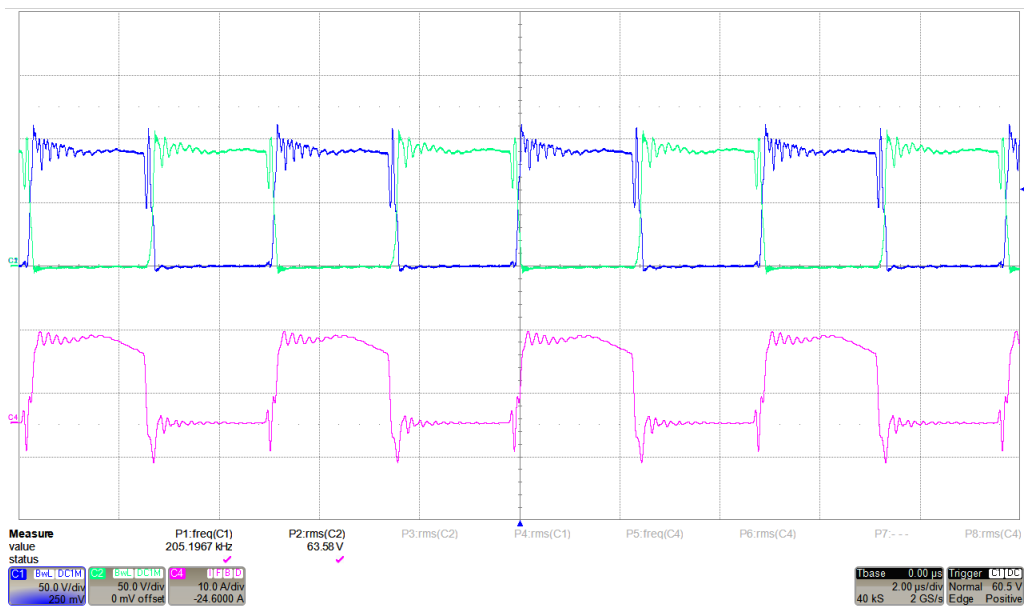
FIGURE 2.60: Synchronous rectification output stage caption with
TVSs installation. Working point: 37A$_{out}$ - 48V$_{out}$: blue and green
- drain-source voltages of MOSFET; magenta - current of MOSFET
green signal.

2.11.1   Ripple on the output voltage during PWM operation

As illustrated in section 2.5 the PWM adoption benefits the ripple of the output volt-
age during light load operation. The controlled adopted in the prototype imple-
ments the hybrid modulation strategy PFM-PWM mode. In Figure 2.61 is shown
that the voltage ripple measured during PWM operation is limited to few volts.

FIGURE 2.61: Caption of output voltage ripple in PWM control. Working point $7A_{out}$ - $35V_{out}$ $f_{sw} = 160$kHz. Output voltage - blue; primary current - magenta

2.12 Asymetric PWM effects on synchronous rectification stage

In the previous section 2.4 has been shown by the Figure 2.23(b) the "asymmetric" PWM modulation technique adopted to obtain soft-switching condition switching when the low side MOSFET is turned on after the dead time 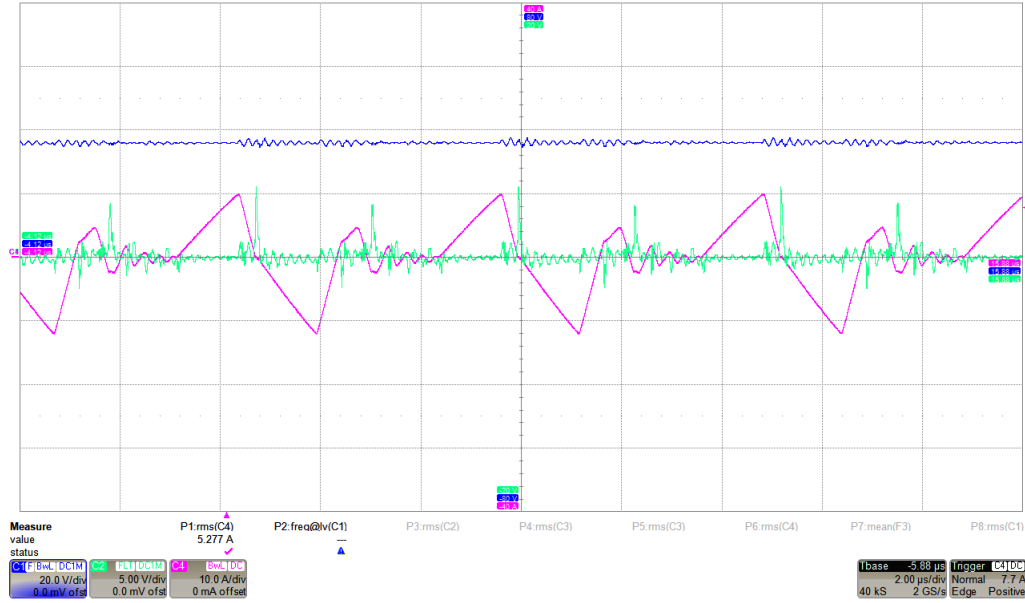period. The value of the dead time is sufficient for the magnetizing current to charge/discharge the midpoint capacitance C_{MP}. Despite all, under this operating conditions has been stated that there is not an equal distribution of the losses, but the temperature of the high side device is higher, as shown by the thermal acquisition of Fig. 2.47(a). Another effect of this PWM modulation technique is observed on the current unbalance of the secondary windings. Figure 2.62 shows the acquisition obtained simulating on PLECS the converter working in PWM mode. The current flowing through one winding is more with respect the other. Looking at Fig. 2.63 is possible to notice magnetizing current is not symmetrical during asymmetric PWM operation because the low side MOSFET is turned on at different value of the magnetizing current with respect to the high side device. This result in an unbalanced current transferred at the secondary windings.

Figure 2.64 shows an experimental caption of the LLC prototype during the same PWM working point adopted for the simulations. The primary current is unbalanced and due to this, looking at the drain-source voltages of the MOSFET of the synchronous rectification stage, the body diode of one branch is not conducting over the full half-period. The thermal acquisition of Fig. 2.65 shows that thermal unbalance happens at the secondary side as well, on the body diode that is sustaining more current.
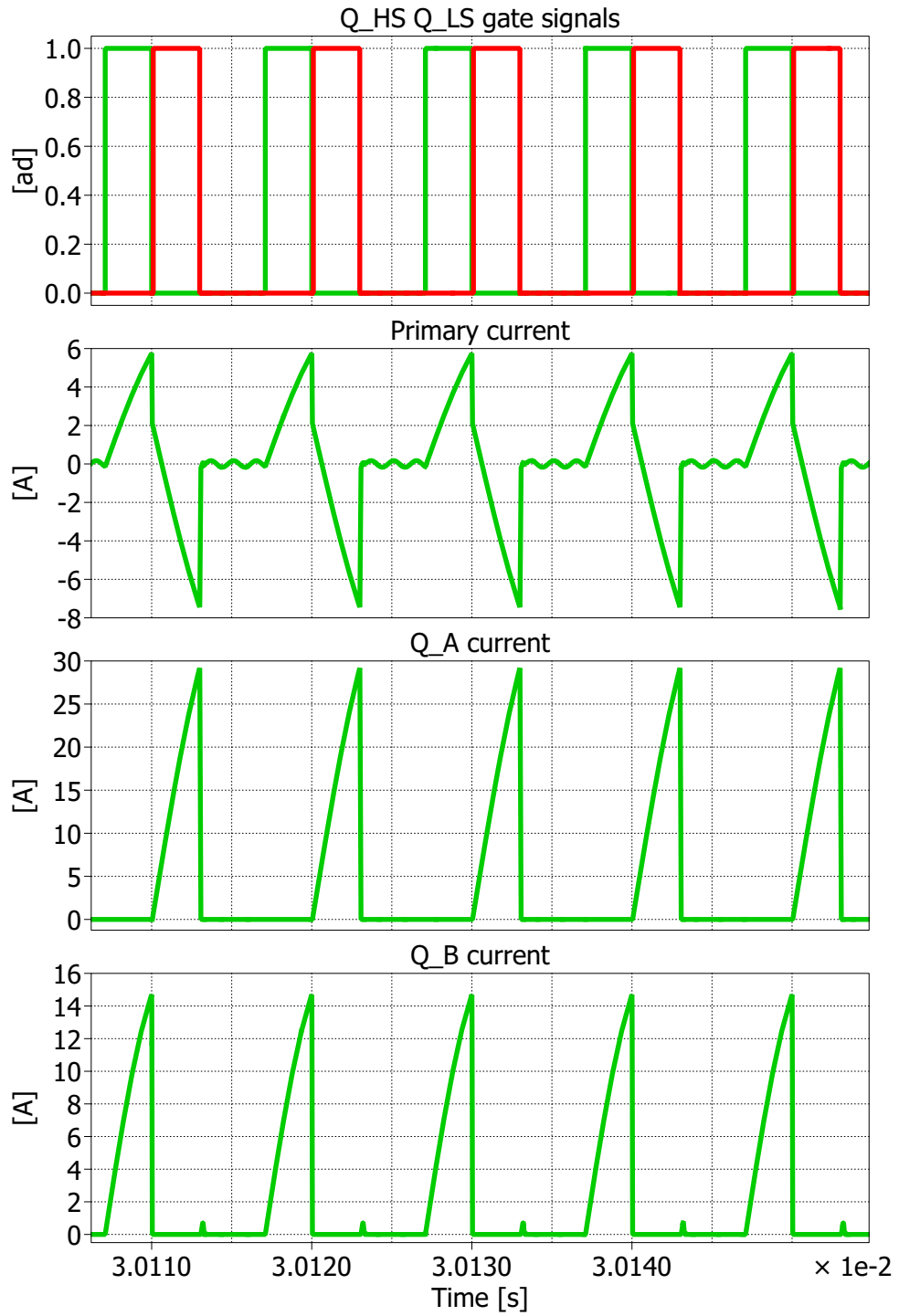
FIGURE 2.62: PLECS simulation asymmetric current at 7A$_{out}$ - 48V$_{out}$
$f_{sw} = 50$kHz $duty = 0,3$. First plot: Q_{HS} and Q_{LS} gate signals. Second plot: primary current. Third plot: $Q_{SYNC,A}$ currents. Fourth plot:
$Q_{SYNC,B}$ currents.
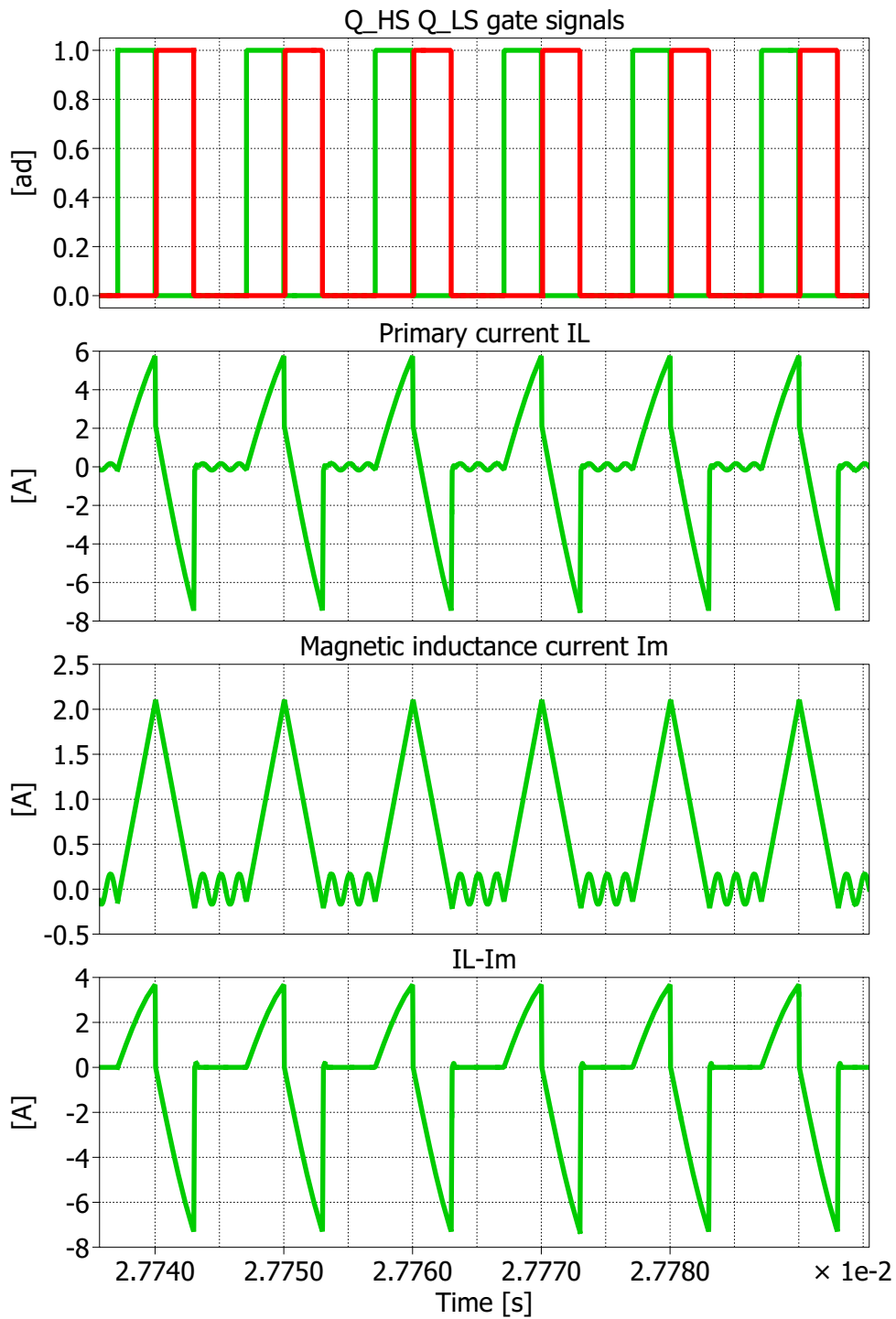
FIGURE 2.63: PLECS simulation asymmetric current at $7A_{out}$ - $48V_{out}$ $f_{sw} = 50kHz$ $duty = 0,3$. First plot: Q_{HS} and Q_{LS} gate signals. Second plot: primary current. Third plot: magnetic inductance currents. Fourth plot: primary current transferred to secondary side.
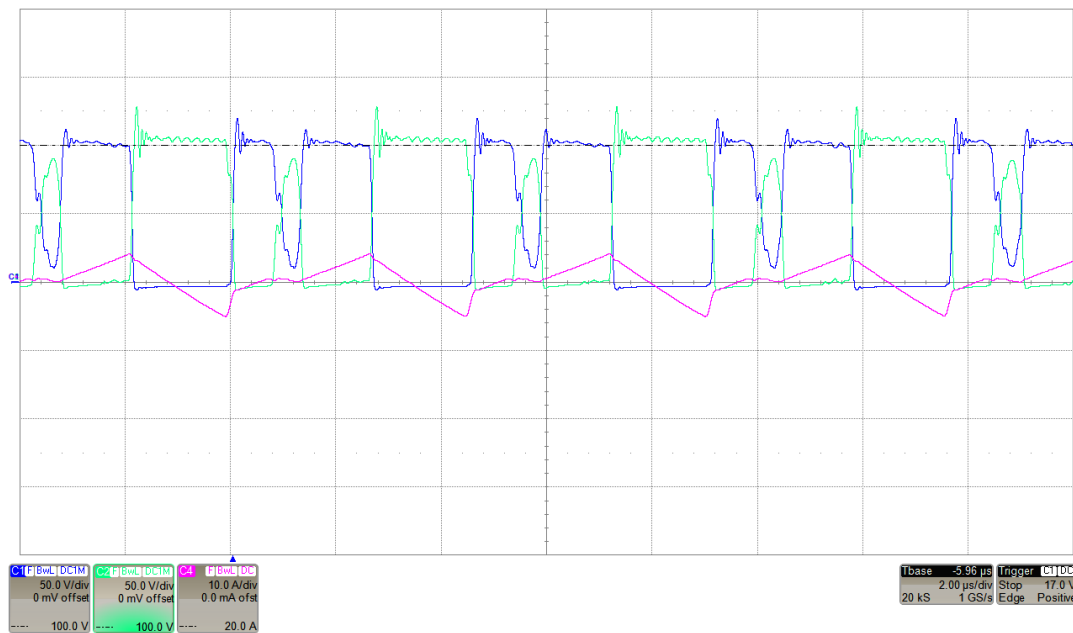
FIGURE 2.64: Caption of asymmetric current during PWM opera-
tion (7A$_{out}$ - 50V$_{out}$): $Q_{SYNC,B}$ drain-source voltage - green; $Q_{SYNC,A}$
drain-source voltage - blue; primary current - magenta.
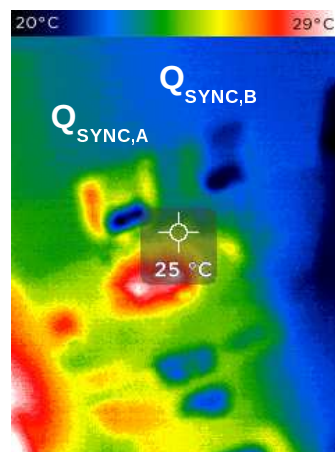
FIGURE 2.65: Thermal distribution losses on synchronous rectifica-
tion stage during asymmetric PWM modulation (7A$_{out}$ - 50V$_{out}$).

2.13 Conclusion

This chapter has presented a brief introduction to resonant converter topologies and how they are involved in the transport electrification. The design of a 2kW was described, focusing on the resonant parameters properly sized for wide voltage capability. The design of the power planar transformer was presented and an external resonant inductor was adopted to realize the leakage inductance at primary side. The following part of the chapter analysed the benefits, drawbacks and critical aspects of the PWM adoption at light load operation. The PWM modulation is useful to extend the continuous switching operation at low output voltage / low output power, thus obtaining a reduction of output voltage ripple for a given size of the output capacitor. With classic PWM modulation, both the high side and the low side switches have a hard-switching commutation. A modulation strategy able to reduce the hard-switching commutations was identified and evaluated. With optimized PWM strategies, the overall losses can be reduced, but the free oscillation frequency of the resonant tank current during the t_{off} can result in increased losses at the restart of the modulation. As a result, the turn-on losses are always allocated to the first device starting the PWM sequence (in the present work Q_{HS}). The proposed solution to this unwanted behaviour is the introduction of an *Adaptive PWM* technique based on Quasi-Resonant control, that is able to exploit the free oscillation. After a first analytic assessment, the impact on turn-on losses of the proposed Adaptive PWM was evaluated by means of numerical simulations and was described a possible implementation. The control waits for one of the valleys in V_{DS} of Q_{HS} before switching on the device. With this strategy, the ZVS is guaranteed for the Q_{HS} regardless of Si or SiC MOSFETs adoption and the switching losses are minimized. The laboratory prototype enabled to identify the losses distribution and demonstrated the benefits introduced by SiC devices both on dead time requirement and free oscillation. The experimental results have validated the design of the converter and the efficiency curves were obtained at different operating points.

Bibliography

[1] J. Park and S. Choi. "Design and Control of a Bidirectional Resonant DC–DC Converter for Automotive Engine/Battery Hybrid Power Generators". In: *IEEE Trans. on Power Electronics* 29.7 (July 2014), pp. 3748–3757. ISSN: 0885-8993. DOI: 10.1109/TPEL.2013.2281826.

[2] Jiangheng Lu and A. Khaligh. "1kW, 400V/12V high step-down DC/DC converter: Comparison between phase-shifted full-bridge and LLC resonant converters". In: *2017 IEEE ITEC*. June 2017, pp. 275–280. DOI: 10.1109/ITEC.2017.7993284.

[3] B. Yang, F. C. Lee, and M. Concannon. "Over current protection methods for LLC resonant converter". In: *APEC '03*. Vol. 2. Feb. 2003, 605–609 vol.2. DOI: 10.1109/APEC.2003.1179276.

[4] P. Horowitz and W. Hill. *The Art of Electronics*. Cambridge University Press, 2015. ISBN: 9780521809269.

[5] Francesco Di Domenico, Alois Steiner, and Johnald Catly. *Design of a 600 W HB LLC Converter using 600V Cool MOS^{TM} P6*. Revision1.0, 2015-07-31.

[6] E. C. W. de Jong, E. C. W. de Jong, B. J. A. Ferreira, and P. Bauer. "Toward the Next Level of PCB Usage in Power Electronic Converters". In: *IEEE Transactions on Power Electronics* 23.6 (Nov. 2008), pp. 3151–3163. DOI: 10.1109/TPEL.2008.2004276.

[7] C. Quinn, K. Rinne, T. O'Donnell, M. Duffy, and C. O. Mathuna. "A review of planar magnetic techniques and technologies". In: *APEC 2001. Sixteenth Annual IEEE Applied Power Electronics Conference and Exposition (Cat. No.01CH37181)*. Vol. 2. Mar. 2001, 1175–1183 vol.2. DOI: 10.1109/APEC.2001.912514.

[8] S. R. Cove, M. Ordonez, and J. E. Quaicoe. "Modeling of planar transformer parasitics using design of experiment methodology". In: *CCECE 2010*. May 2010, pp. 1–5. DOI: 10.1109/CCECE.2010.5575138.

[9] Z. Ouyang, O. C. Thomsen, and M. A. E. Andersen. "The analysis and comparison of leakage inductance in different winding arrangements for planar transformer". In: *2009 International Conference on Power Electronics and Drive Systems (PEDS)*. Nov. 2009, pp. 1143–1148. DOI: 10.1109/PEDS.2009.5385844.

[10] Alexander J. Young. "Characterizing the dynamic output capacitance of a MOSFET". In: *EDN Network* (Sept. 2013).

[11] Helen Ding. *Design of Resonant Half-Bridge converter using IRS2795(1,2) Control IC*. AN-1160.

[12] W. Feng, F. C. Lee, and P. Mattavelli. "Optimal Trajectory Control of Burst Mode for LLC Resonant Converter". In: *IEEE Trans. on Power Electronics* 28.1 (Jan. 2013), pp. 457–466. ISSN: 0885-8993. DOI: 10.1109/TPEL.2012.2200110.

[13] Fairchild. *FEBFAN7688-I00250A*. Revision 1.0, August 2015.

[14]   R. Fornari, G. Migliazza, E. Lorenzani, and F. Immovilli. "Critical Aspects of Hybrid PFM-PWM Operation in LLC Converters For Electric Vehicles". In: *2018 IEEE International Conference on Electrical Systems for Aircraft, Railway, Ship Propulsion and Road Vehicles International Transportation Electrification Conference (ESARS-ITEC)*. Nov. 2018, pp. 1–6. DOI: 10.1109/ESARS-ITEC.2018.8607763.

[15]   Seok-Bae Park, J. E. Wilson, and M. Ismail. "The CHIP - Peak Detectors for Multistandard Wireless Receivers". In: *IEEE Circuits and Devices Magazine* 22.6 (Nov. 2006), pp. 6–9. ISSN: 1558-1888. DOI: 10.1109/MCD.2006.307270.

[16]   Hui-Yung Chu, Hurng-Liahng Jou, and Ching-Lien Huang. "Transient response of a peak voltage detector for sinusoidal signals". In: *IEEE Transactions on Industrial Electronics* 39.1 (Feb. 1992), pp. 74–79. ISSN: 1557-9948. DOI: 10.1109/41.121914.

[17]   S. Lee, T. Vu, and H. Cha. "A new fast peak detector for single or three-phase unsymmetrical voltage sags". In: *2010 IEEE Energy Conversion Congress and Exposition*. Sept. 2010, pp. 434–440. DOI: 10.1109/ECCE.2010.5617993.

Chapter 3

Dual Active Bridge converter design

3.1 Bidirectional DC-DC converter for electric vehicles

Chapter 1 has dealt with the architectural typologies of HEVs and Full EVs. Different energy sources such as batteries, ultracapacitors or fuel cells can be used by the vehicle to provide the power to the drive train. Figure 3.1 gives an illustrative representation of a bidirectional DC-DC power converter installed on the vehicle that interfaces the energy source with the drive train. The represented scheme is intentionally generic because the possibles configurations are many and varied, are related to the vehicle typology (hybrid or full electric) and to the kind of architecture (series, parallel, series-parallel) [1].
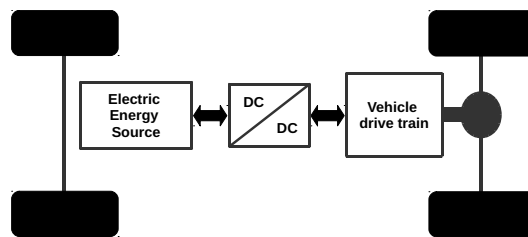
FIGURE 3.1: Bidirectional DC-DC power converter inside an EV's architecture.

The bidirectionality is required to deliver energy from the energy source to the load and to manage the regenerative braking. The battery or capacitors voltage typically is lower than the dc-link. In the automotive range 400V is considered a good tradeoff between the converter current load and costs for drive trains up to 100kW [2]. In the case of Fig. 3.2 Fuel Cells are directly linked to the dc-link, the available bus voltage is load dependent and it varies with the dynamic of the vehicle[3]. In this case, the converter has to transfer power in a wide voltage operating range at HV dc-link. Also, the battery side is affected by a wide voltage variation depending on the state of charge.

FIGURE 3.2: Power system architecture of a EV with Fuel Cells.

The galvanic isolation between HV dc-link and LV dc-link is required for safety reasons. The design of the converter for automotive application has to meet other requirements such as low costs design, minimization of size and number of comp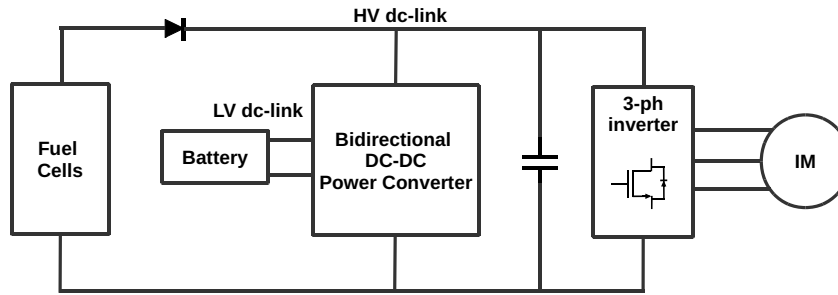onents. These constraints are achieved increasing the switching frequency and by providing for modularity. The maximization of the efficiency over a wide input and output power range is a critical issue that involves the efficiency of the overall drive train. Many challenging tasks are involved by the design of a DC-DC converter used as a power interface of HEV's or EV's energy sources. During high power operations high currents flow at the low voltage side, increasing the thermal stresses of the components. The EMI emissions make difficult to match the costs, weight and dimensional constraints of the converter [4]. Thus, from these aspects comes the need for an efficient, compact and cost-effective isolated bidirectional DC-DC converter design.

In the electric transportation field, the application of a bidirectional DC-DC converter is not limited to an on-board use. It can be applied as off-board battery charger [5], [6], [7], [8]. The idea of green transportation is EVs that have zero gas emission charging their battery from clean renewable sources. In a "Smart Home" [9, 10] the residential unit is equipped with distributed energy resource (among them, PV), coupled with energy storage in order to maximize self-consumption of the produced energy [11]. Because of increased demand for electrical energy storage in case of overproduction in grid-tied renewable energy plants, bi-directional converter architectures are extremely interesting for interfacing the storage unit. Designed targets are characterised by high efficiency and wide voltage ratio operations. Safety requirements imply the use of galvanically insulated topologies, preferably single-stage, to reduce the number of intermediate energy conversions.

The widespread of green energy sources can be exploited to help the EVs charging during the high phase production or considering the EV's batteries as storage systems during these phases. The V2G concept [12] requires the capability of the vehicle to sustain the grid returning energy during peak hours. Figure 3.3 gives an illustrative representation of a PV charging station: the EV is connected through the battery charger to the DC bus, linked to the PV source and to the grid.
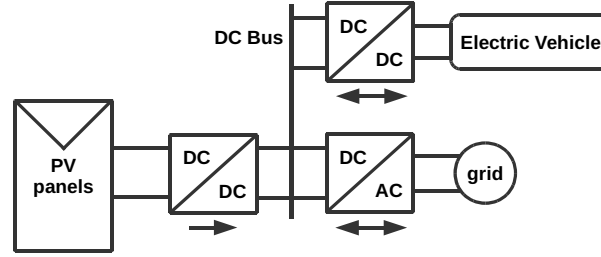
FIGURE 3.3: PV charging station with indicated power flow directions.

In this configuration the DC-DC converter used to charge the EV's battery pack is isolated and has the ability to transfer power in a bidirectional way with a wide input-output voltage range. Depending on the state of charge the power to transfer varies in a wide range as well.

This chapter deals with the design of wide input-output voltage range Dual Active Bridge (DAB). Full size 3, 2kW prototype was manufactured and experimental validation was carried out. The DAB is a galvanic isolated bidirectional single-stage DC/DC converter based on two active bridges [13] that offers galvanic insulation. Bi-directional resonant converters are other converter typologies investigated in literature [14]. Simple DAB with traditional phase shift modulation does not offer a good efficiency in wide voltage/power applications [15]. Wide voltage range operation can be obtained by adopting two-stage cascaded topologies or using advanced modulation techniques [16]. The design of the DAB involves a tradeoff between a good efficiency over a wide power range and high full-load efficiency at the nominal voltage, [17]. With more advanced modulation techniques the soft-switching can be extended over a wider voltage and power ranges, alternatively the number of hard-switching commutations over one switching cycle can be kept to a minimum [18]. The DAB converter was designed adopting two alternative modulation sequences, Trapezoidal or Triangular, depending on the input/output voltage level and the required power to transfer. An open loop control of the DAB converter based on its mathematical model was implemented together with a simple feed forward compensation of non-idealities.

3.2 DAB control and design

For the intended application, the design of the DAB (the schematic circuit is reported in Fig. 3.4) involves a tradeoff between the maximum power transferable over the wide voltage range and the maximum currents on the semiconductor devices.
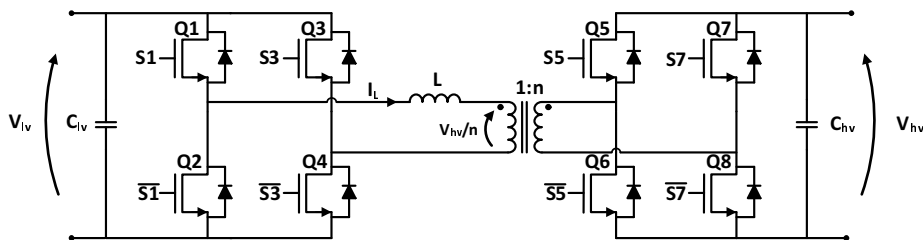

FIGURE 3.4: Schematic circuit of the DAB topology converter.

Figure 3.5 shows the voltage range where rated power of 3, 2kW is guaranteed and the power derating region for lower HV side voltage values (to avoid over-current in semiconductor devices). This section describes the design of the DAB converter starting from these specifications.
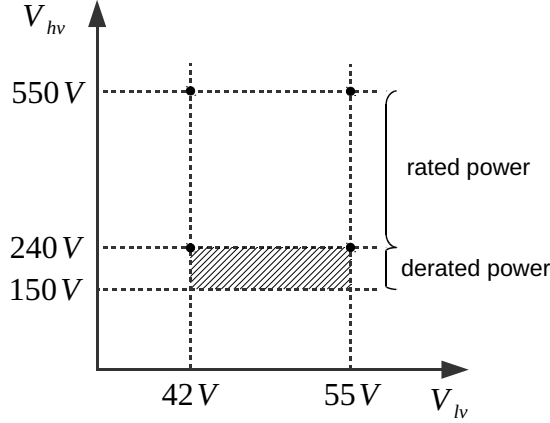

FIGURE 3.5: Complete DAB operating range, detailing the different regions of operation.

Three main PWM strategies can be adopted for DAB converters: Rectangular, Trapezoidal and Triangular modulation strategies. The Rectangular modulation is well-known and widely adopted, the other two more advanced modulations are aimed at reducing the number of hard-switching commutations over one period, especially in case of wide voltage range operation:

1. In the Rectangular modulation the shift between the two bridge defines the effective power transferred from one side to the other side. The main disadvantages of this modulation are: large *rms* currents in the transformer and limited operating range with low switching losses, when the converter works over wide voltage ranges [19].

2. In case of Trapezoidal modulation, the relevant waveforms are shown in Fig. 3.12. This modulation is adopted at higher power level. As reported in [18], the maximum transferable power in Trapezoidal mode $P_{trap,max}$ is equal to:

$$P_{trap,max} = \frac{((V_{lv} \cdot V_{hv})/n)^2}{4 f_s L (V_{lv}^2 + V_{lv} \cdot V_{hv}/n + (V_{hv}/n)^2)} \tag{3.1}$$

Equation (3.1) shows that the higher is the input-output voltage difference, the higher is the maximum transferable power in Trapezoidal mode. This modulation can not be adopted when the voltage at the one side tends to zero, e.g. at startup.

3. When transferring lower power levels, it is useful to further limit the number of hard-switching commutations over one period. In case of Triangular modulation, the relevant waveforms are shown in Fig. 3.14. Due to the discontinuous conduction modulation, the Triangular modulation minimizes the

number of commutations in the switching period. The maximum transferable power $P_{tri,max}$ is equal to [18]:

$$P_{tri,max} = \frac{(V_{hv}/n)^2 \cdot |(V_{lv} - V_{hv}/n)|}{4 f_s L V_{lv}}$$

(3.2)

The $P_{tri,max}$ matches with the minimum power transferable in Trapezoidal mode. In fact, the Triangular modulation can be considered as a particular case of the Trapezoidal modulation. Similarly to Trapezoidal case, in Triangular mode higher is the input-output voltage difference, higher is the maximum transferable power. However, when the voltages at the two side tend to be equal to the turns ratio n, the transferable power drops to zero.

Figure 3.6 shows the strategy control of the DAB converter. Two operating modes are provided by the Modulator depending on the sign of the power setpoint:

- Charge mode: the energy flows from the high voltage side to the low voltage side.

- Discharge mode: the energy flows from the low voltage side to the high voltage side.

The DAB Control block defines the Trapezoidal or Triangular modulation pattern for driving the two full-bridges, given the operating point defined by the measured V_{lv}, V_{hv} and by the desired transferred power P^*. The dwell times T_H, T_L and the phase shift between the dwell times phs_{dw},are computed according to [18, 20].
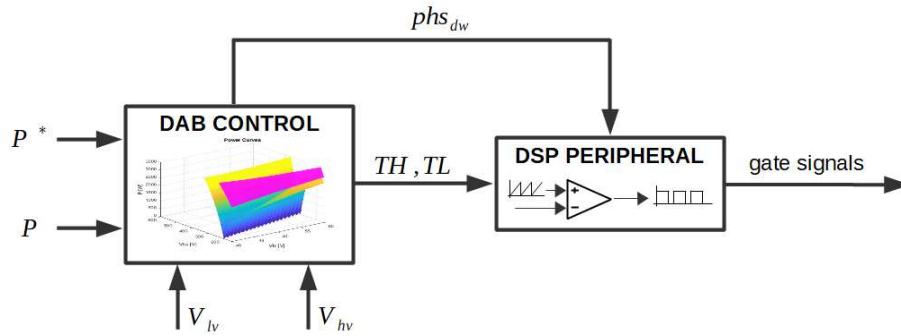
FIGURE 3.6: Schematic of the DAB Modulator.

3.2.1 Series inductance selection and magnets design

In the present work, the DAB interfaces at the low voltage side V_{lv} a battery pack with nominal voltage 48V, peak voltage 55V, minimum voltage 42V. As shown graphically by Fig. 3.5, the low voltage range V_{lv} is 42V-55V and the high voltage range V_{hv} is 150V-550V. The rated power should be met only in the range 240V-550V for V_{hv} side, while a power derating curve is followed at lower voltage range 240V-150V, as limitations due to the switches current rating.

In designing the converter, the primary side series inductance L is sized in case of Trapezoidal modulation. As stated before, this modulation allows the converter to

exploit the maximum transferable power. The value has to be selected identifying the worst case of input-output voltages, in order to guarantee the desired rated power in such condition [18]. Substituting the rated power value P_o in the variable $P_{trap,max}$ of eq. (3.1) it is possible find the value of the primary inductance needed to obtain P_o as a function of transformer turn ratio n, input-output voltages V_{hv}, V_{lv} and the switching frequency f_s:

$$L = \frac{((V_{lv} \cdot V_{hv})/n)^2}{4f_s P_o(V_{lv}^2 + V_{lv} \cdot V_{hv}/n + (V_{hv}/n)^2)} \tag{3.3}$$

The values of n and L are closely related to guarantee the rated power achievement. Different values can satisfy this constraint and an iteration process is needed. Figure 3.7 plots eq. (3.3) obtained with $n = 5$ and using the converter parameter listed in Tab. 3.1. Each point of the plotted surface corresponds to the inductance value requested to transfer the nominal power, for the given couple of V_{hv} and V_{lv} values.
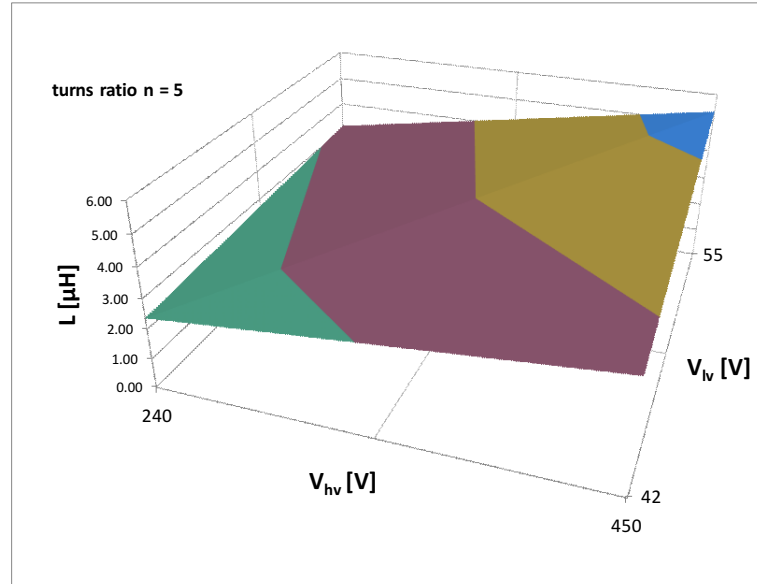
FIGURE 3.7: Plot of the maximum permissible inductance value L in
order to transfer the rated power.

Name	Value
P_o [W]	3200
V_{hv_max} [V]	450
V_{hv_min} [V]	240
V_{lv_max} [V]	55
V_{lv_min} [V]	42
f_s [kHz]	22

TABLE 3.1: DAB specification used for the series inductance value
selection.

The values of L computed at the four extreme points of the working area are listed in Tab. 3.2. By choosing the minimum of the computed values (considering a sufficient margin due to the design tolerance of the magnet components), the converter is able to transfer the rated power all over this area.

	Vhv [V]		
	L [µH]	240	450
Vlv [V]	42	**2,37**	**3,72**
	55	**3,11**	**5,41**

TABLE 3.2: Series inductance values computed at the four edge points of the input-output voltage operating region.

Figure 3.8 shows the boundary surfaces of transferable power plotted in Trapezoidal and Triangular modulation with the chosen values of $n = 5$ and $L = 2,0\mu H$. Outside of the "V" surface the Modulator (Fig. 3.6) adopts the Triangular modulation, inside it adopts the Trapezoidal modulation. The magenta surface identifies the maximum power that can be transferred in Trapezoidal modulation.
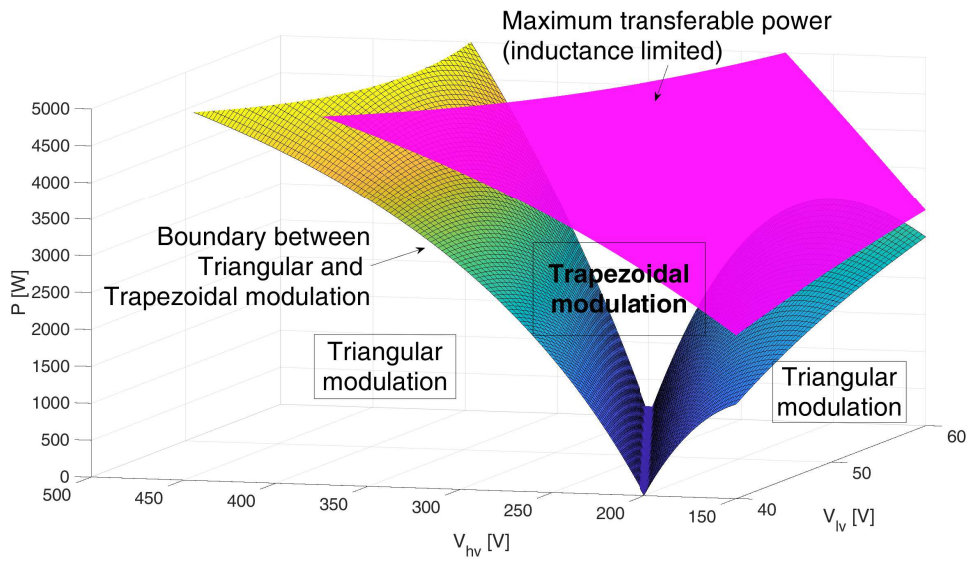
FIGURE 3.8: Triangular and Trapezoidal Power Curves. Colour surface identifies $P_{tri,max}$ and magenta surface identifies $P_{trap,max}$.

Figure 3.9 shows the prototyped magnets. The series inductance is realized with an external inductor and exploiting the leakage inductance of the transformer. The inductor is placed at the secondary side and is realized with a powder core (distributed air gap). The main characteristics of the magnets are listed in Tab. 3.3. The design practices are the same described in the Chapter 2 while the current and voltage specifications were obtained by PLECS models.

(a)   (b)

FIGURE 3.9: (a) Series inductance realized with a powder core (b) Transformer realized with two E70/33/32 cores.

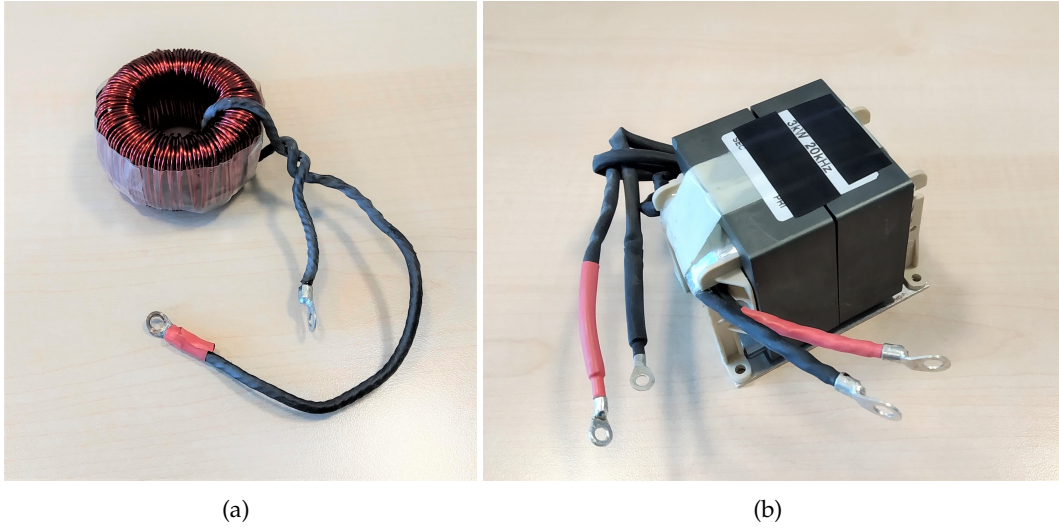| Characteristics	value
Transformer turns ratio n	5
Magnetic Inductance L_m [mH]	1,7
Inductance at primary side (ext. inductor + trafo leakage) L [μH]	1,94
Peak primary current $I_{L,peak}$ [A]	196,9
Maximum rms primary current I_{L,rms_max} [A]	100
Insulation specifications	**value**
Coils to core [kV]	2
Primary to secondary [kV]	4
Core characteristics	**value**
Inductor core	powder core
Transformer core	2xE70/33/32

TABLE 3.3: Magnets parameters and building specifications.

3.2.2 Control loop and feed forward compensation

The DAB Control block of Fig. 3.6 starting from the desired transferred power P^* for the different cases (Trapezoidal or Triangular modulation and discharging or charging phase, [20, 18]) computes the dwell times T_H and T_L. The computed dwell times are then translated into the PWM signals for the switching devices of both H bridges by the DSP peripheral.

It is important to highlight that the dwell times and the following PWM signals are computed in open loop (i.e. in feed forward) without the feedback of any current loop on the transformer side and that the dead time is analytically compensated.

Dead time compensation is applied according to the modulation adopted. In the case of Trapezoidal modulation, the theory for dead time compensation was first described in [20]. The formulas for dwell time computation presented in [18] were properly modified for the triangular case. Dead time compensation is carried out

considering a delay on the rising edge of the gate signal, with the aim to avoid DC offset application to the HF transformer. Feed forward operation of the DAB Control block requires precise knowledge of the DAB converter parameters, especially the primary side series inductance L. Because of manufacturing tolerances on the wound components (transformer leakage inductance, external series inductance), it is unavoidable in feed forward operation that an error appears between the desired transferred power and the actual one. This small error was simply eliminated modifying P^* in order to obtain the desired measured transferred power with the use of a traditional PI regulator, as illustrated by Fig. 3.10.
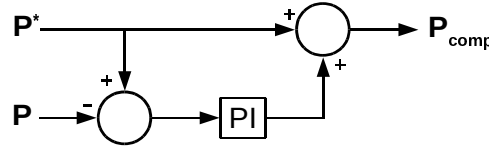
FIGURE 3.10: Feed forward compensation block used to compute the DAB control setpoint power P_{comp}.

The value of the power P_{comp} is used as setpoint by the DAB control to compute the dwell times and the phase shift, according to the flow chart of Fig. 3.11. The case of the figure is relative to the conditions of $V_{lv} < V_{hv}/n$ and $P_{mod} < 0$ for trapezoidal and triangular modulation cases.

FIGURE 3.11: Flow chart of the DAB control when $V_{lv} < V_{hv}/n$ and $P_{mod} < 0$.

3.3   Switching and conduction losses analysis

In this section the switching and conduction losses are analysed for the Trapezoidal and Triangular modulation [21] and considerations on the characteristics of the silicon device to take into account will be done on the base of the obtained results. The modulation scheme in Trapezoidal or Triangular mode depends on relation between the value of the reflected secondary voltage with respect to the primary voltage:
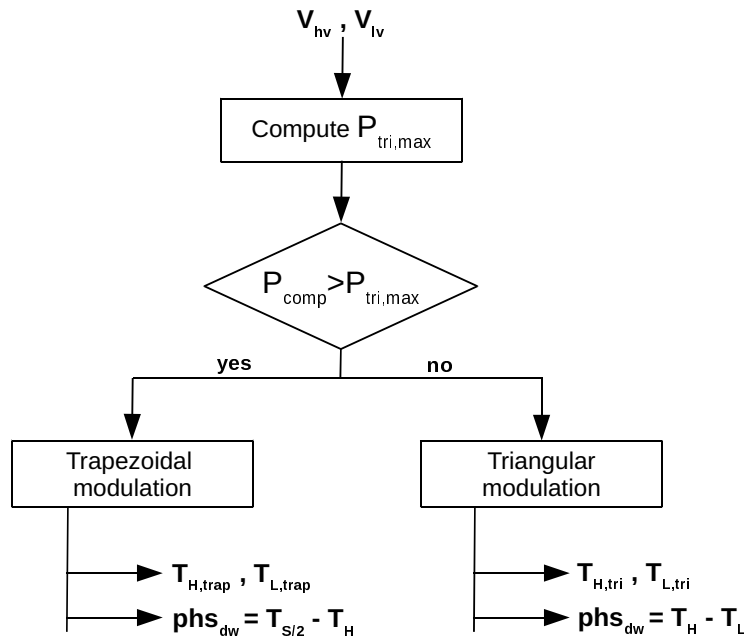
$$\begin{cases} V_{lv} > V_{hv}/n \\ V_{lv} < V_{hv}/n \end{cases} \tag{3.4}$$

Figure 3.12 and Fig. 3.14 show current and voltage waveforms in Trapezoidal and Triangular modulation.
The commutation sequence of the devices in Trapezoidal modulation when the reflected voltage V_{hv}/n is greater than V_{lv} is shown in Fig. 3.13:

- $T_0 - T_1$ (Fig. 3.13(a)): Q1, Q4, Q5 and Q7 are turned on in ZCS at T_0. A positive current flows on the transformer's primary side and series inductance.

- $T_1 - T_2$ (Fig. 3.13(b)): Q7 is turned off in hard-switching while Q8 is turned on in ZVS at T_1. The secondary side V_{hv} is reflected according to the turn ratio to the transformer's primary side.

- $T_2 - T_{s/2}$ (Fig. 3.13(c)): Q1 is turned off in hard-switching and Q2 is turned on in ZVS at T_2. At the zero crossing, $T_{s/2}$, Q5 is turned off and Q6 is turned on in ZCS.

- $T_{s/2} - T_s$: the sequence is performed in analogous way in the subsequent half-period, refer to Fig. 3.12.
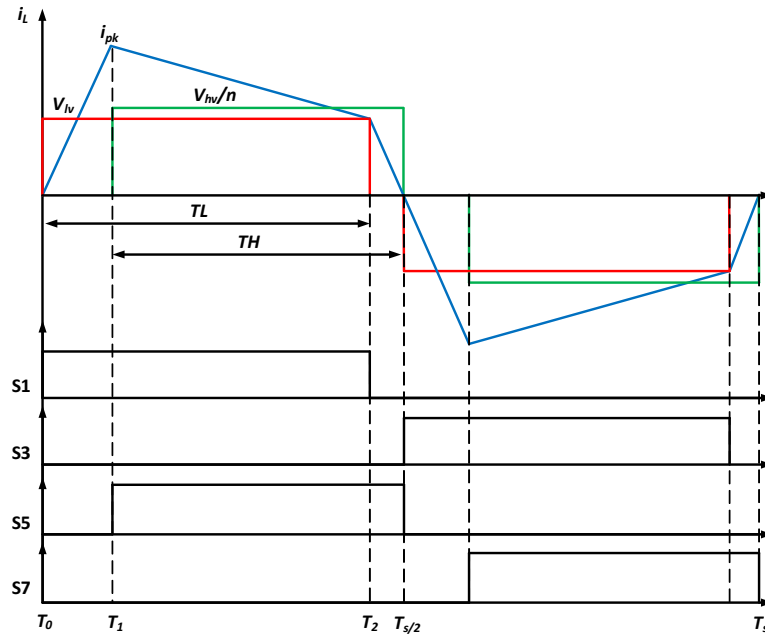
FIGURE 3.12: Trapezoidal modulation sequence in discharging mode
$(V_{lv} < V_{hv}/n)$.
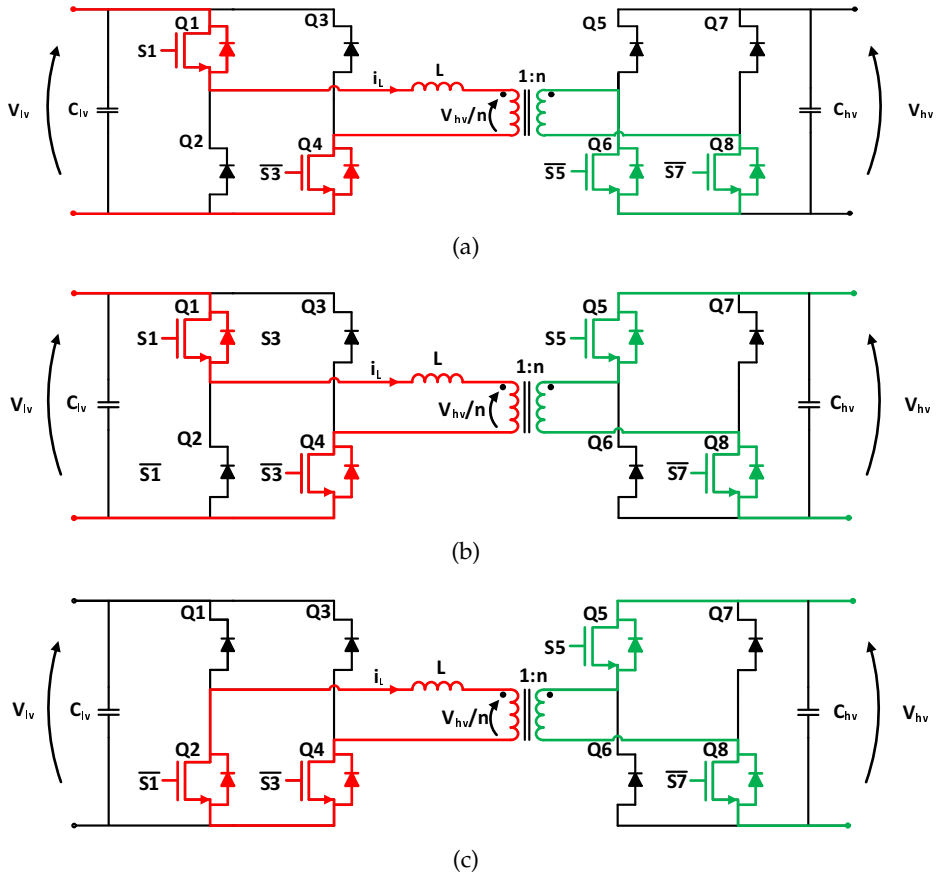
FIGURE 3.13: Commutation half-sequence, battery discharge mode in Trapezoidal modulation with $V_{lv}<V_{hv}/n$: a) T_0-T_1; b) T_1-T_2; c) T_2-$T_{s/2}$.
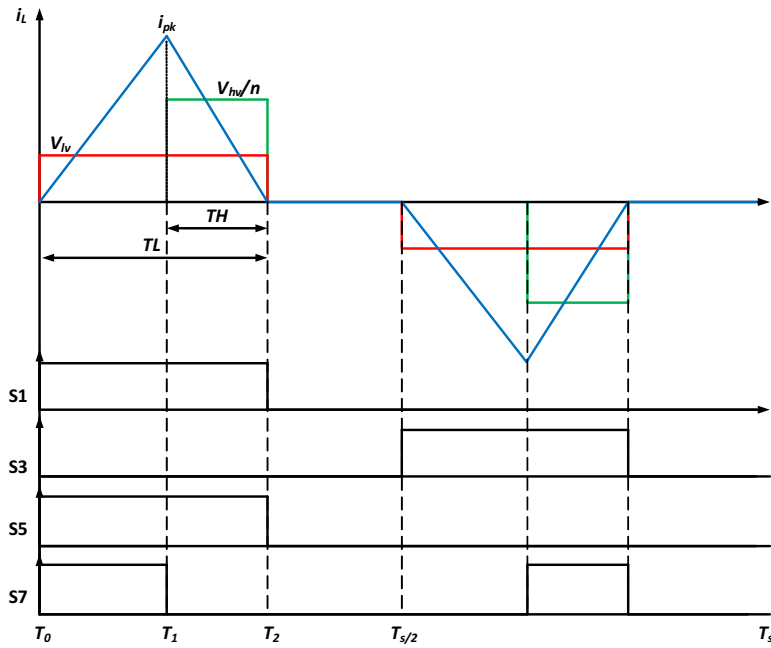
FIGURE 3.14: Triangular modulation sequence discharging mode $(V_{lv}<V_{hv}/n)$.
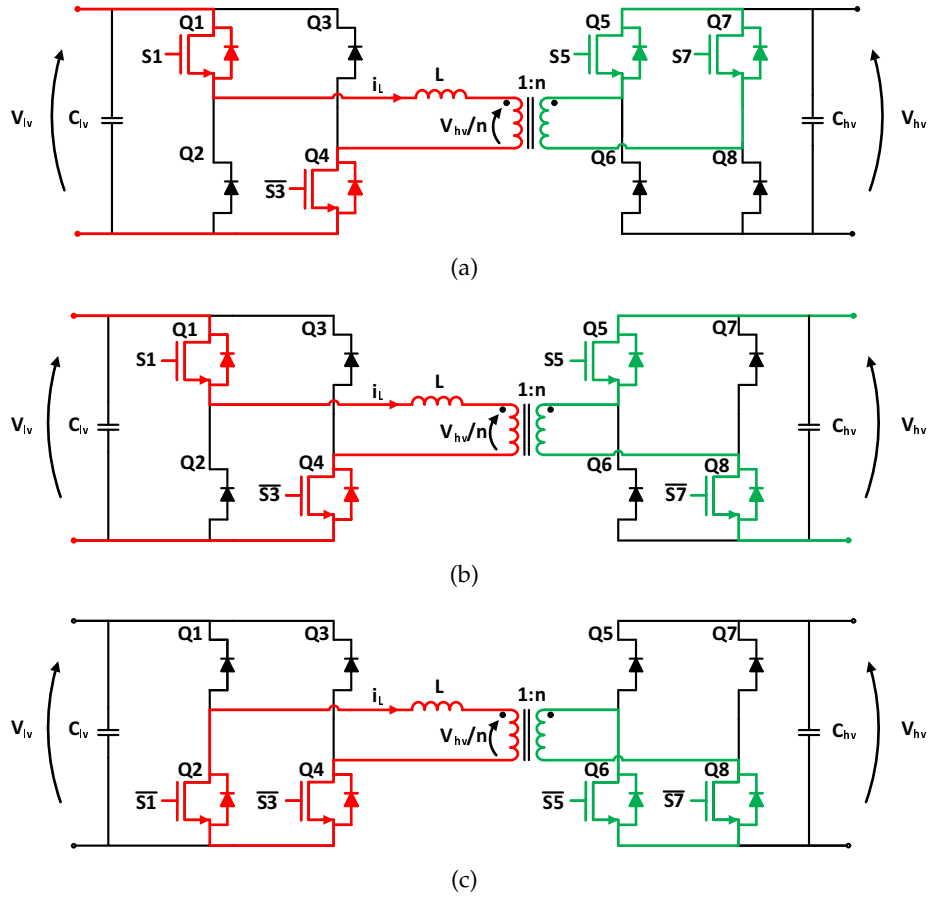
FIGURE 3.15: Commutation half-sequence, battery discharge mode in Triangular modulation with $V_{lv} < V_{hv}/n$: a) T_0-T_1; b) T_1-T_2; c) T_2-$T_{s/2}$.

The commutation sequence of the devices in Triangular modulation when the reflected voltage V_{hv}/n is greater than V_{lv} is shown in Fig. 3.15:

- $T_0 - T_1$ (Fig. 3.15(a)): Q1, Q4, Q5 and Q7 are turned on in ZCS at T_0. A positive current flows on the transformer's primary side and series inductance.

- $T_1 - T_2$ (Fig. 3.15(b)): Q7 is turned off in hard-switching while Q8 is turned on in ZVS at T_1. The secondary side V_{hv} is reflected according to the turn ratio to the low voltage side.

- $T_2 - T_{s/2}$ (Fig. 3.15(c)): Q1 and Q5 are turned off and in ZCS at T_2, while at the same time Q2 and Q6 are turned on in ZCS.

- $T_{s/2}$-T_s: the sequence is performed in analogous way in the subsequent half-period, refer to Fig. 3.14.

In Triangular modulation, according to eq. (3.4), the hard-switching commutation happens only on one device of the leg located on the high voltage or low voltage bridges. In Trapezoidal modulation one device of the high bridge and one of the low bridge experiences a hard-switching commutation, as summarized in Table 3.4.

Adopted Modulation	Number of hard-switching events over T_s	Location of hard-switching when $V_{lv}>V_{hv}/\mathrm{n}$	Location of hard-switching when $V_{lv}<V_{hv}/\mathrm{n}$
Triangular	2	low-side bridge	high-side bridge
Trapezoidal	4	both bridges	both bridges

TABLE 3.4: tabular, compared over one switching period T_s.

Simulations were carried out using the parameters listed in Table 3.5 in Matlab - Simulink environment. The thermal/power loss models of the semiconductor devices were modelled in PLECS. A comparison between conduction and switching losses in discharge mode was carried out over three working points at 50%, 75% and 100% of the rated power. The LV is held constant at the nominal battery value. According to Fig. 3.8 the HV is set to 400V for the Triangular case and to 270V for the Trapezoidal case. Figure 3.16 and Fig. 3.17 show the switching and conduction losses in case of Trapezoidal modulation and in case of Triangular modulation, respectively.

Description	Symbol	Value
Switching frequency	f_s	22kHz
Primary inductance	L	$2,2\mu$H
Turns ratio	n	5
Nominal LV side voltage	V_{lv}	48V
Capacitance LV side	C_{lv}	$54,4$mF
Capacitance HV side	C_{hv}	$2,4$mF
HV side IGBT model	STGW35HF60WD	
LV side MOSFET model	IRFP4468	
LV side diode model	STPS80150CW	

TABLE 3.5: Converter parameters used for simulations.

In Trapezoidal modulation, increasing the processed power from half to full load, the contribution of the switching losses and the conduction losses increase have a proportionality. In Triangular modulation, over the same power interval, the conduction losses increase proportionally, while the number of commutations is lower thanks to the reduced number of hard-switching events. When comparing the conduction losses of Trapezoidal modulation against Triangular modulation, the higher losses in the latter case is due to an increase of the *rms* current value. At the same power level, Triangular modulation experiences higher peak currents, and hence higher the *rms* current value than Trapezoidal modulation.

Following these considerations, the choice of the devices should be based on the modulation scheme adopted for the largest portion of the operating time. In Triangular case the choice should move towards devices with low conduction losses. If Trapezoidal modulation is expected to be dominant, devices with optimized dynamic characteristics can be favoured.
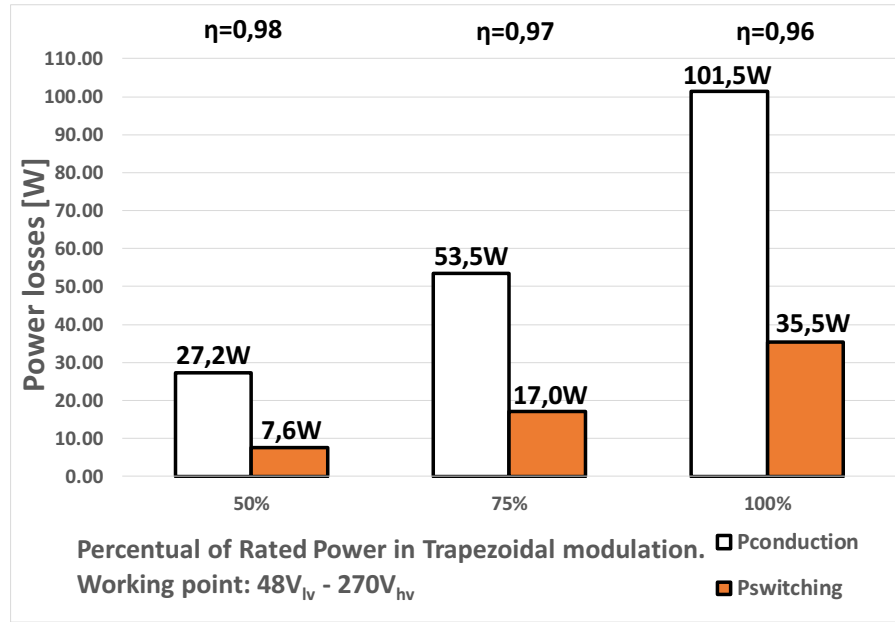
FIGURE 3.16: Semiconductor power losses comparison in Trapezoidal mode at 50%, 75% and 100% of the rated power (3200W).
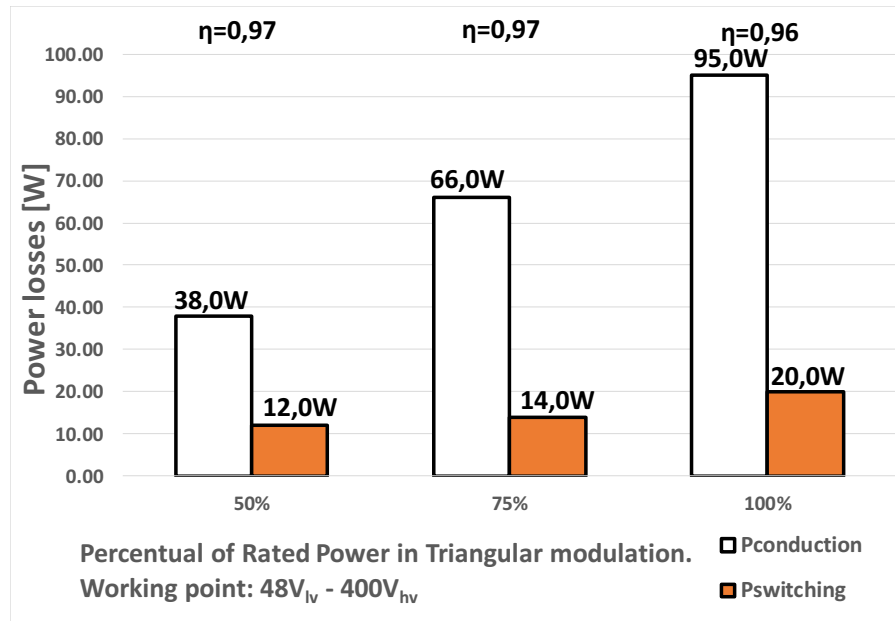
FIGURE 3.17: Semiconductor power losses comparison in Triangular mode at 50%, 75% and 100% of the rated power (3200W).

3.4 Experimental validation

A full size $3,2$kW DAB laboratory prototype was fabricated, Fig. 3.18. The device part number is listed in Table 3.5. The control was implemented on a Texas Instruments 90MHz DSP TMS320F28069. Due to the computational load of the control algorithm, the control is made every two switching period. Two lithium battery pack

48V 50Ah $LiFePO_4$ connected in parallel are used as the storage medium. In charging mode, the high-side bus is linked to a DC voltage supply and in discharge mode, it was connected at a resistive load. Thermal imaging is obtained via TESTO 870-1 camera. The efficiency measurements were taken using an N4L PPA5530 power analyzer.

FIGURE 3.18: Full scale 3,2kW DAB converter prototype (foreground) together with one battery module (background).

Figure 3.19 shows inductor current and gate signals in Trapezoidal mode charging 1,5kW, while Fig. 3.20 shows 2,6kW discharge phase in Triangular modulation.
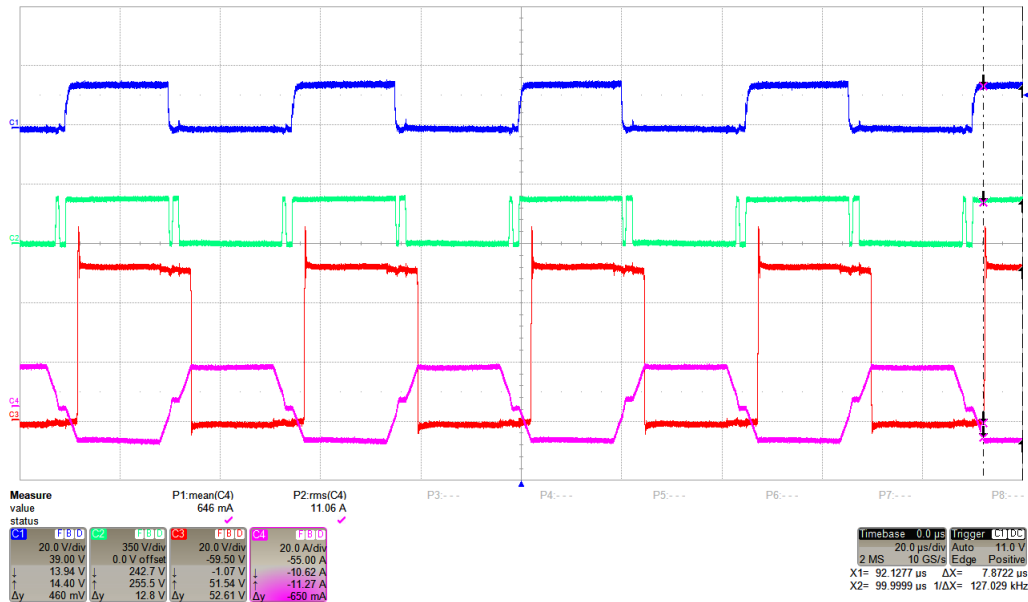
FIGURE 3.19: Charge mode Trapezoidal modulation, 1,5kW $V_{hv} = 270V$, $V_{lv} = 50V$. From upper to lower trace: Q5 V_{GE} (blue, 20V/div), Q6 V_{CE} (green, 350V/div), Q2 V_{DS} (red, 20V/div), secondary current(purple, 20A/div). Time: $20\mu s$/div

Figure 3.21 shows the efficiency obtained in the discharge working point 370V-47V and in the charge working point 370V-51V. The data are plotted with respect to the current transferred to the battery side. Because of the voltage drop on battery interconnecting cables and battery voltage itself, a comparison made on the same power determines different circulating currents. For this reason, in this figure, the power transferred in charge mode results higher with respect to that transferred in discharge mode.
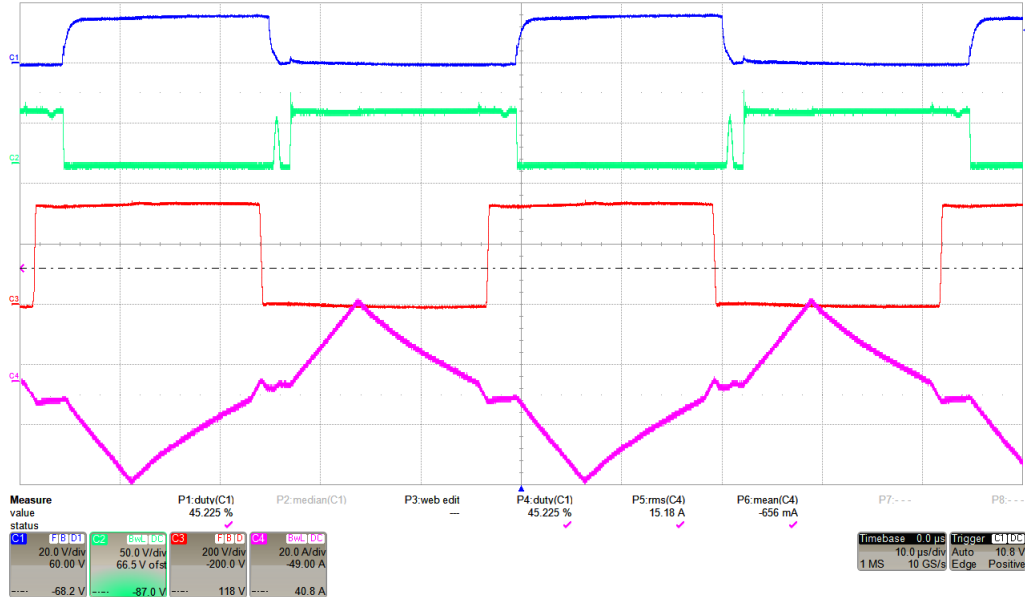
FIGURE 3.20: Discharge mode Triangular modulation, $2,6kW$ $V_{hv} = 325V$, $V_{lv} = 46V$. From upper to lower trace: Q4 V_{GS} (blue,20V/div), Q4 V_{DS}(green, 50V/div), Q7 V_{CE} (red, 200V/div), secondary current, (purple, 20A/div). Time: $20\mu s$/div.
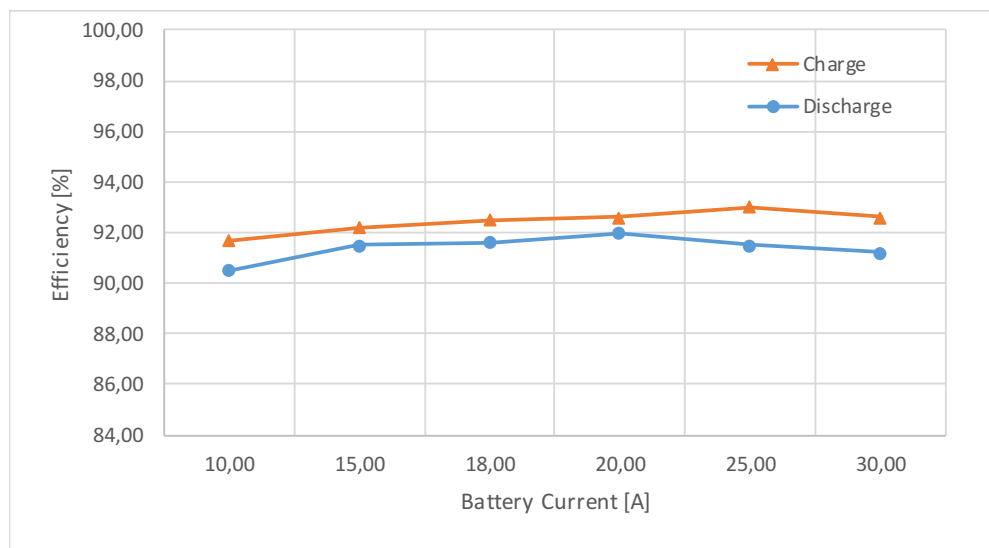
FIGURE 3.21: Measured efficiency: in discharge mode ($V_{hv} = 350V$, $V_{lv} = 47V$) and in charge mode ($V_{hv} = 350V$, $V_{lv} = 51V$).

As described in Section 3.3 the Q1 device experiences a hard-switching commutation while Q4 is turned on in ZCS. Figure 3.22 shows a thermal acquisition (obtained at thermal regime) of the MOSFETs Q1 and Q4 in Trapezoidal modulation, discharging 3, 2kW. Due to the higher losses the temperature of Q1 is greater than the temperature of Q4.
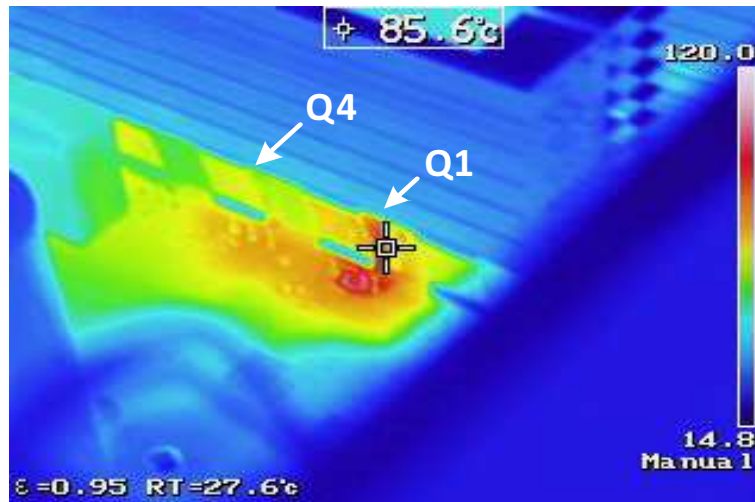
FIGURE 3.22: Thermal image of Q1 and Q4 during a test run at full load (3, 2kW) discharge mode in Trapezoidal modulation.

Figure 3.23 shows the thermal acquisition (obtained at thermal regime) of the same devices, but discharging at full load in Triangular modulation. The MOSFET Q1 is working in ZCS during the modulation sequence and the measured temperature is lower due to the limited switching losses in these conditions.

FIGURE 3.23: Thermal image of Q1 and Q4 during a test run at full load (3, 2kW) discharge mode in Triangular modulation.

3.5 Conclusion

In this chapter, the role of a bidirectional DC-DC power converter for EVs has been described. It can be placed on-board of the vehicle taking part in the propulsion of the vehicle to aid the main energy source or to manage the regenerative braking. The converter can be used as a bidirectional battery charger for the V2G ability, interfacing the vehicle with a green energy plant. The DAB architecture was selected as a galvan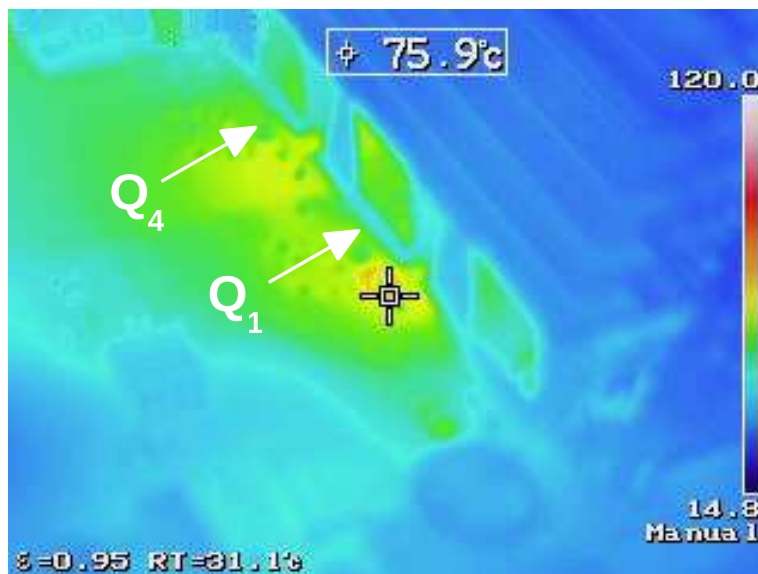ically insulated single-stage DC/DC bidirectional converter. The DAB design and control were developed to match the efficiency requirement and wide voltage capability on both sides. Two advanced modulation sequences were implemented: Trapezoidal and Triangular modulations. The DAB control loop generates the dwell times TH, TL computed in feed forward according to the input-output DC links voltages and the desired transfer power value. An additional block was inserted to compensate the inaccurate knowledge of all the DAB parameters. Semiconductor power losses and hard-switching commutations were investigated for both Trapezoidal and Triangular modulations. Comparison based on thermal/power losses simulation model was carried out. Different criteria to choose the devices can be adopted according to the predominant modulation sequence: in case of Triangular modulation, transistors with low conduction losses are more suitable, while in case of Trapezoidal modulation transistors with optimized dynamic characteristics are preferable. The construction of a full-size 3, 2kW DAB power converter prototype demonstrated the feasibility of the design in terms of overall control strategy, wide voltage range capability, hard-switching commutations and high power conversion efficiency even adopting standard low-cost power semiconductor devices.

Bibliography

[1]   A. Emadi. "Transportation 2.0". In: *IEEE Power and Energy Magazine* 9.4 (July 2011), pp. 18–29. DOI: 10.1109/MPE.2011.941320.

[2]   S. Waffler and J. W. Kolar. "A Novel Low-Loss Modulation Strategy for High-Power Bidirectional Buck - Boost Converters". In: *IEEE Transactions on Power Electronics* 24.6 (June 2009), pp. 1589–1599. DOI: 10.1109/TPEL.2009.2015881.

[3]   S. S. Williamson, A. K. Rathore, and F. Musavi. "Industrial Electronics for Electric Transportation: Current State-of-the-Art and Future Challenges". In: *IEEE Transactions on Industrial Electronics* 62.5 (May 2015), pp. 3021–3032. DOI: 10.1109/TIE.2015.2409052.

[4]   R. M. Schupbach and J. C. Balda. "Comparing DC-DC converters for power management in hybrid electric vehicles". In: *IEEE International Electric Machines and Drives Conference, 2003. IEMDC'03*. Vol. 3. June 2003, 1369–1374 vol.3. DOI: 10.1109/IEMDC.2003.1210630.

[5]   A. Tazay and Z. Miao. "Control of a Three-Phase Hybrid Converter for a PV Charging Station". In: *IEEE Transactions on Energy Conversion* 33.3 (Sept. 2018), pp. 1002–1014. DOI: 10.1109/TEC.2018.2812181.

[6]   M. Brenna, A. Dolara, F. Foiadelli, S. Leva, and M. Longo. "Urban Scale Photovoltaic Charging Stations for Electric Vehicles". In: *IEEE Transactions on Sustainable Energy* 5.4 (Oct. 2014), pp. 1234–1241. DOI: 10.1109/TSTE.2014.2341954.

[7]   P. K. Joseph and E. Devaraj. "Design of hybrid forward boost converter for renewable energy powered electric vehicle charging applications". In: *IET Power Electronics* 12.8 (2019), pp. 2015–2021. DOI: 10.1049/iet-pel.2019.0151.

[8]   S. A. Khan, M. R. Islam, Y. Guo, and J. Zhu. "A New Isolated Multi-Port Converter With Multi-Directional Power Flow Capabilities for Smart Electric Vehicle Charging Stations". In: *IEEE Transactions on Applied Superconductivity* 29.2 (Mar. 2019), pp. 1–4. DOI: 10.1109/TASC.2019.2895526.

[9]   M. A. A. Pedrasa, T. D. Spooner, and I. F. MacGill. "Coordinated Scheduling of Residential Distributed Energy Resources to Optimize Smart Home Energy Services". In: *IEEE Transactions on Smart Grid* 1.2 (Sept. 2010), pp. 134–143. ISSN: 1949-3053.

[10] C. Keerthisinghe, G. Verbič, and A. C. Chapman. "A Fast Technique for Smart Home Management: ADP With Temporal Difference Learning". In: *IEEE Transactions on Smart Grid* 9.4 (July 2018), pp. 3291–3303. ISSN: 1949-3053. DOI: 10.1109/TSG.2016.2629470.

[11] G. Litjens, W. van Sark, and E. Worrell. "On the influence of electricity demand patterns, battery storage and PV system design on PV self-consumption and grid interaction". In: *2016 IEEE 43rd Photovoltaic Specialists Conference (PVSC)*. June 2016, pp. 2021–2024. DOI: 10.1109/PVSC.2016.7749983.

[12]   H. Turker and S. Bacha. "Optimal Minimization of Plug-In Electric Vehicle Charging Cost With Vehicle-to-Home and Vehicle-to-Grid Concepts". In: *IEEE Transactions on Vehicular Technology* 67.11 (Nov. 2018), pp. 10281–10292. DOI: 10.1109/TVT.2018.2867428.

[13]   F. Krismer and J. W. Kolar. "Accurate Small-Signal Model for the Digital Control of an Automotive Bidirectional Dual Active Bridge". In: *IEEE Transactions on Power Electronics* 24.12 (Dec. 2009), pp. 2756–2768. ISSN: 0885-8993. DOI: 10.1109/TPEL.2009.2027904.

[14]   A. Hillers, D. Christen, and J. Biela. "Design of a Highly efficient bidirectional isolated LLC resonant converter". In: *2012 15th International Power Electronics and Motion Control Conference (EPE/PEMC)*. Sept. 2012, DS2b.13-1-DS2b.13–8.

[15]   J. Riedel, D. G. Holmes, B. P. McGrath, and C. Teixeira. "Maintaining Continuous ZVS Operation of a Dual Active Bridge by Reduced Coupling Transformers". In: *IEEE Transactions on Industrial Electronics* 65.12 (Dec. 2018), pp. 9438–9448. ISSN: 0278-0046. DOI: 10.1109/TIE.2018.2815993.

[16]   F. Krismer, J. Biela, and J. W. Kolar. "A comparative evaluation of isolated bidirectional DC/DC converters with wide input and output voltage range". In: *Fourtieth IAS Annual Meeting. Conference Record of the 2005 Industry Applications Conference, 2005.* Vol. 1. Oct. 2005, 599–606 Vol. 1. DOI: 10.1109/IAS.2005.1518368.

[17]   A. Rodríguez, A. Vázquez, D. G. Lamar, M. M. Hernando, and J. Sebastián. "Different Purpose Design Strategies and Techniques to Improve the Performance of a Dual Active Bridge With Phase-Shift Control". In: *IEEE Transactions on Power Electronics* 30.2 (Feb. 2015), pp. 790–804. ISSN: 0885-8993. DOI: 10.1109/TPEL.2014.2309853.

[18]   Florian Krismer. "Modeling and Optimization of Bidirectional Dual Active Bridge DC–DC Converter Topologies". PhD thesis. ETH Zurigh, 2010.

[19]   F. Krismer, S. Round, and J. W. Kolar. "Performance optimization of a high current dual active bridge with a wide operating voltage range". In: *2006 37th IEEE Power Electronics Specialists Conference*. June 2006, pp. 1–7. DOI: 10.1109/pesc.2006.1712096.

[20]   Nikolaus Schibli. "Symmetrical Multilevel Converters With Two Quadrant DC-DC Feeding". PhD thesis. EPFL, Lausanne, 2000.

[21]   R. Fornari, F. Immovilli, and E. Lorenzani. "Wide Voltage Range Dual Active Bridge PV Retrofit Storage System". In: *IECON 2019 - 45th Annual Conference of the IEEE Industrial Electronics Society*. Vol. 1. Oct. 2019, pp. 2524–2531. DOI: 10.1109/IECON.2019.8926933.

Chapter 4

Enhanced flux-weakening strategies for traction applications

4.1 Introduction to electric power train applications

This chapter deals with the optimization of the control strategy of Internal Permanent-Magnet Synchronous Motor IPMSM for light vehicle application. In particular, this work proposes different control strategies to address the critical issue of fast torque transition, presenting different modified flux-weakening strategies based on outer voltage loop or i_d current error. The proposed modified control strategies are experimentally validated with extensive test campaign on a dedicated test bed.

Internal permanent magnet machine is one of the most common typologies employed in the design of power train for electric transportation. It shows: high torque density, high efficiency (due to the absence of the magnetizing current and rotor circuit) and high flux-weakening capability [1]. In power train application flux-weakening control strategy is a critical point because electrical machines operate in a wide speed range above the constant torque region. The flux-weakening definition is due to the fact that the stator magnetic field is used to weaken the permanent-magnet flux linked with the stator coil. This aim is achieved by increasing the negative d-axis current component until the characteristic current of the machine matches the outer limit of the current circle for an ideal infinite speed range. Many papers deal with the optimal magnetic flux quantity to obtain an optimal machine behaviour, that can be substantially synthesized in a machine design that force the characteristic current on the edge of the current limit circle in the i_d-i_q plane, thus avoiding Maximum Torque Per Voltage (MTPV) region to obtain the maximum exploitation of the power train. For electric vehicle application this simple statement must fulfil different duty types with corresponding different current limits, therefore a tradeoff has to be found. In this chapter the characteristic current is designed to be in the middle of two current limits corresponding to the continuous duty type (S1) and the short-time duty (S2). According to this design approach a large volume of rare earth permanent-magnets must be employed achieving high machine performance and efficiency, but also high permanent magnet linkage flux. With this design approach, during flux-weakening operation at high speed it is necessary to counteract the magnet Back-EMF with an appropriate d-axis magneto-motive force, in particular a high negative d-axis current has to be fed even if the torque set point is quite low or at least equal to zero.

Different flux-weakening control strategies have been developed in the last years as shown in [2], [3], nevertheless even if this control strategies are strongly proven in motor operation, few studies and examples of what happens during fast transitions

of the torque set point and the external load at high speed have been deeply investigated. The control strategy for an electrical vehicle is usually based only on a torque control loop and the driver adjusts the vehicle speed acting on the throttle (torque control). During brake or other fast torque transitions, the torque set point could be moved from its maximum value to zero and, if the motor is in the flux-weakening region, the motor should move its working point either in generating region or in a zero-torque condition. During the transition of torque set point, the current angle error due to iron losses changes its sign [4] making difficult to manage the energy-flow transition from the motor to the battery to avoid battery unsafe operation or overcharge. Moreover, the vehicle behaviour could be heavily affected by the braking torque generated by the motor, especially for motorcycles also a short time braking torque could cause driver injuries. The author of [4] proposes a flux-weakening control algorithm based on the increase of the i_d current error, once the voltage limit is reached. This i_d error is used to decrease the v_q axis voltage set point. The control scheme is substantially a modification of the classical feed forward vector control method. This solution allows a smooth transition from Maximum Torque Per Ampere (MTPA) to flux-weakening control strategies and fast response. In addition, this method does not strongly rely on the motor parameter and LUT of the magnetic model.

Other control approaches [5] implement the flux-weakening strategy employing the outer voltage loop to generate an appropriate i_d current to keep the voltage vector within the range limits imposed by the Voltage DC-bus. The control scheme is aimed to the voltage maximum exploitation, also in this case no specific strategy is deeply investigated to manage the fast torque transition. In paper [6], an enhanced control strategy for high speed permanent-magnet synchronous machines is proposed for electric vehicle application. This control strategy operates from low up to high speeds region employing the same approach of the outer voltage loop adding some additional block with also the MTPV equations. Even in this case fast torque transition issue is not pointed out and no tests on a real vehicle are presented. Other similar control strategies are presented in [7],[8],[9].

The work presented in this chapter shows a modified flux-weakening control strategy to appropriately manage fast torque transitions and/or braking torque issue. Two control schemes are presented: the first based on the outer voltage loop and the second on [4] solution. Experimental results of the two control strategies are presented in this treatment. At the beginning recalls of theoretical permanent-magnet synchronous motor control equations and control strategies will be given. In the following, the main critical issues of common flux-weakening strategies will be investigated through experimental tests. In the end, the results of improved control methods will be shown comparing the operating region profiles of the improved methods obtained by test bench experimental.

4.2 PM vector control equations

According to d-q rotor reference frame, where the d-axis corresponds to the North Permanent-Magnet (PM) magnetic axis, the steady-state voltage equations of permanent-magnet synchronous motor PMSM are expressed as follows:

$$\begin{aligned} v_d &= R_s i_d - \omega_e L_q i_q \\ v_q &= R_s i_q + \omega_e \Lambda_{PM} + \omega_e L_d i_d \end{aligned} \tag{4.1}$$

where i_d, i_q, v_d, v_q are d- and q-axis components of stator currents and motor terminal voltages, Λ_{PM} is the PM flux, R_s is the stator resistance, L_d and L_q are d- and q-axis self-inductances. If the motor has no saliency the self-inductances are equals. The terms $-\omega_e L_q i_q$ and $+\omega_e L_d i_d$ in the eq. 4.1 are the motional terms which couples d-q axis components and as a consequence, the d- and q-axis cannot be controlled independently by V_d and V_q voltages [10]. Further, Internal PMSMs have large inductances making dominant cross-coupling effects that increase as the speed increases. As a consequence, the current response, as well as the torque response, are affected by the motional terms in the high-speed region. These two contributions could be compensated in the control strategy by feed forward terms in order to linearize the current loops. In the following proposed control schemes, the d-q voltages are determined by current loop PI controller outputs feed forward compensated.
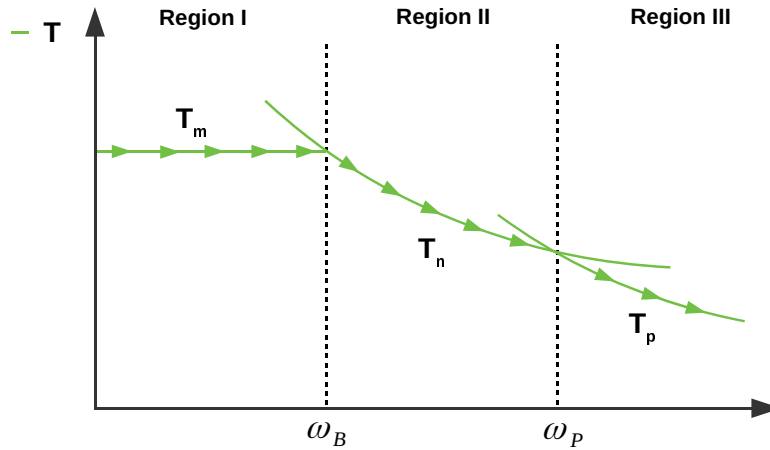

FIGURE 4.1: Electrical machine operating regions and torque curves.

The torque equation of PM motor is expressed in eq. 4.2 [10]:

$$T = \frac{3}{2} p [\Lambda_{PM} i_q + (L_q - L_d) i_d i_q] \tag{4.2}$$

where p is the pole pair number. The Fig. 4.1 shows the machine operating regions:

- Region I: is the constant torque (MTPA) region where the motor accelerates until ω_B speed. The objective of MTPA is to maximize the torque to current ratio (that corresponds to the minimization of the Joule losses). The B point corresponds to the current limit circle given by the eq.4.3:

$$i_d^2 + i_q^2 = i_{Lim}^2 \tag{4.3}$$

where the current value i_{lim} depends on the inverter kVA rating and is obtained applying the maximum available voltage, that in this case corresponds to the battery voltage state. On i_d-i_q plane the voltage limit circle in the plane becomes an ellipse, see eq. 4.4 and eq. 4.5 where ω_m is rotor mechanical speed.

$$v_d^2 + v_q^2 = v_{Lim}^2 \tag{4.4}$$

$$L_d^2\left(i_{Lim} + \frac{\Lambda_{PM}}{L_d}\right)^2 + L_q^2 i_q^2 = \left(\frac{v_{Lim}}{p\omega_m}\right)^2 \tag{4.5}$$

Figure 4.2 shows these critical constraints on d-q plane and the iso-torque curves.

FIGURE 4.2: Current, voltage limits and iso-torque curves on d-q plane.

- Region II: starting from point B of Fig. 4.2, to increase the velocity with the same torque (point D) a higher current should be applied to the stator winding exceeding the current limit. To extend the operation to higher speed the trajectory is moved on the current limit circle circumference decreasing the torque at the rotor shaft. In this condition, called *flux-weakening* (FW), the constant maximum available voltage is applied and the d-component current is increased to contrast the permanent magnet flux Λ_{PM}. This condition can be identified with the maximum power operation, due to the maximum current and voltage limits are applied.

- Region III: for a given machine, the voltage ellipse depends on machine mechanical speed, in particular the ellipse axes shrink as the mechanical speed increases. The centre of the voltage ellipse is expressed as follows:

$$i_{ch} = -\frac{\Lambda_{PM}}{L_d} \tag{4.6}$$

The value given by eq. 4.6 is strictly dependent on machine parameters and operating point, due to cross saturation effects [11]. Two cases are possible: the centre of the voltage ellipse falls inside of the current limit circle or is outside. Figure 4.3 and Fig. 4.4 show respectively the case when $i_{ch} < i_{lim}$ and $i_{ch} > i_{lim}$

on d-q plane. In the first case the speed range can be extended above the ω_P speed adopting the MTPV strategy to maximize the torque to voltage ratio [12], meaning that in this region the torque is maximized for any flux as well [13].
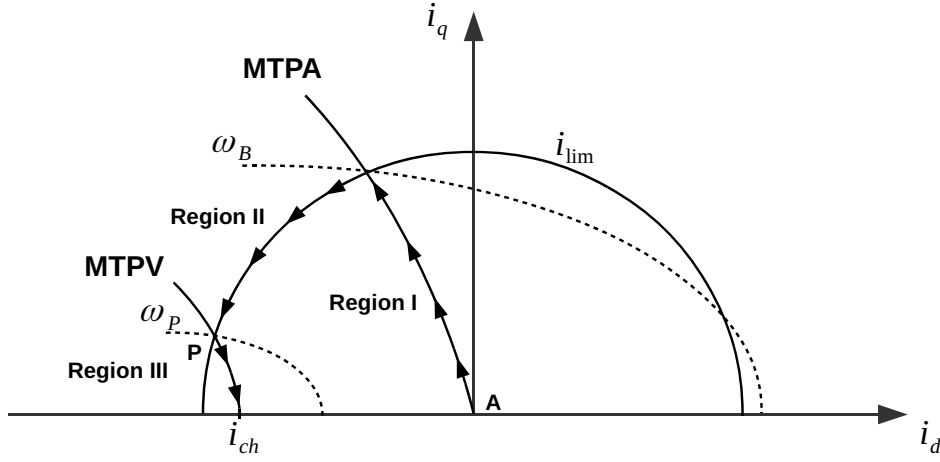

FIGURE 4.3: Optimum current trajectory on d-q plane for $i_{ch} < i_{lim}$.
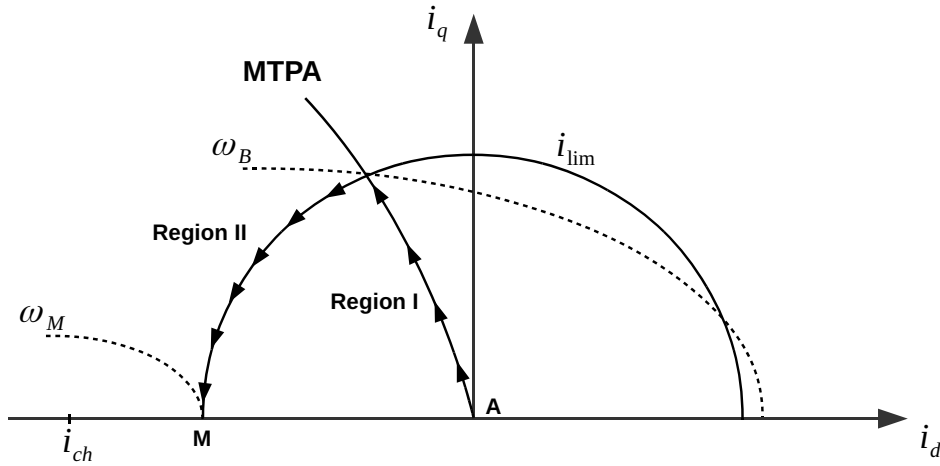

FIGURE 4.4: Optimum current trajectory on d-q plane for $i_{ch} > i_{lim}$.

Referring to Fig. 4.1 different torque curve are applied in any region. The T_m is the peak constant torque at which the motor can be accelerated until ω_B speed with MTPA strategy. T_n and T_p are the torque profiles that can be obtained respectively [10]: at maximum current (on the current limit circle circumference) and optimizing the torque for any flux. The rotor speed ω_p is the value of speed at which the MTPV strategy is suitably adopted. The electrical operating regions become as in Fig. 4.5(a) when MTPV is adopted, with theoretically no speed limit.

The aim of the IPMSM control of this work is to set the machine electrical inputs to obtain a certain torque at a given mechanical speed enhancing power train performance. In so doing an optimized control strategy has to be adopted to determine the optimum current vector to exploit the maximum torque profiles in all speed range: in Region I with the MTPA strategy and in Region II where the motor is controlled according to flux-weakening strategy and the permanent magnetic flux Λ_{PM} is contrasted to increase the speed.
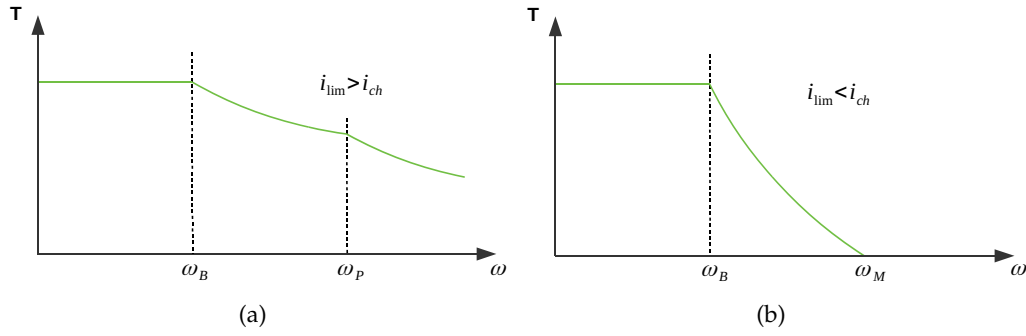
FIGURE 4.5: Electrical machine operating regions: a) with MTPV
when $i_{ch} < i_{lim}$; b) without MTPV when $i_{ch} > i_{lim}$.

4.3 Flux-weakening behaviour in traction application

During the vehicle operating conditions, the driver controls the torque reference by means of the throttle. Thus, during acceleration, the ideal behaviour depends linearly to the torque set point. This correlation is fundamentally true in MTPA region, while in FW the torque decreases as the speed increases with a constant current vector amplitude. Therefore, a robust control strategy should approximate this behaviour and guarantee full exploitation of the FW region. Flux-weakening, in traction applications, permits to achieve an extended constant power range eliminating the need for mechanical gear ratio and avoiding the volt-ampere oversizing of the power converter. To implement Field Weakening of IPM motor it is necessary to generate a suitable negative i_d setpoint. As a matter of fact, a negative i_d current will produce a flux along the d-axis opposing the rated flux generated by Permanent Magnets. The strategy adopted to determine the i_d setpoint affects the motor performance and it must be designed taking into account on one side the torque generation and on the other the voltage and current limitations. As is well known an early Field Weakening strategy can reduce the generated torque deteriorating acceleration performance if too strong action is made. On the contrary, a late start or a weak action may result in undesired torque drop according to the current regulator saturation. This states the importance of changing the onset point of flux-weakening according to the operating point and machine parameters.

Since the onset point and the level of flux-weakening depend on load, motor parameters and battery state of charge, the generation of the ideal weakening trajectory and, in turn, of the relative i_d setpoint is a complicated task. From a theoretical point of view, the i_d and i_q setpoints could be computed starting from the torque command and the desired flux magnitude. With this approach, known as *feed forward* technique, it's almost impossible to obtain the maximum possible torque vs. speed due to parameters change during motor operation. Voltage battery variation, magnetic saturation, resistive voltage drop can affect the final result. In [7] an effective feed forward flux-weakening control algorithm, based on motor equations, is proposed. Assuming I_s the maximum inverter current and V_{BUS} the measured bus voltage, from equations 4.3 and 4.5 it is possible to obtain currents command i_{d_safe},

i_{q_max} in function of motor parameters, electrical speed $\omega_e = p\omega_m$ and bus voltage:

$$
\begin{cases}
i_{d\_safe} = \dfrac{-\Lambda_{PM}L_d + \sqrt{\Lambda_{PM}^2 L_d^2 - \left(L_d^2 - L_q^2\right)\left(L_q^2 I_{max}^2 + \Lambda_{PM}^2 - \dfrac{v_{BUS}^2}{\omega_e^2}\right)}}{\left(L_d^2 - L_q^2\right)} \\[4mm]
i_{q\_max} = \sqrt{I_s^2 - i_d^2}
\end{cases}
\tag{4.7}
$$

Figure 4.6 reports the results obtained by the feed forward technique generation of i_d command. The first set (red solid lines) is obtained using the rated motor parameters and the actual Battery voltage. The second one (blue solid lines) refers to a situation in which the bus voltage is underestimated of about 5%. As it is clearly visible in the latter case the torque and the power obtained in flux-weakening conditions are lower than the previous one. It could be helpful to recall that in both cases the results are away from those obtained in an ideal situation being the mechanical power far from constant in flux-weakening region. In summary, some closed-loop correction is necessary to fully exploit the power limit of IPM motors.
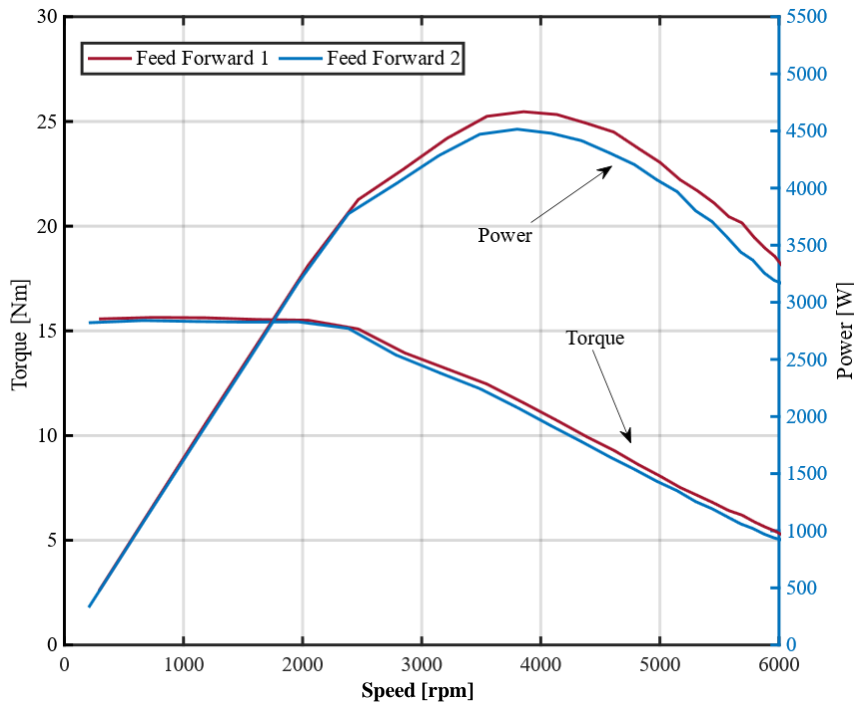

FIGURE 4.6: Drive performance with feed forward strategy with two different battery charge levels. Red line with the correct battery voltage and blue line with underestimated bus voltage of 5%.

In literature methods based on saturation of current regulators detection or on voltage saturation detection have been proposed by researchers. Among them, in this chapter are investigated the scheme proposed in [5], [14] and in [4] because of their simplicity and effectiveness. Fig. 4.7 reports the scheme proposed in [5]. In the MTPA operations the torque command is converted into the corresponding values of d-q axis current commands $i_{a,sp}$ by function blocks f1 and f2 and then the polar to rectangular conversion block ($i_{d,sp}^*$ and $i_{q,sp}$). The flux-weakening control module executes the current angle reduction by a PI regulator which input is the voltage saturation error obtained by comparing the requested voltage with the available battery voltage that depends on the state of charge.
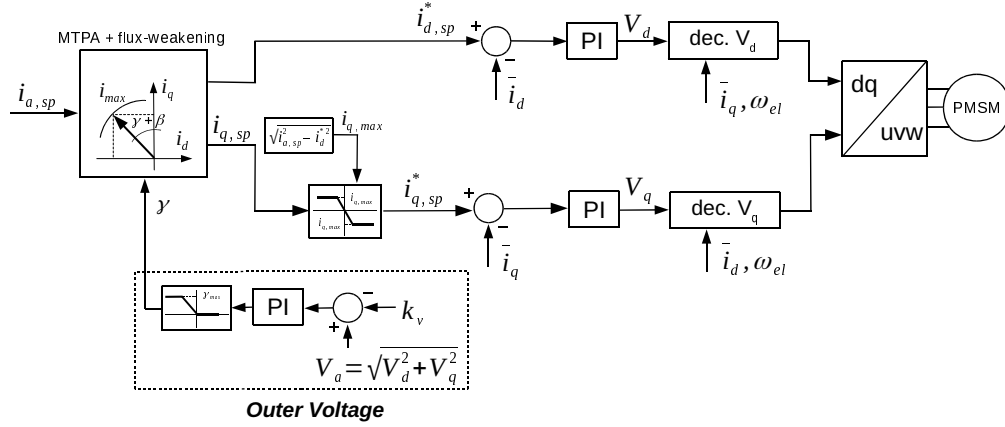
FIGURE 4.7: Outer voltage scheme proposed in [5].

Figure 4.8 reports the scheme proposed in [4]. In this solution MTPA operation is very similar, the flux-weakening control is realized using the i_d error (Δi_d) between the d-axis current command $i_{d,sp}^*$ and the resultant value $\bar{i}_d$ which provides valuable detection feedback. In presence of a growing d-axis current error Δi_d, the q-axis current command $i_{q,sp}$ will be decreased. By so doing the command current vector is forced back down inside the ellipse instead of lying outside the voltage limit ellipse at a given speed. Both methods look good to exploit the potential of the IPM electrical machine in flux-weakening, almost in acceleration. Since under both schemes rely on an integral action that drives the limits of the currents command, some issues could arise in deceleration depending on the integral dynamic. With the aim to test their performance in acceleration and in deceleration as well, a suitable test bed was implemented (see section 4.5).
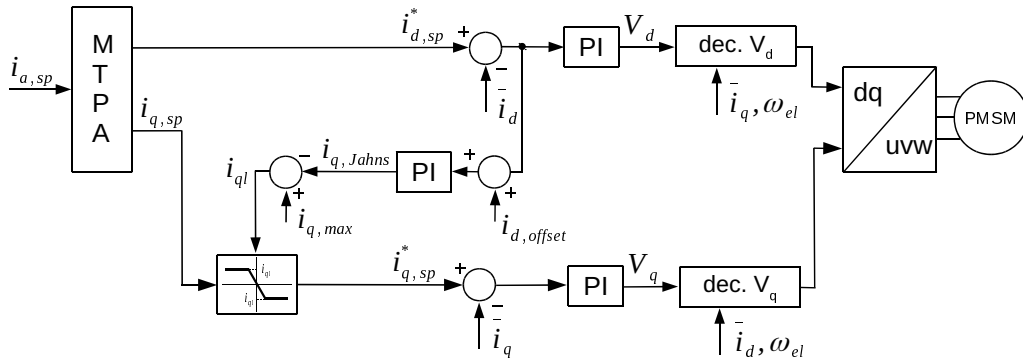

FIGURE 4.8: Control scheme proposed by "Jahns" in [4].

Figure 4.9(a) and 4.9(b) show the performance in acceleration and deceleration of the flux-wakening strategy of both outer voltage method and Jahns method during experimental tests. As previously discussed, the flux-weakening angle or d-q current components are computed relying on an integrator. As it can be expected they perform quite good in acceleration, but present a big issue when the torque command goes abruptly to zero at high speed due to an external mechanical braking action.

In Fig 4.10(a) and 4.10(b) it can be appreciated that the angle computed by the integrator (orange solid line) when torque command goes to zero, approaches the value computed for the MTPA region. This is due to the fact that in the braking condition the voltage error in the outer loop method changes sign and the integral

value reduces it to its minimum angle value (about 18°). Something similar happens in Jahns method as well.
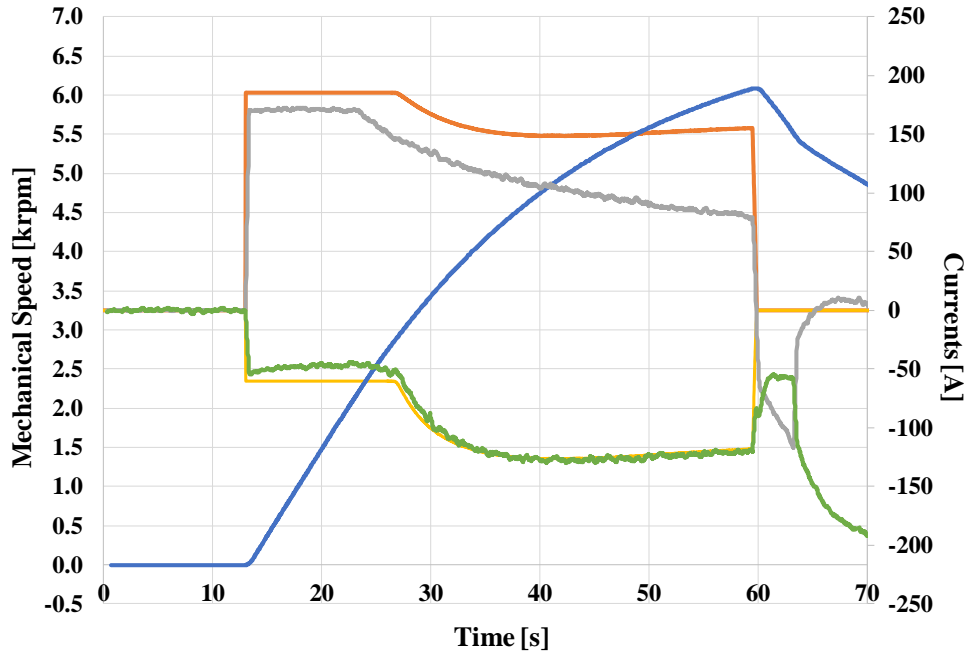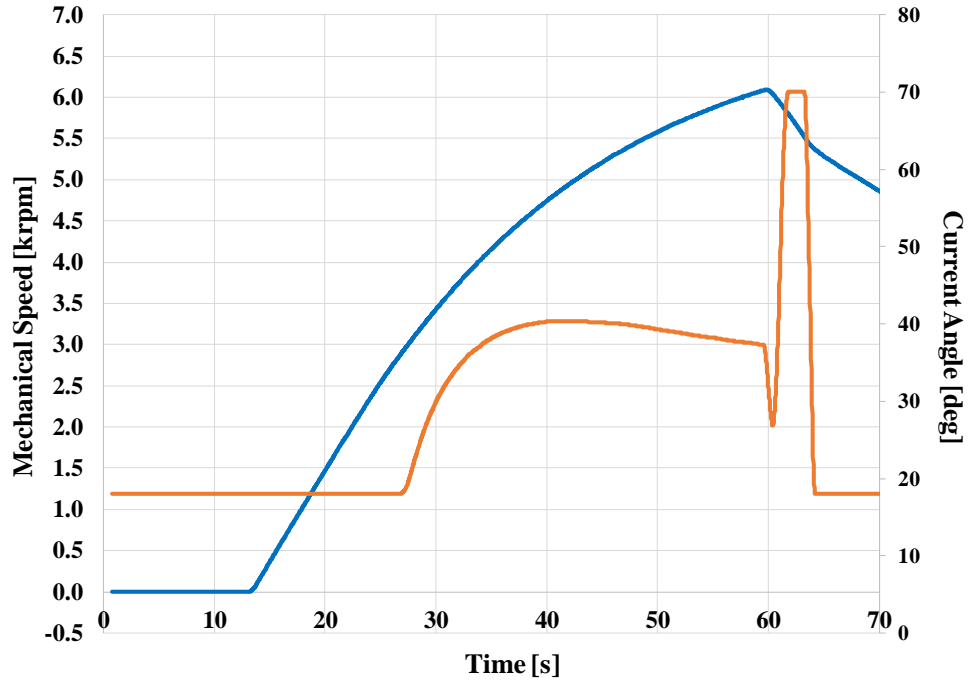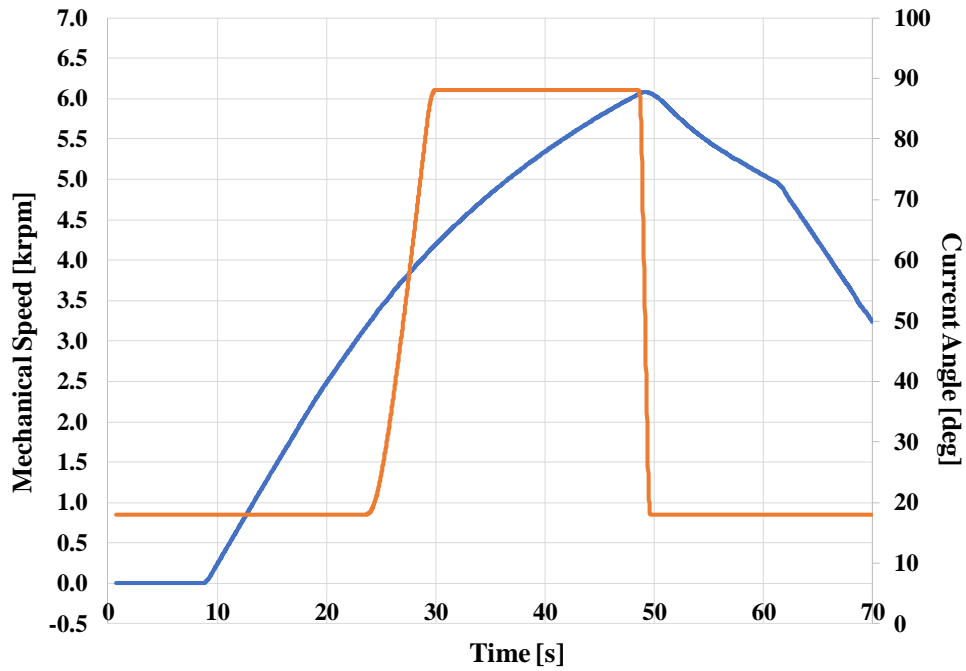

(a)
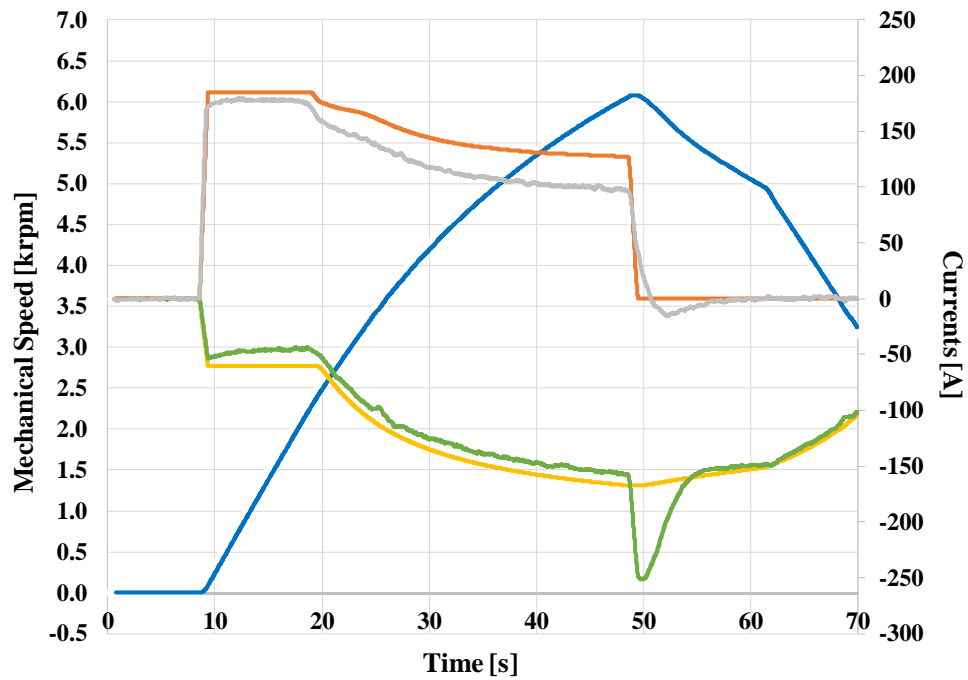
(b)

FIGURE 4.9: Speed profile (blue solid line) and d-q currents signals: i_d set point (yellow solid line), motor i_d (green solid line), i_q set point (orange solid line) and motor i_q (grey solid line). a) Outer voltage control and b) Jahns control.

(a)

(b)

FIGURE 4.10: a) Outer voltage current angle (orange solid line) and
b) Jahns current angle (orange solid line).

Obviously, since i_d setpoint should depend on speed and voltage only, the sudden change of the outer voltage error generates a wrong i_d^* command, i.e. the i_d^* command suitable for MTPA region. This, in turn, generates an error in current control giving rise to voltage error or i_d error again. Moreover, it produces an uncontrolled active braking torque and an uncontrolled generation, with consequent uncontrolled current flow in the battery pack. Eventually, also the braking feeling

perceived by the driver will be uncomfortable being the initial braking phase uncontrolled and, in a condition of wet road, it can be harmfully. In Fig. 4.9(a) the different slope of the speed profile during the braking phase in case of outer voltage method can be appreciated. Jahns method (Fig. 4.9(b)) results are quite similar.

4.4 Optimized control strategy for flux-weakening operation

To improve the performance of both methods, a feed forward action based on the current command of formula 4.7 was introduced to overcome the issue related to the current angle computation [15]. In so doing a good estimation of the d-axis current can be computed and adopted by the control strategy during braking in flux-weakening region. During braking phase in flux-weakening region, if the i_d^* command computed using the integral approach is lower than the i_{d_safe} command resulting from 4.7 the latter will be taken as i_d^* current setpoint. Thus, the motor performance is preserved during the braking phase at high speed. This is the reason why we named this contribution "*id-safe*".
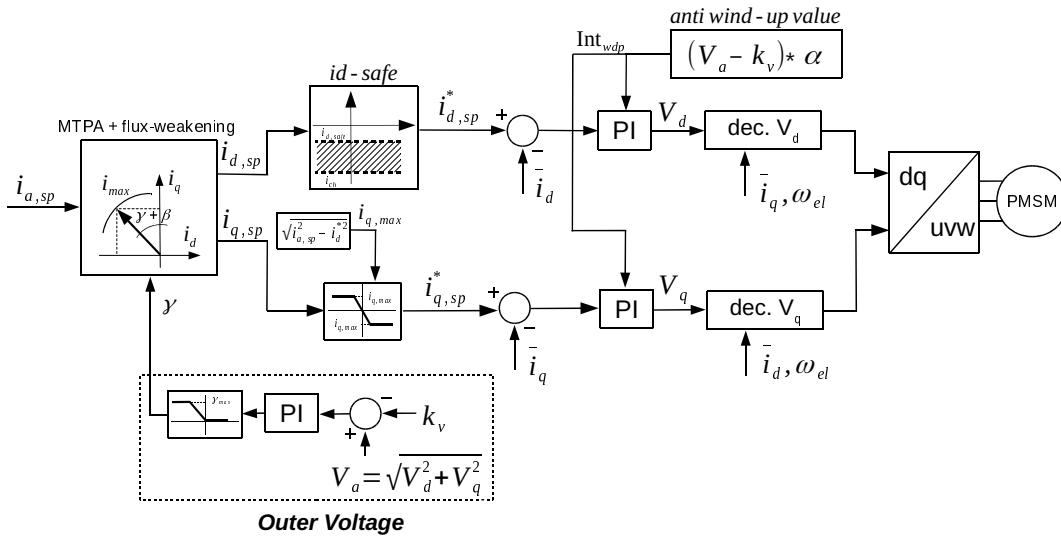

FIGURE 4.11: Outer Voltage method improved by the Id-safe strategy.

Fig. 4.11 reports the experimental result of the Outer Voltage method improved by the "*id-safe*" strategy, while Fig. 10 shows the corresponding results during acceleration/deceleration from zero up to $6000rpm$ and back. During the braking phase the current angle is by-passed by the "*id-safe*" values, as it can be seen the annoying effect on the speed at the early braking stage is properly compensated and the performance repetitiveness was guaranteed.
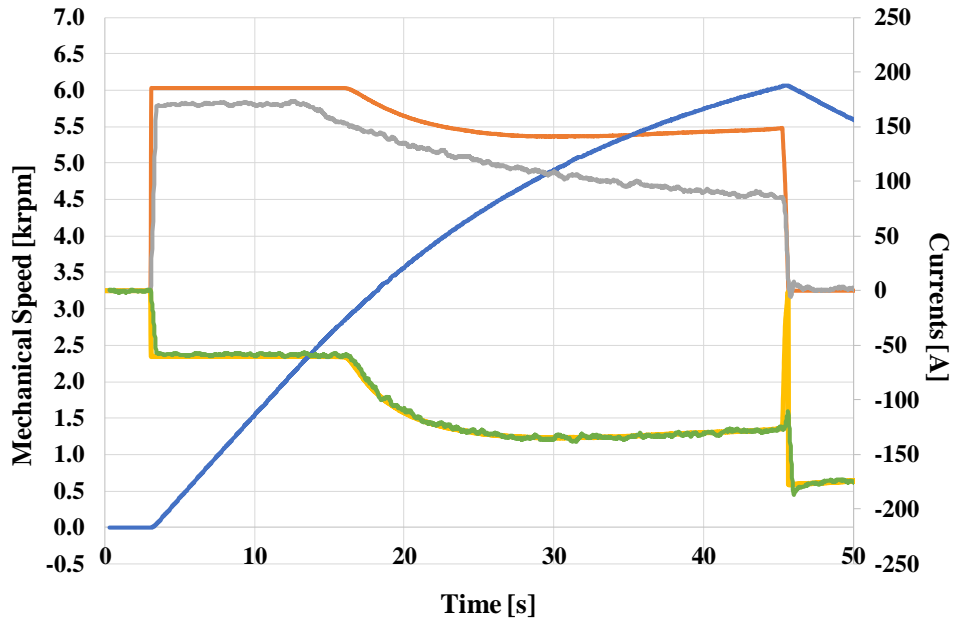
(a)
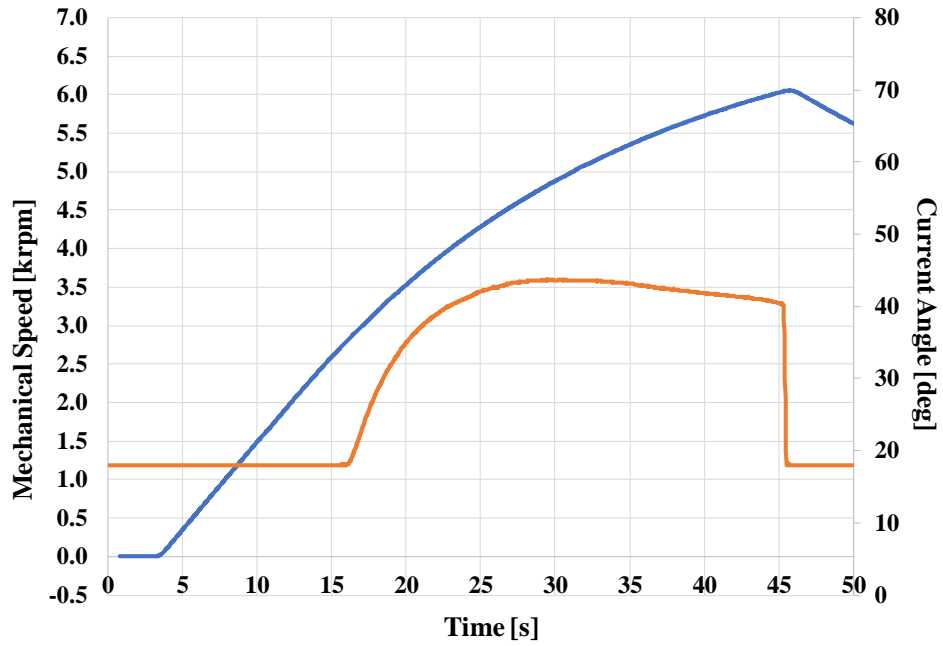
(b)

FIGURE 4.12: Improved Outer Voltage method results; a) speed profile and i_d-i_q currents signals and b) current phase angle (orange solid line). .

The same feed forward action was introduced in Jahns control scheme. Fig. 4.13 shows the resulting control scheme while Fig. 4.14 reports the behaviour during acceleration/deceleration from zero up to $6000rpm$ and back. The current angle profile is similar to that shown in Fig. 4.10.
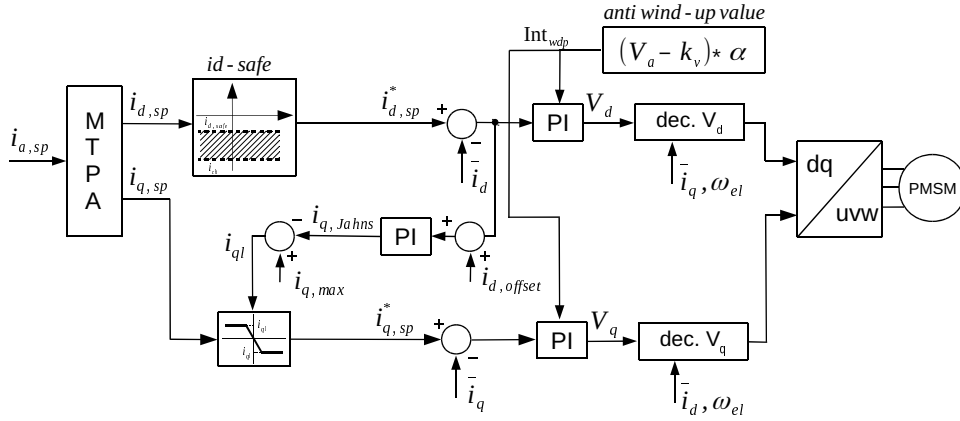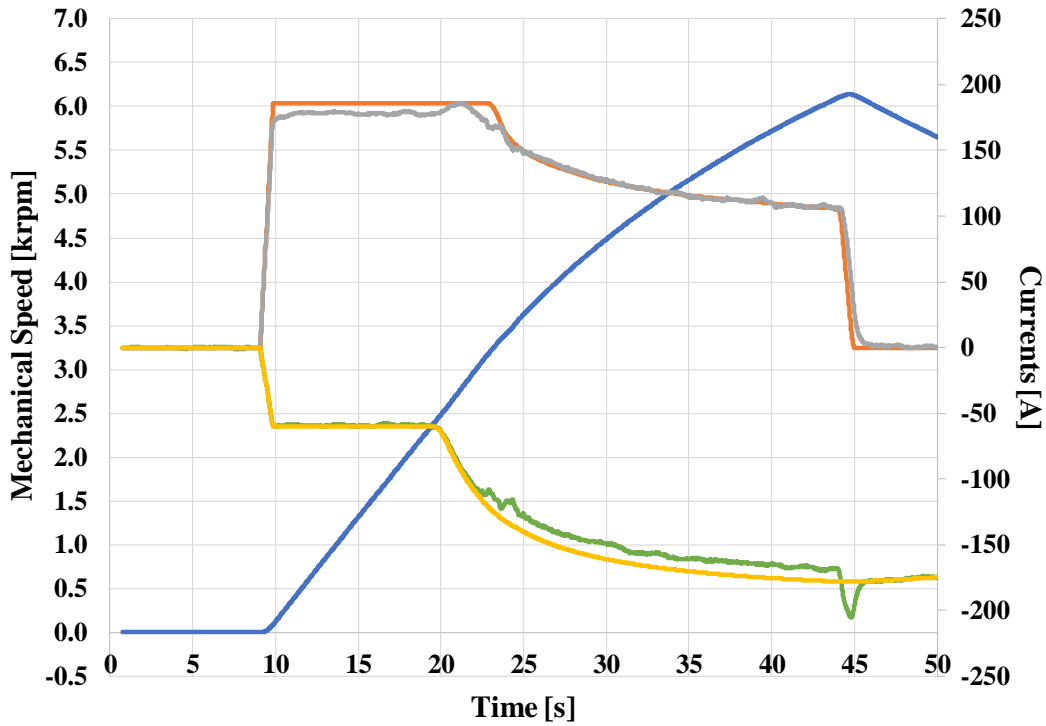
FIGURE 4.13: Improved Jahns control scheme.

Also, in this case, the braking action performs good showing controllability and repetitiveness. A particular anti-windup approach has been introduced with the aim to increase further the performance in the flux-weakening region, while keeping the voltage request on the edge of the saturation. In particular, the error between the requested voltage and the voltage at disposal is multiplied by a suitable gain α and then it is summed to the integral action of both d-q axis current PI regulators. In so doing, no deep saturation of current PI regulators can arise due to the lack of voltage. The dynamic performance of the system increases since current PI regulators are forced to ask, more or less, what the system can realize in term of voltage. This solution must be applied with great care in case of outer voltage since this method relies on voltage saturation for current angle computation.

FIGURE 4.14: Improved Jahns control scheme results; speed profile and i_d-i_q currents signals.

4.5   Experimental results

The proposed control strategies have been validated on an active test bench. The rig is composed as follows:

- 12 slots 10 poles IPM Motor under test;

- Three-phase high current drive;

- Power analyser;

- Torque meter;

- 48V lead battery pack;

- Active brake 45kW, 500N m.

Parameter	Symbol	Value	Measure Unit
Nominal Current	I_n	68, 5	A_{rms}
Nominal Load Torque	T_n	8, 5	N m
Nominal Mechanical Speed	ω_m	4500	rpm
Number of Slots	Q	12	-
Pole pairs	p	5	-
Nominal Supply Voltage	V_n	48	V_{rms}
Permanent-Magnet Flux	Λ_{PM}	13, 2	mWb
Overload Current	I_{ov}	335	A_{rms}
Overload Torque	T_{ov}	34, 5	N m
Torque Constant	kt	0, 13	V_{rms}/A_{rms}
Lamination Stack Length	L_{stk}	120	mm
Slot Conductors (=2*NO. coils)	n_c	10	-
Copper Wire Section	S_w	7, 6	mm^2
Wire Length	L_w	5, 9	m
Phase-to-Phase Resistance	R_{ph-ph}	3, 3	$m\Omega$
Phase-to-Phase Inductance	L_{ph-ph}	0, 22	mH
Short Duty Time	$S2$	30	min

TABLE 4.1: IPM Drive Motor Characteristics

Table 4.1 reports IPM motor characteristics used to shows experimental results shown in sections 4.3 and 4.4. The test bench is shown in Fig. 4.15
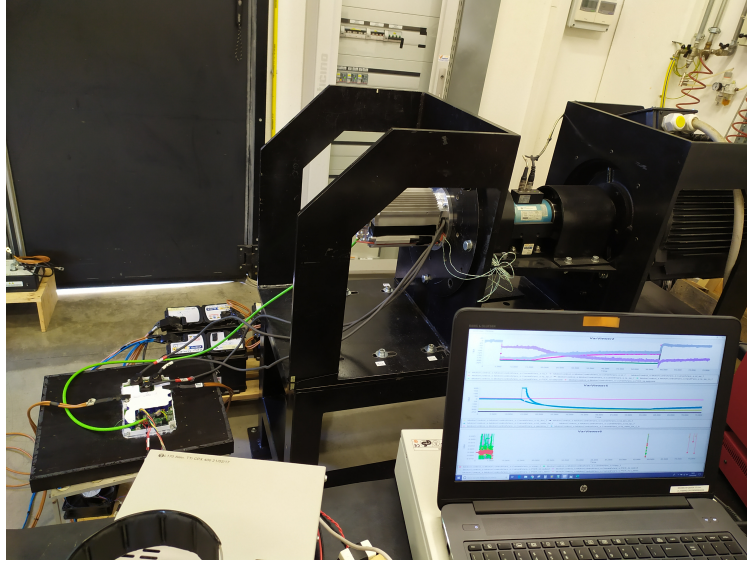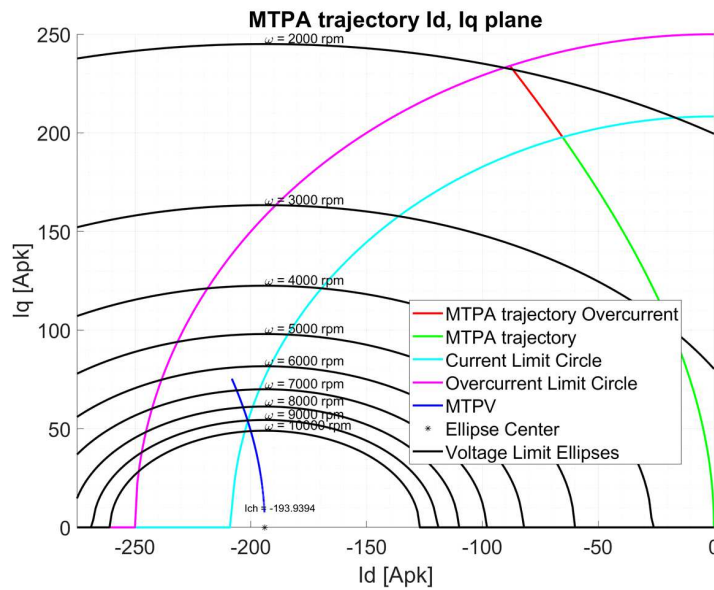
FIGURE 4.15: Test bench set up.

Figure 4.16 shows the theoretical operating regions on i_d-i_q plane of the selected motor. As can be seen, the i_{ch} value is located close to the current limit circle.

FIGURE 4.16: Theoretical i_d-i_q plane regions for the IPM drive motor of Tab 4.1.

The control algorithms have been implemented on an ARM architecture floating-point DSP STM32F407VET6, using LEM HC5F800-s as the current transducer, based on hall-effect principle. The run-time control data, such as set points and measured currents on the d-q axis, are logged by STM-Studio software. The active brake has been controlled by a speed loop control, while the motor under test has been controlled with a torque reference employing the proposed control loop and strategies. The IPM motor has a nominal continuous torque of 8.5N m @ 4500rpm. The lamination external diameter is equal to 120mm, while the stack length is equal to 120mm. The motor is cooled by natural convection and radiation air cooling frame with fins. The rotor position sensor is an absolute digital magnetic encoder.
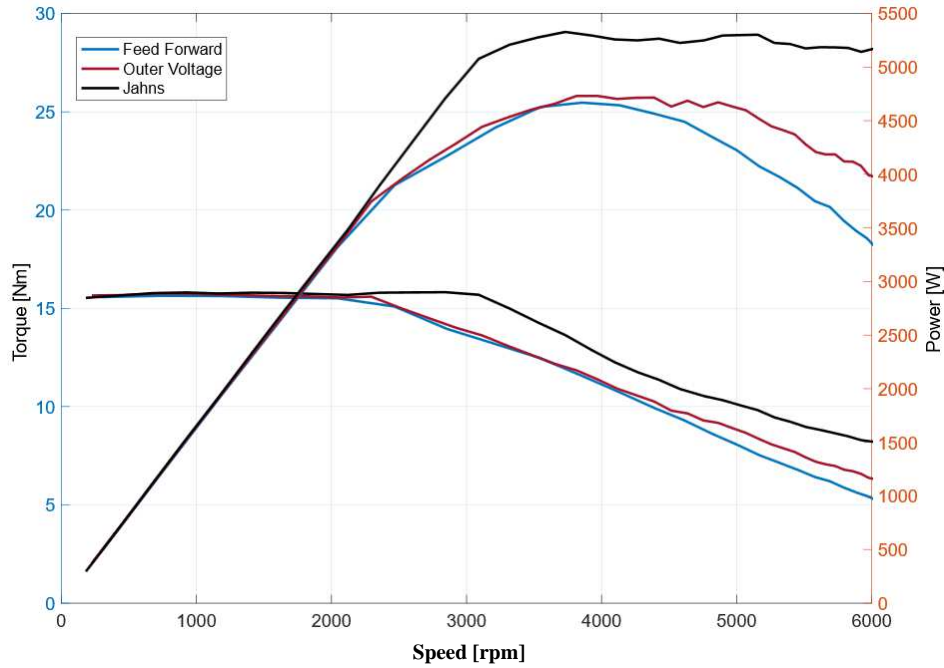
FIGURE 4.17: Results comparison between feed forward method and the improved proposed methods. Feed forward strategy (red solid line), improved outer voltage (light blue solid line) and improved Jahns method (black solid line).

Figure 4.17 show the result of the comparison between feed forward approach, optimized outer loop and optimized Jahns in terms of torque and power generation versus speed. It is clearly visible that Jahns outperforms both feed forward method and outer loop method.

4.6   Conclusion

In this chapter has been analysed different IPM motor control strategies for light traction pure electric vehicles. Two methods proposed in literature based on saturation of current regulators detection or on voltage saturation detection have been adopted. Their performance well exploits the potential of the IPM electrical machine in flux-weakening during acceleration, but since they rely on an integral action some issues could arise in deceleration depending on the integral dynamic as observed during experimental tests. According to this, to overcome this issue have been introduced two additional control strategies to optimize their performance during deceleration. The proposed control actions are "*id-safe*" and anti-windup approach. The "*id-safe*" is a feed forward value which corrects the i_d current command according to motor speed and bus voltage. The anti-windup avoids the deep saturation of d-q current PI regulators allowing to fully exploit the available bus voltage. The optimized methods have been validated by experimental tests with an IPM motor for a light electric vehicle. Both methods have improved the motor performance, during the transition from flux-weakening strategy to MTPA due to deceleration. The anti-windup must be applied with great care in case of the outer voltage control strategy.

Bibliography

[1]   A. Fratta, A. Vagati, and F. Villata. "Enhanced Internal Permanent-Magnet Machines Flux Weakening Control Strategies for Traction Applications". In: *ICEM International Conference on Electrical Machines*. Vol. 2. Aug. 1990, pp. 1059–1065. URL: http://hdl.handle.net/11583/1418830.

[2]   Dongyun Lu and N. C. Kar. "A review of flux-weakening control in permanent magnet synchronous machines". In: *2010 IEEE Vehicle Power and Propulsion Conference*. Sept. 2010, pp. 1–6. DOI: 10.1109/VPPC.2010.5728986.

[3]   S. Bolognani, S. Calligaro, R. Petrella, and F. Pogni. "Flux-weakening in IPM motor drives: Comparison of state-of-art algorithms and a novel proposal for controller design". In: *Proceedings of the 2011 14th European Conference on Power Electronics and Applications*. Aug. 2011, pp. 1–11.

[4]   T. M. Jahns. "Flux-Weakening Regime Operation of an Interior Permanent-Magnet Synchronous Motor Drive". In: *IEEE Transactions on Industry Applications* IA-23.4 (July 1987), pp. 681–689. ISSN: 1939-9367. DOI: 10.1109/TIA.1987.4504966.

[5]   N. Bianchi, S. Bolognani, and M. Zigliotto. "High-performance PM synchronous motor drive for an electrical scooter". In: *IEEE Transactions on Industry Applications* 37.5 (Sept. 2001), pp. 1348–1355. ISSN: 1939-9367. DOI: 10.1109/28.952510.

[6]   L. Sepulchre, M. Fadel, M. Pietrzak-David, and G. Porte. "MTPV Flux-Weakening Strategy for PMSM High Speed Drive". In: *IEEE Transactions on Industry Applications* 54.6 (Nov. 2018), pp. 6081–6089. ISSN: 1939-9367. DOI: 10.1109/TIA.2018.2856841.

[7]   R. Krishnan. "Control and operation of PM synchronous motor drives in the field-weakening region". In: *Proceedings of IECON '93 - 19th Annual Conference of IEEE Industrial Electronics*. Nov. 1993, 745–750 vol.2. DOI: 10.1109/IECON.1993.338988.

[8]   S. Morimoto, Y. Takeda, T. Hirasa, and K. Taniguchi. "Expansion of operating limits for permanent magnet motor by current vector control considering inverter capacity". In: *IEEE Transactions on Industry Applications* 26.5 (Sept. 1990), pp. 866–871. ISSN: 1939-9367. DOI: 10.1109/28.60058.

[9]   S. Morimoto, Y. Tong, Y. Takeda, and T. Hirasa. "Loss minimization control of permanent magnet synchronous motor drives". In: *IEEE Transactions on Industrial Electronics* 41.5 (Oct. 1994), pp. 511–517. ISSN: 1557-9948. DOI: 10.1109/41.315269.

[10]   Liu Qinghua. "Analysis, design and control of permanent magnet synchronous motors for wide-speed operation". PhD thesis. National University of Singapore, Sept. 2005. URL: https://scholarbank.nus.edu.sg/handle/10635/15011.

[11]   B. Stumberger, G. Stumberger, D. Dolinar, A. Hamler, and M. Trlep. "Evaluation of saturation and cross-magnetization effects in interior permanent-magnet synchronous motor". In: *IEEE Transactions on Industry Applications* 39.5 (Sept. 2003), pp. 1264–1271. ISSN: 1939-9367. DOI: 10.1109/TIA.2003.816538.

[12]   G. Pellegrino, E. Armando, and P. Guglielmi. "Direct-Flux Vector Control of IPM Motor Drives in the Maximum Torque Per Voltage Speed Range". In: *IEEE Transactions on Industrial Electronics* 59.10 (Oct. 2012), pp. 3780–3788. ISSN: 1557-9948. DOI: 10.1109/TIE.2011.2178212.

[13]   G. Pellegrino, E. Armando, and P. Guglielmi. "Direct Flux Field-Oriented Control of IPM Drives With Variable DC Link in the Field-Weakening Region". In: *IEEE Transactions on Industry Applications* 45.5 (Sept. 2009), pp. 1619–1627. ISSN: 1939-9367. DOI: 10.1109/TIA.2009.2027167.

[14]   A. Vagati, M. Pastorelli, and G. Franceschini. "High-performance control of synchronous reluctance motors". In: *IEEE Transactions on Industry Applications* 33.4 (July 1997), pp. 983–991. ISSN: 1939-9367. DOI: 10.1109/28.605740.

[15]   R. Fornari, G. Franceschini, D. David, A. Torreggiani, C. Bianchini, and M. Frigieri. "Enhanced Internal Permanent-Magnet Machines Flux Weakening Control Strategies for Traction Applications". In: *IECON 2019 - 45th Annual Conference of the IEEE Industrial Electronics Society*. Vol. 1. Oct. 2019, pp. 2682–2687. DOI: 10.1109/IECON.2019.8926936.

Conclusions and assessment of the results

This thesis work has dealt with soft-switching DC-DC converters for HEVs or Full EVs, highlighting the characteristics required for such kind of applications. The design was focused on efficiency, power density and wide voltage/power range capability. Two different typologies have been designed and experimental validated. The LLC converter was proposed as power stage of a unidirectional battery charger. The DAB was proposed as a battery charger suitable for V2G capability or as a bidirectional converter of a PV plant where the vehicle's battery is used as storage mean. In power train application flux-weakening control strategy is a critical point because the electrical motor operates in a wide speed range above the constant torque region. An enhanced flux-weakening control strategy for a high speed IPM has been proposed to overcome the fast torque transition issues.

The design of the 2kW LLC prototype was characterized by resonant tank parameters sized for wide output voltage range capability. The power transformer was made with a planar core and the construction characteristics were illustrated in details. The benefits, drawbacks and critical aspects related to the advanced PWM adopted at light load condition were investigated through simulation models and experimental tests. An innovative *Adaptive PWM* control, based on Quasi-Resonant control, was proposed to overcome the hard-switching losses on the first commutation of the high side MOSFET during PWM operation. The benefits resulting from this control technique on the switching losses were analysed for different device part numbers. Exploiting the free oscillation, the soft-switching conditions for the high side MOSFET are identified by the Free Oscillator Peak Detector Circuit. By means of the Peak Detector, the valley of the midpoint voltage is identified and the PWM signals are re-enabled from the masking state. A Duty Cycle Corrector circuit properly compensates the duty cycle of the low side MOSFET to prevent the saturation of the transformer. The laboratory prototype was used to identify the losses distribution and demonstrated the benefits introduced by SiC devices adoption. The experimental results have validated the design of the converter and the efficiency curves were obtained.

The 3, 2kW DAB converter has been prototyped. Rather than traditional Phase-Shift, two advanced Trapezoidal and Triangular modulation techniques known in literature were implemented. The series inductance value was properly chosen for the *wide voltage/power capability* at both DC-link sides. With the solutions adopted by the design of this proposed work, the soft-switching operations were extended to the overall operating range of the converter and the wide range capabilities were reached by means of a *single-stage* architecture. In particular, the computations of the dwell times performed by the control logic were made in *feed forward* and an additional block was inserted to compensate the inaccurate knowledge of all DAB

parameters. This work has investigated for both modulation schemes the semiconductor power losses and hard-switching commutations. Comparison based on thermal/power losses simulation model was carried out, disclosing that different criteria can be adopted to choose the devices according to the predominant modulation sequence. Transistors with low conduction losses are more suitable for Triangular modulation, while transistors with optimized dynamic characteristics are preferable in Trapezoidal case. The experimentals show the feasibility of the design, validating the overall control strategy, wide voltage range capability and hard-switching commutations. High power conversion efficiency was obtained even adopting standard low-cost power semiconductor devices.

The last chapter of this thesis has focused on an *enhanced flux-weakening* IPM motor control strategy. Two methods proposed in literature based on the detection of the saturation of current regulators or of the voltage have been adopted and investigated via experimental tests. Their performance well exploits the potential of the IPM electrical machine in flux-weakening during acceleration, but since they rely on an integral action some issues could arise. Depending on the integral dynamic of the control loops the braking phase may result uncontrolled. Due to this, the vehicle behaviour could be heavily affected by the braking torque generated by the motor. Especially for motorcycles also a short time braking torque could cause driver injuries. To overcome this issue two new additional control strategies have been introduced in this work. The strategies are based on *id-safe* and *anti-windup* approach to optimize their performance during deceleration. The *id-safe* is a *feed forward* value which corrects the i_d current command according to motor speed and bus voltage. The *anti-windup* avoids the deep saturation of d-q current PI regulators allowing to fully exploit the available bus voltage. Experimental tests have shown that both methods have improved the motor performance, during the transition from flux-weakening strategy to MTPA due to deceleration.

Appendix A

Fundamentals of electromagnetism

A.1 Introduction to Maxwell's equations

Maxwell's equations describe the electromagnetic phenomenons [1], [2]. Maxwell was able to look at the magnetic field and electric field, current and charges to explain mathematically how they work and interact with each other. Furthermore, he was able to find a mathematical way of showing what was the speed of light. Maxwell's equations are a set of mathematical equations representing electric and magnetic field. By these equations is possible to study how one field affects the other. Moreover how the fields are affected by charges and currents, and how currents affect the fields.
The electric and the magnetic fields interact in his way:

- Charges create electric field: a presence of a charge generates an electric field. So any atom due to the electrons and protons has an electric field around it.

- Vibrating charges (accelerating and decelerating charges) create electromagnetic waves.

- Moving charges create a magnetic field: only if there are moving charges, there is a magnetic field.

- Magnetic field cause forces on charges moving perpendicular to the field: a charge inside a magnetic field does not experience any force until the charge starts to move (or a relative movement with respect the magnetic field).

- Electric field causes force on moving or still charges: the movement depends on the direction of the electric field and the polarity of the charge.

The statements listed before are summarized by the four Maxwell's equations. These four equations describe the electric field, the magnetic field and how they interact with each other.

A.1.1 Gauss's law for the electric field

$$\Phi_E = \oint \vec{E} \cdot d\vec{A} = \frac{Q}{\varepsilon_0} \tag{A.1}$$

Fig. A.1 shows a positive charge Q rounded by a generic surface. The infinitesimal vectorial area element $d\vec{A}$ is equal to the product between the infinitesimal segment dx and dy, times the unit vector $d\vec{n}$ perpendicular to the area (eq. A.2).

$$d\vec{A} = dA \cdot \vec{n} = dx \cdot dy \cdot \vec{n} \tag{A.2}$$

The eq. A.1 can be rewritten in this way:

$$\Phi_E = \oint \vec{E} \cdot dx \cdot dy \cdot \vec{n} = \oint E \cdot dx \cdot dy \cdot \cos\theta \tag{A.3}$$

The idea of Gauss was to choose a spherical surface of radius R (Gaussian surface - Fig. A.2) such that the electric field is always perpendicular ($cos(\theta) = 1$). In such way the eq. A.3 begins:

$$\Phi_E = \oint E \cdot dx \cdot dy = \oint E \cdot dA = \frac{Q}{\varepsilon_0} \tag{A.4}$$

Considering the spherical surface, the value of the electric field is expressed as follows:

$$E = \frac{Q}{4\pi R^2 \varepsilon_0} = \frac{kQ}{R^2} \tag{A.5}$$

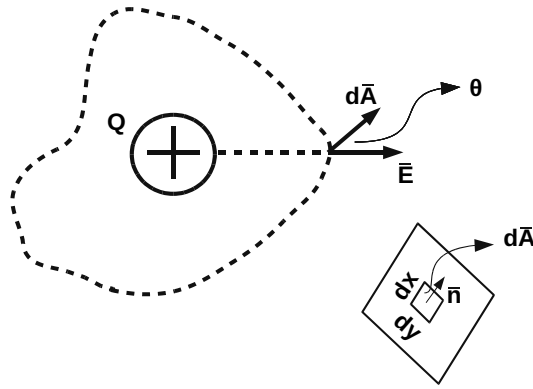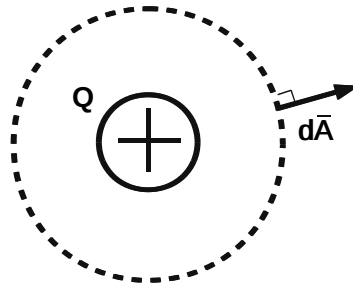FIGURE A.1: Generic surface containing the charge Q and infinitesimal area $d\vec{A}$.

FIGURE A.2: Charge Q inside a Gaussian surface.

The Gauss's law for the electric field says that for a given charge, rounded by a Gaussian surface, the electric field emanating from that is equal to the charge inside over the permittivity of the free space ϵ_0. It's obtained considering that any infinitesimal element of the Gaussian surface is perpendicular to the field because it's a spherical surface. This equation correlates the strength of the electric field based upon the distance away from the charge, defined by the radius of the sphere.

A.1.2 Gauss's law for magnetism

$$\Phi_B = \oint \vec{B} \cdot d\vec{A} = 0 \tag{A.6}$$

Equation A.6 states that the magnetic field generated by the presence of a magnet and the total amount of flux entering into the surface is equal to the total amount leaving the surface. As result for a given Gaussian surface, the net flux [1] is always equal to zero, no matter where the surface is defined. This is different for an electric field when the net electric flux is zero for a surface enclosing no charge.

The Gauss's law for the magnetism tells us that the integral over all surface of the strength of the magnetic field is always zero, wherever the surface is placed with respect to the magnet that causes the field. As it can be seen from Fig. A.3 illustrating the two cases.

$$\oint \vec{B} \cdot d\vec{A} = 0$$

$$\oint \vec{B} \cdot d\vec{A} = 0$$

(a) Gaussian surface over a magnetic field lines.

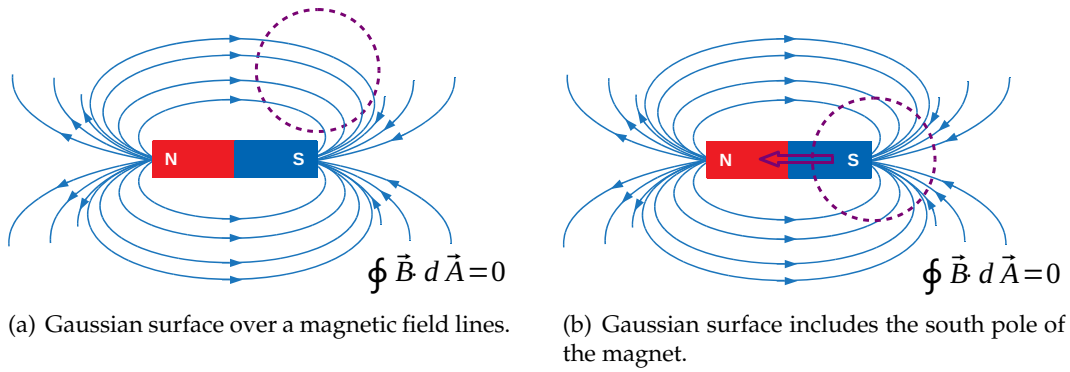(b) Gaussian surface includes the south pole of the magnet.

FIGURE A.3: Examples of Gauss's law for the magnetic field.

In the case a) the Gaussian surface is placed outside from the magnet. Because the lines of the magnetic field always loop backs the result of the integral is zero. The same thing happens for the case b), where the Gaussian surface is placed over the south pole of the magnet. Because the property of the magnetism is not possible to enclose only the south or the north pole. If a magnet is broken in two parts, the new parts have always a north and a south pole. Is not possible to identify a "magnetic charge" as the case of the electric charge. The magnetic charge does not exist. As a consequence, for any closed surface, the number of the magnetic entering lines is equal to those that leave the surface. So for the case b) the field that enters into the surface loops back through the magnet to the north pole. The integral of $\vec{B}$ all over the surface is still zero.

Making similar consideration for the electric field, where is possible to identify a charge, is possible to understand the case of Fig. A.4(a) and of Fig. A.4(b) right away. In the former, the integral is not zero because the surface encloses the charge. In the latter is zero because the charge is outside from the surface.

---

[1] Flux is a measure of how much of the field passes through a given surface.

(a) Gaussian surface includes the charge Q.

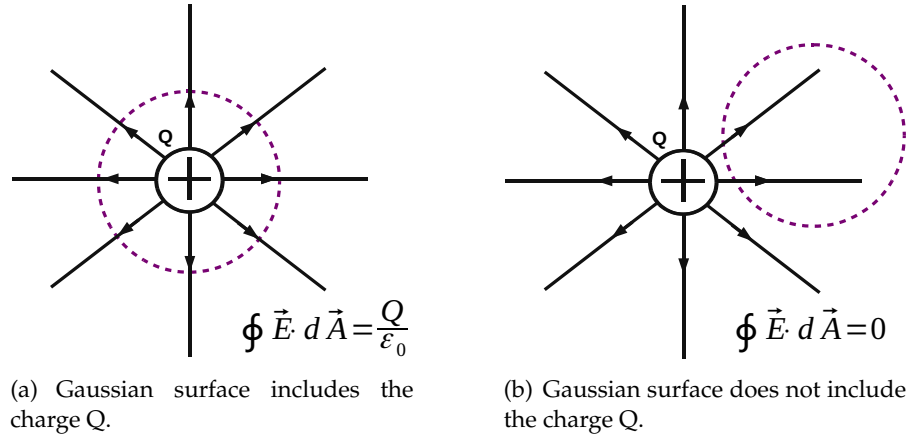(b) Gaussian surface does not include the charge Q.

FIGURE A.4: Examples of Gauss'law for the electric field.

A.1.3 Faraday's law of induction

$$V_{EMF} = \oint \vec{E} \cdot d\vec{s} = - \frac{d\phi_B}{dt} \tag{A.7}$$

Figure A.5 illustrates a conductor loop (a conductor that allows the current flow) that has free charges and a magnetic field going to through the loop.
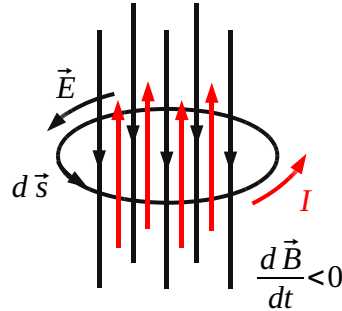

FIGURE A.5: Faraday law loop.

If the magnetic field is stationary, nothing happens. The magnetic flux is defined as:

$$\Phi_B = \vec{B} \cdot \vec{A}$$

where B is the density of the magnetic flux and A is the area of the loop. When Φ_B changes with respect the time (either increasing or decreasing), it will cause an electric field to exist inside the conductor. The integral of the electric field $\vec{E}$ inside the conductor times the infinitesimal line segment $d\vec{s}$ through the all length of the conductor is equal to the voltage named *Electromotive Force* V_{EMF}, equal to the change of the magnetic flux Φ_B with respect the time.

In Fig. A.6 are shown the plates of a capacitor. A positive test charge q is at the negative plate. To move the test charge from the negative plate to the positive plate a certain amount of work W is needed. The work is given by the product between the force and the distance:

$$W = \vec{F} \cdot \vec{d}$$

The force experienced by the test charge is equal to:
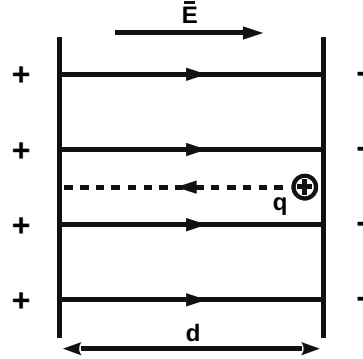
$$\vec{F} = \vec{E} \cdot q$$

FIGURE A.6: Capacitor plates at distance d, with test charge Q.

The amount of work needed can be rewritten in this way:

$$W = \vec{E} \cdot q \cdot \vec{d} \tag{A.8}$$

Dividing both sides by the test charge q:

$$\frac{W}{q} = \frac{\vec{E} \cdot q \cdot \vec{d}}{q} \tag{A.9}$$

is obtained this expression:

$$V_{EMF} = \vec{E} \cdot \vec{d} \tag{A.10}$$

where V_{EMF} is the electromotive force, i.e. the potential difference between the two plates. The name *potential difference* explains that a charge is pushed to a different value of potential: a positive charge is pushed to the lower value of the potential, while a negative one is pushed to the higher value. The potential difference is strictly related to the work done over the charge. In the example of the capacitor plates, the potential difference at the plates is defined as the work to take a charge across the plates, divided by the size of the charge.

The Faraday's law tells us that a change over the time of the magnetic flux Φ_B will cause an electric field $\vec{E}$ into the loop. This means that the change in magnetic flux in the loop causes a voltage to exist around the loop and vice versa. The electric field will cause charges to move, so current to exist in the loop. So this equation explains that is possible to set up a current I by changing the $\vec{B}$ field trough the loop.

The minus sign, known as *Lenz's law*, means the voltage tends to be opposite to the variation of magnetic field has caused it: the current I generates a $\vec{B}$ field in order to oppose the change, and so the direction of the induced field is opposite to the variation of the original one (compare the red and black lines of the Fig. A.5). In summary, Faraday's law says:

- The changing of the magnetic field $\vec{B}$ inside the current loop sets up an electric field $\vec{E}$ along the current loop.

- The electric field $\vec{E}$ induces an electromotive force V_{EMF} that causes a current I into the loop.

- The current I sets a magnetic field in order to oppose the change of the original magnetic field B.

- The changing of the magnetic field acts literally as a *Elecromotive force* on the charges.

A.1.4 Ampere's law

$$\oint \vec{B} \cdot d\vec{s} = \mu_0 I + \mu_0 \varepsilon_0 \frac{d}{dt} \Phi_E \tag{A.11}$$

Given wire carrying a current (Fig. A.7), there will be a magnetic field around. The integral of the magnetic field $\vec{B}$ along the all length of a circular region rounding the wire, whose $d\vec{s}$ is a small segment, will be equal to current enclosed in the region times the vacuum permeability μ_0.
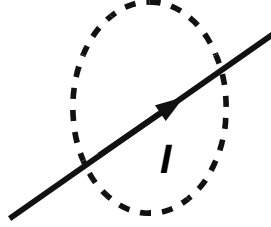

FIGURE A.7: Current through a wire inside a circular region.

It means that whenever is a current always there is a magnetic field and vice versa and the strength of the magnetic field is proportional to the current. According to Ampere's law A.7, the second term on the right side of the equation states that a change of the strength of the electric flux also causes a magnetic field. The second term is a current, as well. As explained in the following it's commonly named *displacement current*. So the magnetic field is created by currents and by the change of the electric field.

Figure A.8 depicts the first term of the Ampere's law equation. Considering that the magnetic field $\vec{B}$ is always in the same direction of the small segment $d\vec{s}$ of the loop, the term

$$\vec{B} \cdot d\vec{s} = B \cdot ds \cdot cos(\theta)$$

can be rewritten in this way, considering that the angle θ is equal to zero over all the wire loop. By these considerations the first term of the equation is equal to:

$$\oint \vec{B} \cdot d\vec{s} = \oint B \cdot ds = B \cdot 2\pi R = \mu_0 I \tag{A.12}$$

Rearranging the terms of the eq. A.12 is obtained:

$$B = \frac{\mu_0 I}{2\pi R} \tag{A.13}$$

The eq: A.13 indicates the strength of the magnetic field $\vec{B}$ in the space, for the wire run by the current I at the distance R.
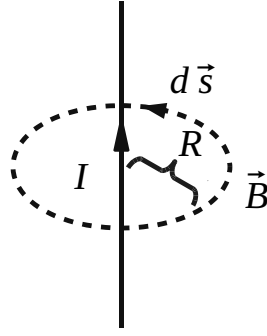
FIGURE A.8: First term of the Ampere's law.

As mentioned before, the second term of the Ampere's law gives a second condition by the magnetic is generated: the change of the electric flux Φ_E with respect the time. If the electric field changes it causes the magnetic field to exist. Figure A.9 gives an example of the electric flux between two plates of a capacitor. The magenta dotted line is an imaginary line completely encompassing the magnetic field between the plates. Through the area A, defined by the line, there is the electric flux, given by:

$$\Phi_E = E \cdot A$$

Changing the potential difference between the places changes the electric field. The change of the electric field causes the magnetic flux to exist as the same a current is going away from one plate to the other one. This displacement current I_{DISP} is an imaginary current that does not exist, but produces the same effect as shown in Fig. A.8 for the first term of the Ampere's law. Ampere realizes that changing the electric flux acts just like there is a current going from one plate to the other.
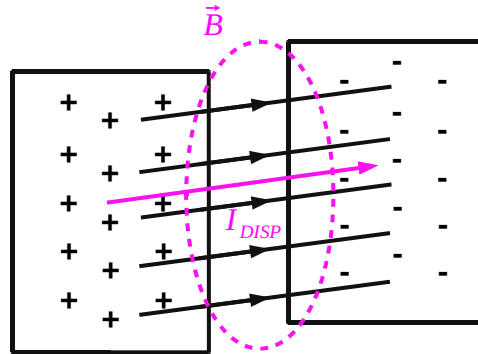

FIGURE A.9: Example of second term of the Ampere's law between two capacitor plates.

In summary, Ampere's law says that:

- There is a magnetic field around a current loop.

- There is a magnetic field around a region where an electric field is changing.

The speed of light

As shown in Fig. A.10, the strength of the electric field $\vec{E}$ due to the presence of the charge Q at the distance R is given by the equation A.14. The term ϵ_0 represent the vacuum permittivity, of value given by the eq. A.15.
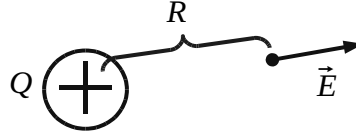
FIGURE A.10: The strength of the electric field $\vec{E}$ for a given positive
charge Q at R distance.

$$E = \frac{Q}{4\pi\varepsilon_0 R^2} \tag{A.14}$$

$$\varepsilon_0 = 8.85 \times 10^{-12}\frac{C^2}{Nm^2} \tag{A.15}$$

As shown in Fig. A.11 the strength of the magnetic field $\vec{B}$ generated by the
current I run a wire, at distance R is given by the eq. A.14, where μ_0 is the vacuum
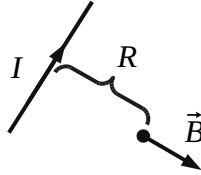permeability, of value given by the eq. A.16.

FIGURE A.11: The strength of the magnetic field B for a wire run a
current I at R distance

$$\mu_0 = 4\pi \times 10^{-7}\frac{Wb}{Am} \tag{A.16}$$

$$B = \frac{\mu_0 I}{2\pi R^2} \tag{A.17}$$

The variables ϵ_0 and μ_0 are the property of the free space and determines how
fast the magnetic field and electric field can interact with each other and with the
charges and currents. Those variables determine how an electromagnetic wave can
move in the free space. The speed of the light c is determined by these two constant,
in the form of the eq. A.18.

$$c = \frac{1}{\sqrt{\mu_0\varepsilon_0}} = \frac{1}{\sqrt{\left(4\pi \times 10^{-7}\right)\left(8,85 \times 10^{-12}\right)}} = 2,998 \times 10^8 \frac{m}{s} \tag{A.18}$$

A.2 Fundamental form of Maxwell's equations

By the definition the electric and magnetic permeability of a generic material is given by:

$$\varepsilon = \varepsilon_0 \left(1 + \chi_e\right) \varepsilon_0 \cdot \varepsilon_r$$

$$\mu = \mu_0 \left(1 + \chi_m\right) = \mu_0 \cdot \mu_r \tag{A.19}$$

where χ_e and χ_m are the electric and magnetic susceptibilities of a given material, respectively. The terms ε_r and μ_r correspond to the relative permittivity and relative permeability. Actually, by the electric and magnetic permeability of a material is possible to describe how the material interacts with the electric or magnetic field. In this way is possible to have the relation between the *displacement field* $\vec{D}$ with respect the electric field $\vec{E}$ and the "magnetic induction" $\vec{B}$ with respect the magnetic field $\vec{H}$:

$$\vec{D} = \varepsilon \vec{E}$$

$$\vec{B} = \mu \vec{H} \tag{A.20}$$

Due to this meaning, the eq. A.20 are named *constitutive relations* in the electromagnetism. By the displacements we know "how many" the charges inside the material tend to be moved by the electric field and by the induction how much magnetic flux it catches.

The Ohm's law describes the effects of the electric field $\vec{E}$ on the current density $\vec{J}$. The conductivity σ gives this relation that can be considered as the third constitutive material equation:

$$\vec{J} = \sigma \vec{E} \tag{A.21}$$

Considering that the electric and magnetic permeabilities are constant, Maxwell's equations can be rewritten as shown by the Tab. A.1.

	Standard form	with constitutive relations
Gauss's law for $\vec{E}$	$\nabla \cdot \vec{E} = \frac{\rho}{\varepsilon_0}$	$\nabla \cdot \vec{D} = \rho$
Gauss's law for $\vec{B}$	$\nabla \cdot \vec{B} = 0$	$\nabla \cdot \vec{H} = 0$
Ampere's law	$\nabla \times \vec{B} = \mu_0 \vec{J} + \mu_0 \varepsilon_0 \frac{\partial \vec{E}}{\partial t}$	$\nabla \cdot \vec{H} = \vec{J} + \frac{\partial \vec{D}}{\partial t}$
Faraday's law	$\nabla \times \vec{E} = -\frac{\partial \vec{B}}{\partial t}$	

TABLE A.1: Maxwell's equation in differential and integral form.

A.3 Magnetomotive force and Hopkinson's law

In the chapter A.1 it has been seen that an electromotive force V_{EMF} is experienced by a charge placed in an electric field. This force causes a current flow of the charges through the conductor. Similarly, it happens in the presence of a magnetic field for a hypothetical "magnetic charge" that experienced the magnetic flux ϕ_B. Does not exist any kind of current of magnetic charge, but this analogy makes easy the relationship between the Ohm's law and the Ohms's law for the magnetic circuit, also known as "Hopkinson's law".

The Ohm's law states that the relationship between the electromotive force and current I flowing through the conductor is proportional to the resistance R:

$$V_{EMF} = R \cdot I$$

The Hopkinson's law is of the same form, where $\mathcal{F}$ is the Magnetomotive Force (MMF), and $\mathcal{R}$ is the reluctance.:

$$\mathcal{F} = \phi_B \cdot \mathcal{R} \tag{A.22}$$

Comparing it to the Ohm's law, $\mathcal{F}$ makes the role of Electromotive force V_{EMF}, ϕ_B of the current I and $\mathcal{R}$ of the resistance R. The MMF can be obtained from the Ampere's law (rearranging the eq. A.11 with eq. A.20):

$$\mathcal{F} = \oint \vec{H} \cdot d\vec{l} = \oint \frac{\vec{B}}{\mu} \cdot d\vec{l} = \oint \frac{\phi_B}{\mu A} \cdot d\vec{l} = \phi_B \mathcal{R} = NI \tag{A.23}$$

where the reluctance has been expressed as:

$$\mathcal{R} = \frac{l}{\mu A} \tag{A.24}$$

The term l is the length, A is the cross sectional area and μ is the permeability of the material given by the eq. A.19. Similarly to the expression of the electric resistance:

$$R = \rho \frac{l}{A}$$

the inverse of the permeability makes the role of the resistivity ρ.

By these considerations the Hopkinson's law can be rewritten as the relation between the ampere-turn and the linkage flux:

$$\phi_B \cdot \mathcal{R} = N \cdot I \tag{A.25}$$

This makes clear why the unit measure of the MMF is the ampere-turn (At). The eq. A.25 is useful to analyse a magnetic circuit. As in the electric domain the current flows through the least resistance path, the same happens in a magnetic circuit. The Gauss's law for the magnetism tells us that the magnetic flux always follows a closed loop. The path of the loop depends on the reluctance: where is lower reluctance there is a higher concentration of the magnetic flux. The term ϕ_B has to be intended as the flux running through every loop of the N windings.

Another expression of the Hopkinson's law can be obtained. Both terms of the eq. A.25 can be multiplied by N:

$$N\phi_B \cdot \mathcal{R} = N^2 \cdot I \tag{A.26}$$

Now, by the definition of *inductance*:

$$L = \frac{N^2}{\mathcal{R}} \tag{A.27}$$

the Hopkinson's law can be rewritten in this way:

$$N\phi_B = LI \tag{A.28}$$

Bibliography

[1] Albert Shadowitz. *The Electromagnetic Field*. 1st ed. Dover Publications, Apr. 2012. ISBN: 0486132013.

[2] Corrado Mencuccini and Vittorio Silvestrini. *Fisica Elettromagnetismo e ottica*. 1st ed. Casa editrice Ambrosiana, Jan. 2017. ISBN: 880818661X.